

Searching for late-time interaction between Type Ia supernovae and distant circumstellar material using the Zwicky Transient Facility

A dissertation submitted to the University of Dublin
for the degree of Doctor of Philosophy

Jacco H. Terwel

School of Physics, Trinity College Dublin

Supervisor:

Prof. Kate Maguire

Co-Supervisor:

Dr.

September 2024



Trinity College Dublin

Coláiste na Tríonóide, Baile Átha Cliath

The University of Dublin

Declaration

I agree to deposit this thesis in the University's open access institutional repository or allow the Library to do so on my behalf, subject to Irish Copyright Legislation and Trinity College Library conditions of use and acknowledgement.

I consent to the examiner retaining a copy of the thesis beyond the examining period, should they so wish (EU GDPR May 2018).

Name: Jacco H. Terwel

Signature: **Date:** 01/09/2024

Summary

... abstract ...

... *dedication* ...

Acknowledgements

... acknowledgements ...

List of Publications

Publications

1. ... publications ...

Contents

List of Publications	vi
List of Figures	ix
List of Tables	xiii
1 Introduction	1
1.1 The final stages of stars	1
1.2 Type Ia SNe	1
2 Observing in the optical regime	3
2.1 Types of observations	3
2.1.1 Photometry	4
2.1.2 Spectroscopy	4
2.2 Telescopes	6
2.2.1 Zwicky Transient Facility	6
2.2.2 Nordic Optical Telescope	8
2.2.3 Gran Telescopio CANARIAS	8
2.2.4 Other observations	9
2.3 Calibration images	10
2.3.1 Bias	10
2.3.2 Dark	10
2.3.3 Flatfield	11
2.3.4 Arc	11
2.4 Reduction	12
2.4.1 Bias, dark, and flat corrections	13
2.4.2 Cosmic-ray removal and image stacking	13
2.4.3 Standard star calibration	13
2.4.4 Forced photometry	14
2.5 General considerations for observing	15
2.5.1 Location	15
2.5.2 Telescope, instrument, observation type, and setup	17
2.5.3 Night plan	17
3 ZTF SN Ia DR2: Searching for late-time interaction signatures in Type Ia supernovae from the Zwicky Transient Facility	20
3.1 Data	20
3.1.1 ZTF light curve data	21
3.1.2 Baseline correction	22
3.2 Analysis	23

3.2.1	Binning & filtering programme	23
3.2.2	Removal of SN Ia radioactive tail detections	25
3.2.3	SuperNova Animation Programme (SNAP)	27
3.2.4	Simulated interaction recovery fractions	28
3.2.4.1	The interacting SN model	28
3.2.4.2	Simulating the observing campaign	30
3.2.4.3	Simulated interaction recovery	32
3.2.4.4	Impact of reference image depth	35
3.3	Results	35
3.3.1	Initial summary of detected events	36
3.3.1.1	Known Ia-CSM	36
3.3.1.2	Siblings	42
3.3.1.3	Kinked tails	43
3.3.2	Additional tests of promising events	44
3.3.2.1	Scene modelling photometry	45
3.3.2.2	AGN contamination	47
3.3.2.3	Presence of a sibling close to the SN location	47
3.3.2.4	Late-time interaction candidates	53
3.3.3	Late-time CSM interaction rates based on our candidate objects	60
3.4	Discussion	64
3.4.1	Late-time interaction is rare in SNe Ia	64
3.4.2	Properties of SNe Ia with late-time interaction	66
3.4.3	Limitations of the analysis	67
3.4.4	By-product pipeline detections	69
3.5	Conclusions	69
3.6	Tables	71
3.7	Inputs to SIMSURVEY simulations	74
3.8	Late-time spectrum of SN 2020alm	74
3.9	Binned SMP light curves of the final candidates	76
	References	79

List of Figures

1.1	<i>gri</i> composite image of NGC4216 using observations taken by the Zwicky Transient Facility. Left: composite image of observations taken before 1 January 2024. Right: composite image of observations taken between 5 and 19 January 2024, the first two weeks after the first detection of the Type Ia SN 2024gy. (Credit: Benjamin Nobre Hauptmann) Use this as an example when introducing transients	2
2.1	Image and partial spectrum of SN 2024nqr (left) and SN 2024pgd (right), two SNe Ia active simultaneously in the same galaxy. The image was taken without a filter and used to align the 1.0'' slit (horizontal dashed lines) over both SNe. The resulting spectrum, taken with grism #4, shows three traces as white vertical stripes. The outer two line up with the two SNe, while the middle trace is from the host galaxy edge in the slit (vertical dotted lines for guidance). The horizontal lines in the spectrum are sky lines coming from atmospheric emission, and the white spots in the spectrum are due to cosmic rays. This data was taken with NOT/ALFOSC on the night of 28 July 2024 while testing an experimental rapid response mode (RRM, credit: Samuel Grund Sørensen). check AT/SN status weirdness	5
2.2	Throughput as a function of wavelength of the different filters used to gather the bulk of the data in this thesis <i>g</i> filters are shown in green, <i>r</i> in orange, <i>i</i> in red, and the different telescopes are shown with different line styles (Continuous for ZTF, dashed for NOT, dot-dashed for GTC). The SDSS filters (dotted lines) are shown for comparison. For the grisms the wavelength ranges are shown as only, not their efficiency at each wavelength.	7
2.3	Night plan for the NOT on the night of 10 August 2024. Targets are plotted with their altitude as a function of universal standard time. Local stellar time is shown on top. The target priority has been colour coded, with the coloured bars showing the amount of time each observation is expected to take. Green targets have already been completed, and the red vertical line shows the current time. Several unscheduled backup targets are shown in case the plan has to be updated during the night.	19

- 3.1 First 250 days of the *gri*-band light curves of SN 2019hbb in flux scaled to the peak flux (top panel) and magnitude (bottom panel) space. Binning starts 100 days after the estimated peak date (vertical black dashed and solid lines), using 25 d bins. The *g*-, *r*-, and *i*-bands are shown green, orange, and red, respectively. Before 100 days, we show the unbinned detections with their uncertainties (coloured circles) and non-detections (inverted triangles). After 100 days we show the bins as horizontal lines to show their size, a circle to show their mean value, and the shaded region showing the 1σ uncertainty (dashed regions are non-detections). A bin is deemed a non-detection if the flux $f < 5\sigma_f$. The 5σ magnitude limit is calculated and shown as a downward arrow. In both the *g*- and *r*-bands, the first bin is a detection and there are multiple adjacent bins with detections, triggering the tail-fitting procedure (see Section 3.2.2). The resulting tail fits are shown in the green and red lines, respectively, with their 1σ uncertainties as hashed regions. The half-life times are $t_{1/2,g} = 70 \pm 6$ d ($\chi^2_{\text{red}} = 0.6$) and $t_{1/2,r} = 27 \pm 4$ d ($\chi^2_{\text{red}} = 1.4$). This tail is therefore deemed to be a normal SN Ia tail. 26
- 3.2 Model spectrum at 300 days (SN 2011fe with the added H α line) is shown in magenta overlaid on a rest-frame spectrum of SN 2015cp at 694 days in grey. The model flux has been scaled to the distance of SN 2015cp for comparison. The green, orange, and red shaded regions are the bandwidths of the *g*-, *r*-, and *i*-bands, respectively. The transmission profiles are plotted in the same colours for each band. The model is also shown shifted to $z = 0.07$ (and offset up in flux), where the H α line has just started to be in the *i*-band. 30
- 3.3 *r*(orange) and *i*(red) absolute magnitude light curves of the SN 2011fe model used in the simulations in the ZTF bands as a function of phase from rest-frame *B*-band peak (Mazzali et al., 2014). The bumpiness in the models is because the underlying SNCOSMO model class interpolates in flux space but fails to find an exponential decay. The added rest-frame CSM interaction model based on H α emission (starting at a phase of 100 d) is shown with dotted lines for the *r*-band. Once the interaction becomes the dominant source, it smooths out the bumps from the underlying tail. The black line shows a radioactive decay with $t_{1/2} = 50$ d, typical of a declining normal SN Ia tail. 31
- 3.4 Fraction of SNe Ia for one of our simulations (interaction occurring between 500 – 1000 d after the peak) where the CSM interaction was recovered per redshift bin of size 0.002. The simulations are shown for interaction strengths of zero (grey), similar to SN 2015cp (red), and 10 times stronger than SN 2015cp (blue). In the simulation without CSM interaction, the recovery fraction should be interpreted as the fraction of false positives. The simulations with normal ZTF quality reference images are shown with dots and fitted sigmoid functions with solid lines. Simulations where one magnitude deeper reference images were assumed are shown in triangles, with their fitted sigmoid functions in dashed lines. 34

3.5	Binned late-time observations of the recovered known SNe Ia-CSM. All objects are shown in absolute magnitude and over the same time range for easy comparison. All objects are detected beyond 100 days after the peak without using the binning technique. We do not show these individual data points to increase readability. The tail fits are shown as solid lines with the hashed region denoting their 1σ uncertainties. For comparison, SN 2020ssf (ZTF20abytpc) in the top left corner is a normal SN Ia with a normally declining tail with $t_{1/2,g} = 53 \pm 1$ days and $t_{1/2,r} = 26 \pm 1$ days. The fitted tails for the SNe Ia-CSM are significantly shallower.	38
3.6	Binned late-time observations in flux space of the five events with a detected sibling, with the flux normalised to the found peak flux. All objects are plotted on the same flux scale for easy comparison except for SN 2018big, as its late-time detections are much weaker compared to the original SN peak magnitude due to the larger distance offset between the siblings.	40
3.7	Light curves of SN 2018big and its sibling SN 2019nvm in magnitude space using bins of 25 d. The g (green) and r (orange) bins follow the tail of SN 2018big until it disappears in the noise. About 450 d after the peak of SN 2018big, new detections are identified in the binned photometry. The individual observations remain upper limits, although their shape hint to the true nature of these late-time detections.	41
3.8	Five objects with kinks in their tails that start to deviate from the assumed decline rate at $\sim 200 - 250$ d post peak are shown in magnitude space as a function of days since peak. As most of these objects have their peak magnitude blinded, no scaling is shown. A normal radioactive decay model was fitted to these tails, shown as solid straight lines with their 1σ uncertainty as dashed regions. But as the ejecta opacity changes over time so does the half-life time of the tail, causing a kink seen in the bins which is not reproduced by the model. The arbitrarily normalised R -band light curve of SN 2011fe (known not to have CSM interaction from detailed spectral studies) (Zhang et al., 2016) is shown in blue, showing the same shift in decline slope at a similar phase.	43
3.9	Two objects whose late-time detections were revealed to be caused by the photometry extraction. The colours are as in Fig. 3.8. The left side shows the binned forced photometry light curve, and the right side shows the binned SMP light curve. Bins with 5σ detections are shaded solid, while the non-detections are hashed.	46
3.10	Objects whose late-time detections are explained in the additional tests. The top four rows show the light curves of the objects where a previously undetected sibling transient as an explanation for the late-time observations could not be ruled out, with forced photometry light curves in the left-hand panels and the scene modelling photometry light curves in the right-hand panels. The 5σ detections are shown as bins with solid uncertainty regions and bins with hashed uncertainty regions are non-detections. The object whose late-time detections are caused by the host galaxy AGN, SN 2019vzf, is shown in the bottom row. The colours are as in Fig. 3.8 with g band in green, r band in orange, and i band in red. .	49

3.11	Three candidate objects, shown in magnitude and flux space. All three have significant detections ($\geq 5\sigma$) after a period of observations consistent with zero flux. From the alternative explanations the best fitting alternate transients are shown in dotted lines. For SN 2018grt this is the Type IIP SN 2017gmr, for SN 2019ldf and SN 2020tfc this is the TDE AT 2018hco.	55
3.12	Colour curves of the three candidate objects, together with the colours of the best fitting alternate transients. The top and bottom panels show $g-r$ and $r-i$, respectively. The first bin for each object starts at zero days, but the bins can be shifted horizontally in an attempt to better fit the colour curve of the transient compared against (given that this is allowed by the rest of the light curve). Bins whose mean observation dates are closest to each other are used to calculate the colour, provided that these bins overlap in time. If there is a detection in only one band used to calculate the colour while the other is a non-detection, the result is a lower or upper limit.	56
3.13	Fraction of MCMC realisations per bin that resulted in one object being recovered in a sample with the same size as the effective DR2 sample size as a function of the late-time CSM interaction fraction. The best and worst case scenario for each object is shown in blue and red, respectively. A skewed normal distribution fit with a 1σ uncertainty band is shown for each scenario, and the dashed and dotted lines give maximum and 68 per cent confidence interval of these distributions, respectively. The distributions continue on the right side of each plot.	62
3.14	Spectrum of the late-time signal in SN 2020alm in its rest frame. The top panel shows the late-time spectrum obtained on 26 July 2023 using OSIRIS on the GTC, and the SDSS spectrum obtained in 2003. The bottom panel shows the late-time excess, obtained by subtracting the SDSS host galaxy spectrum from the observed late-time spectrum. A smoothed spectrum is shown in blue. The smoothing was done using a rolling kernel of size 5 to average over the values. The red lines are a simple TDE model with Milky Way and some amount of host galaxy extinction applied (the amount is shown in the legend), in order to get the approximate shape of the observed spectrum. Narrow emission and absorption lines that were notable in the unsubtracted spectrum are marked with dashed lines. The grey regions are affected by sky lines, and should be ignored. The late-time spectrum of SN 2020alm is available in electronic form at the CDS via anonymous ftp to cdsarc.u-strasbg.fr (130.79.128.5), via http://cdsweb.u-strasbg.fr/cgi-bin/qcat?J/A+A/ or upon request to the author.	77
3.15	Binned SMP light curves of the three candidate objects. As no bins $\geq 5\sigma$ are recovered in SN 2018grt, it is not shown here. Both SN 2019ldf and SN 2020tfc do however still have robust detections in some bands. The best fitting alternate transients, shown in dotted lines, are the same as in Fig. 3.11. The i -band of SN 2020tfc is not shown as the background was not subtracted completely, resulting in a significant flux offset. . . .	78

List of Tables

3.1	Initial sample size and its reduction in each step of the analysis process.	23
3.2	List of objects that passed the initial visual inspections.	37
3.3	Objects with a detected sibling transient.	40
3.4	Results of the additional tests for the ten promising objects. The host separation is given in " and converted to kpc using the redshift given in Table 3.2 and the same cosmology as was used in Sec. 3.2.4.4. In the final five columns the similarity of each SN Ia with a late-time excess is compared to different transient classes to see if the late-time signal can be interpreted as another transient. This can be excluded based on an inconsistent colour (1), duration (2), and/or an excessive amount of host extinction (3) needed to obtain the observed magnitudes.	45
3.5	Details of the comparison transients used to test if late-time detections could be explained by another transient at a similar sky position. The first column shows the assumed type of transient, the second shows the transients used to represent each type, the third has the approximate absolute extinction-corrected r -band peak magnitudes, and the fourth the reference for each event.	47
3.6	Parameters used for rate estimation simulations for each object.	60
3.7	Spectra used to make the SN 2011fe model. All spectra were taken from WISEREP (Yaron & Gal-Yam, 2012).	72
3.8	Redshift values where 50 per cent of the simulated SNe were found to have CSM interaction. Strength is the strength of the $H\alpha$ line compared to the strength detected in SN 2015cp. Start shows how many days after the peak the interaction begins, and duration is in days as well. We fitted sigmoid functions to the results of each simulation in order to find the redshift where 50 per cent of the interactions were recovered, assuming the reference images were of the same depth as the ones used in ZTF or 0.5 or 1 mag deeper. These values are shown in $z_{50} \pm \sigma_{z_{50}}$, and χ^2_{red} shows the quality of the fit.	75

Introduction

1.1 The final stages of stars

1.2 Type Ia SNe

Somewhere state that while I focus on interaction in SNe Ia, this search can be broadened, as is done in paper II

To convert between apparent and absolute magnitude I assume a flat Λ CDM cosmology with $H_0 = 67.7 \text{ km s}^{-1} \text{ Mpc}^{-1}$ and $\Omega_m = 0.310$ (Planck Collaboration et al., 2020) throughout this paper, unless specified otherwise. Do I use another one anywhere?



Figure 1.1: *gri* composite image of NGC4216 using observations taken by the Zwicky Transient Facility. **Left:** composite image of observations taken before 1 January 2024. **Right:** composite image of observations taken between 5 and 19 January 2024, the first two weeks after the first detection of the Type Ia SN 2024gy. (Credit: Benjamin Nobre Hauptmann) Use this as an example when introducing transients

Observing in the optical regime

To do list: Add refs, run by NOT for sanity check, get consistent with g vs g' (ask at NOT), sometimes slightly confused which tense to use, recheck carefully, opmaak, reference about the LP light pollution restriction laws? mention gain (e^- / ADU conversion) and read noise (mean e^- added per pixel at readout) as well somewhere.

Astrophysicists face the challenge of not being able to set up and control their experiments. The universe is our laboratory but all we can do is see or detect the results while often not knowing the exact setup of the experiment. Models are made to explain and predict the behaviour of planets, stars, galaxies, etc. but ultimately observations are needed to compare against and test our models. My work relies heavily on observational data, and in this chapter I will introduce the different types of observations that are used throughout this thesis (section 2.1), telescopes and instruments that are used to obtain these observations (section 2.2), and a quick overview of how to calibrate the raw images and extract useful data (sections 2.3 and 2.4). I will also give a general overview of what to consider when planning observations in section 2.5.

2.1 Types of observations

All optical observations are, in essence, images taken by a camera. Light falls onto a pixel on the detector, a charge-coupled-device (CCD), and frees some amount of electrons. The more light that hits the pixel, the more electrons are freed. At readout these electrons are counted per pixel, or group of pixels if binning is applied, and turned into a digital number called a count. During this process there are contributions from different noise sources, but as long as the total count rate is in the linear regime of the CCD there is a linear relation between the received flux and final count. It is then possible to calculate the observed flux from the target by using calibration images. The different types of calibration images are described in section 2.3 and their usage is explained in section 2.4 when discussing image reduction.

2.1.1 Photometry

Photometry is one of the simplest observing modes as it is just taking a photo of a part of the sky. The top of Fig. 2.1 shows a raw photometric image, taken with ALFOSC on the Nordic Optical Telescope (NOT) without the use of a filter. The images are monochromatic, i.e. they only have a value for the intensity. For colourful images multiple observations have to be made using different filters and combined to represent different colours. Faint objects can be observed by increasing the exposure time in a single image, or by stacking multiple images together to increase the effective exposure time. Stacking images can be useful for e.g. reducing cosmic ray interference, avoiding overexposure of a bright source close to a fainter target, or for constructing time series. When stacking images it is common practice to dither the telescope: applying a small offset between exposures to ensure that the target hits a different part of the CCD to avoid issues with bad pixels ruining otherwise good observations. While this decreases the effective size of the fully stacked image, as long as the edges are not needed there is no issue.

2.1.2 Spectroscopy

Spectroscopy goes one step beyond just taking a photo. Assuming that this is slit spectroscopy, instead of a filter to select a wavelength range to observe now a slit restricts the observable region of the sky to a narrow band along one axis of the detector (e.g. horizontal). After the slit the light hits a grating or grism (a grating and prism combined) which diffracts the light based on wavelength across the second axis of the detector (vertical). The rule density on the grating / grism dictates the wavelength spread of the light: the more rules per unit distance, the bigger the diffraction, and the higher the spectral resolution of the resulting image. The tradeoff is that a smaller part of the spectrum can be observed at a time, and there is less light being received per pixel which reduces the SNR unless the exposure time is increased to account for this. Any point-like source that is observed becomes a line in the spectral direction,

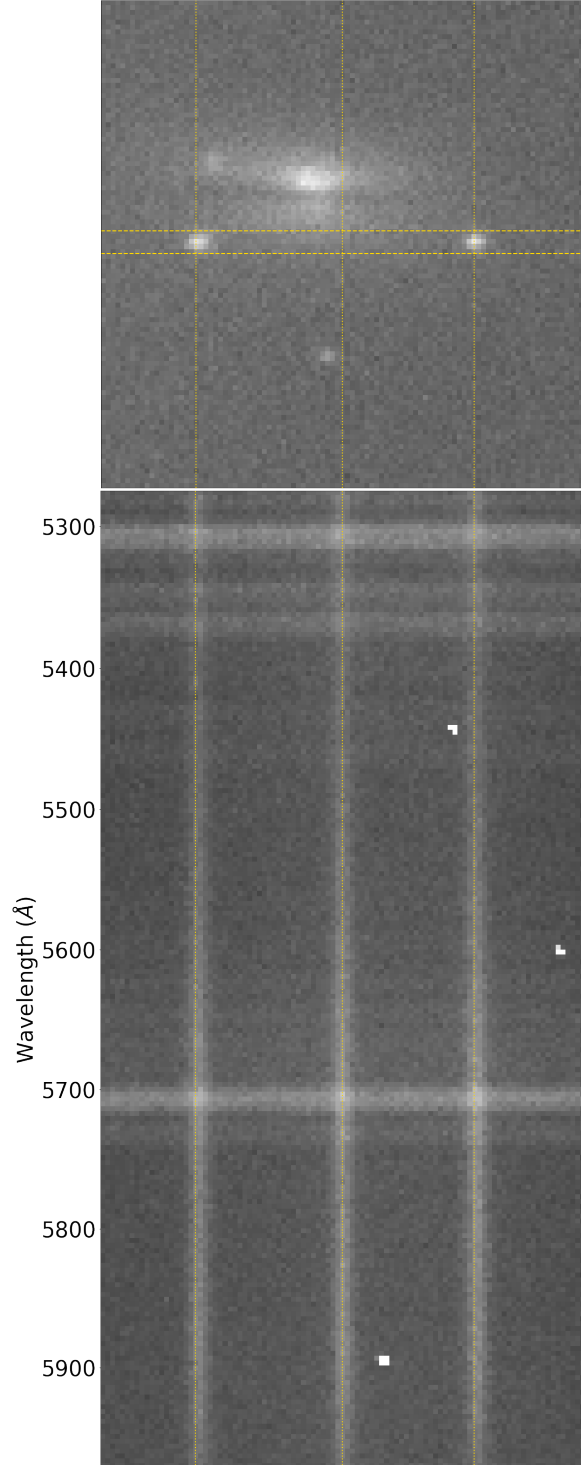


Figure 2.1: Image and partial spectrum of SN 2024nqr (left) and SN 2024pgd (right), two SNe Ia active simultaneously in the same galaxy. The image was taken without a filter and used to align the $1.0''$ slit (horizontal dashed lines) over both SNe. The resulting spectrum, taken with grism #4, shows three traces as white vertical stripes. The outer two line up with the two SNe, while the middle trace is from the host galaxy edge in the slit (vertical dotted lines for guidance). The horizontal lines in the spectrum are sky lines coming from atmospheric emission, and the white spots in the spectrum are due to cosmic rays. This data was taken with NOT/ALFOSC on the night of 28 July 2024 while testing an experimental rapid response mode (RRM, credit: Samuel Grund Sørensen). [check AT/SN status weirdness](#)

called a trace. Extended sources create extended traces.

There is some freedom in the orientation of the slit. This is called the position angle of the slit. If there are multiple targets near each other, and they can be in the slit at the same time, the required position angle can be calculated from the two target positions. If there is a single target to be observed the position angle can be anything, but usually the parallactic angle is chosen. In this orientation the slit is perpendicular to the horizon, and prevents losses from differential diffraction (different colours diffracting differently when entering the atmosphere at an angle, [Filippenko 1982](#)). The trace will only be slightly diagonal on the CCD.

The bottom panel of Fig. [2.1](#) shows a section of the spectrum taken of the SNe in the top panel image. The two SNe are drawn out into vertical traces and a third trace belonging to the edge of the host galaxy can be seen in the middle. The horizontal lines are sky emission lines, and while these can technically be used to estimate the conversion from pixel position to wavelength, standardized arc frames will result in a much better wavelength calibration (see section [2.4](#)).

2.2 Telescopes

Most of the data used in this thesis comes from the Zwicky Transient Facility (ZTF), and follow-up observations have been made using the Nordic Optical Telescope (NOT), and the Gran Telescopio Canarias (GTC), which will be introduced below. Some additional data comes from other sources, which are listed for completeness. The same filter names (*gri*) are used for filters at different telescopes, which have slight differences. In the rest of this thesis I will use *grito* to refer to the ZTF filters, unless specified otherwise. [gotta make sure this is done correctly everywhere](#)

2.2.1 Zwicky Transient Facility

The Zwicky Transient Facility (ZTF, [Bellm et al. 2019a,b](#); [Graham et al. 2019a](#); [Masci et al. 2019](#); [Dekany et al. 2020](#)) is an optical large-sky survey observing the entire

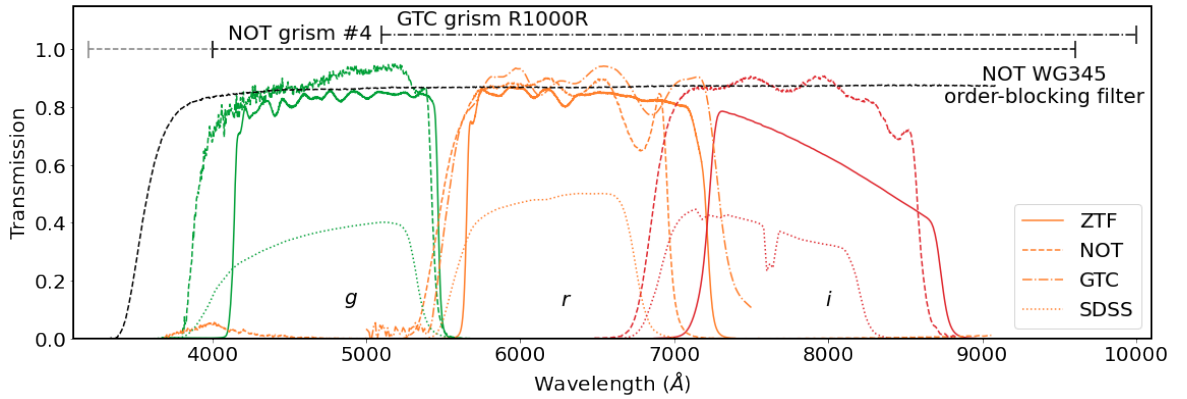


Figure 2.2: Throughput as a function of wavelength of the different filters used to gather the bulk of the data in this thesis g filters are shown in green, r in orange, i in red, and the different telescopes are shown with different line styles (Continuous for ZTF, dashed for NOT, dot-dashed for GTC). The SDSS filters (dotted lines) are shown for comparison. For the grisms the wavelength ranges are shown as only, not their efficiency at each wavelength.

northern night sky above Dec $\approx -30^\circ$ every 2 to 3 nights in three broadband optical filters g ($\lambda_{eff} = 4746.48 \text{ \AA}$), r ($\lambda_{eff} = 6366.38 \text{ \AA}$), and i ($\lambda_{eff} = 7829.03 \text{ \AA}$), which are similar to the well-known SDSS gri filters. The efficiency of these filters is plotted as a function of wavelength in Fig. 2.2. The survey saw first light in October 2017 and the survey formally began scientific operation in March 2018, and has been running continuously until the time of writing this document.

The observations are made using the $48''$ aperture Schmidt-type design Samuel Oschin Telescope, which is based at the Palomar Observatory in Southern California. Each exposure is 30 s long, can go to a limiting magnitude of ~ 20.5 mag and covers an area of $\sim 47 \text{ deg}^2$ at a resolution of $1.01''$ per pixel. The camera is divided in a 4×4 grid of CCDs, each of which have 4 readout channels called quadrants. This results in each observation producing 64 separate images, each with their own readout channel identifier (rcid). Similarly, the observed region of the sky is divided into different telescope pointings called fields to ensure that the same region of the sky is observed in the same way each time, aiding with the reduction of the data. This results in each combination of filter, field, and rcid being a set of observations of a particular part of the sky using specific setup.

2.2.2 Nordic Optical Telescope

The Nordic Optical Telescope (NOT ¹) is a 2.56 m telescope located at Observatorio Roque de Los Muchacos in La Palma, Spain, at an elevation of 2382 m above sea level. It hosts several instruments for observing in the optical and near infrared, both for imaging and spectroscopy. The Alhambra Faint Object Spectrograph and Camera (ALFOSC) was used to obtain the data used in this thesis. I will only discuss the parts relevant to this thesis, further details on this instrument and details on the other instruments can be found at the NOT website.

ALFOSC is a versatile instrument mounted in cassegrain and can be used for imaging, spectroscopy, and (spectro)polarimetry. As there are several wheels equipped to hold a variety of optical elements, the instrument can switch quickly between different setups between observations. The images can cover up to $6.4' \times 6.4'$ per exposure at a resolution of $0.2138''$ per pixel. In this thesis g ($\lambda_{cen} = 4800 \text{ \AA}$), r ($\lambda_{cen} = 6180 \text{ \AA}$), and i ($\lambda_{cen} = 7710 \text{ \AA}$) are used for photometry. For spectroscopy grism #4 is used to split the light vertically, together with a horizontal $1.0''$ slit if the seeing was $\leq 1.3''$ or a horizontal $1.3''$ slit if the seeing was $\geq 1.3''$. Grism #4 has a resolution of $3.3 \text{ \AA pixel}^{-1}$ and an wavelength range from 3200 \AA to 9600 \AA , but as the response at short wavelengths is poor, the spectra used in this thesis are cut at 4000 \AA . For some spectra an order-blocking filter (WG345) is used as well to avoid second order diffracted blue light to overlap with first order diffracted red light on the detector. The transmission curves of the filters and wavelength range of the grism are shown in Fig. 2.2.

2.2.3 Gran Telescopio CANARIAS

The Gran Telescopio CANARIAS (GTC ²) is a 10.4 m telescope at Observatorio Roque de los Muchachos in La Palma, Spain, and is the largest optical / near infrared telescope on the island. Its primary mirror is made up from 36 hexagonal pieces creating an effective collection area of 73 m^2 , ideal for observing very faint targets. The GTC

¹<https://not.iac.es>

²<https://www.gtc.iac.es>

can host up to six instruments at a time in various focal positions, allowing for a large variety of observations to be made. One of the most commonly used instruments is OSIRIS+, the upgraded version of OSIRIS: the Optical System for Imaging and low-Intermediate-Resolution Integrated Spectroscopy.

OSIRIS+ has an unvignetted field-of-view of $7.8' \times 7.8'$ at a resolution of $0.254''$ per pixel. Since the standard readout has 2×2 binning, the resolution can be increased to $0.127''$ per pixel if so desired. Like ALFOSC, this instrument is also built to easily switch between different setups between observations. For photometry the $r(\lambda_{cen} = 6410 \text{ \AA})$ filter is used in this thesis, and for spectroscopy the R1000R grism with a $1.0''$ vertical slit is used. R1000R splits the light horizontally over the detector with a range of 5100 \AA to 10000 \AA with a resolution of $2.62 \text{ \AA pixel}^{-1}$. These filter transmission curve and grism wavelength range are shown in Fig. 2.2.

2.2.4 Other observations

Small amounts of data coming from other telescopes and surveys are presented in this thesis as well. This includes a follow-up observation of SN 2019ldf in section PUT REFERENCE ONCE SECTION IS IN in g and r using the ESO Faint Object Spectrograph and Camera version 2 (EFOSC2, Buzzoni et al. 1984) imaging spectrograph on the ESO New Technology Telescope (NTT) in La Silla, Chile as part of the extended Public ESO Spectroscopic Survey of Transient Objects+ (EPESSTO+, Smartt et al. 2015).

To complement ZTF data of several SNe, in chapters PUT REFERENCES ONES SECTIONS ARE IN, MIGHT BE DIFFICULT TO DO SECTION SPECIFIC FOR THIS optical photometry from the Panoramic Survey Telescope and Rapid Response System (Pan-STARRS, Chambers et al. 2016), (intermediate) Palomar Transient Factory (PTF, Law et al. 2009; Rau et al. 2009, iPTF, Kulkarni 2013), All Sky Automated Survey for SuperNovae (ASASSN, Shappee et al. 2014; Jayasinghe et al. 2019), Asteroid Terrestrial-impact Last Alert System (ATLAS, Tonry et al. 2018), and Global Astrometric Interferometer for Astrophysics (Gaia, Gaia Collaboration et al. 2016) are used,

as well as near-infrared photometry from the Wide-Field Infrared Survey Explorer (WISE, [Wright et al. 2010](#)).

2.3 Calibration images

Before the observations can be used for science, the images need to be calibrated. This is done using different types of calibration images, each of which measure and correct for different effects of the telescope and detector. Usually these are taken during the day or twilight so no valuable observing time is lost. It is standard practice to take multiple calibration images and use an odd number in the reduction to find median values and remove interference from e.g. cosmic rays, this is called a master image.

2.3.1 Bias

The first type of calibration image is the bias, which is made by reading out the CCD without exposing. The resulting image contains the amount of counts that will be in every exposure regardless of what has been observed or with what exposure time. In other words, measuring the bias can be thought of as measuring the offset to correct for in every other image.

2.3.2 Dark

Any detector that is not at a temperature of 0 K will have some amount of noise due to thermal effects. This can free electrons in pixels over time, creating a dark current and increasing the noise over time. The effect can be measured by exposing for the same amount of time as the science images taken, but without letting any light hit the CCD. This is called a dark frame.

As this is a thermal effect, it can be reduced to negligible amounts by cooling the instrument. This saves precious observing time, as otherwise dark frames would ideally have to be taken at the same temperature as the target was observed, which is easiest to do directly after the science exposure. By cooling the detector with e.g. liquid

nitrogen this noise source can be avoided instead of having to correct for, saving time and the amount of images that need to be taken in the process.

2.3.3 Flatfield

The amount of light that the telescope receives is converted into a digital number, but there is no guarantee that this conversion rate is the same for each pixel. This can be due to intrinsic differences between the pixels, or outside effects such as dust reducing the amount of light recieved on a part of the detector. To correct for this an evenly illuminated field has to be observed, resulting in an image called a flat or flatfield. By ensuring that each pixel receives the same amount of light, the different counts will reflect the varying responses per pixel.

Any evenly illuminated object can be used for this, such as the the inside of the telescope dome to create dome flats. A more perfect evenly lit source however is the sky, and using this sky flats can be taken. While it is usually too bright during the day and the CCD will saturate even with the narrowest filter and shortest exposure time, there is a window during twilight where the sky is darker but not dark enough to observe stars yet, perfect for taking flats. As a general rule, narrowband filters need a brighter sky and in the evening these need to be done before the broadband filters. After that, assuming similar efficiencies between filters, blue filters need brighter skies than red filters, forcing a specific order in which the sky flats need to be taken during the short window where this is possible. Of course if flats are taken in the morning the order has to be reversed.

2.3.4 Arc

In spectroscopy one of the axes has low wavelength at one end and high wavelength at the other end of the image. To know where each wavelength falls on the detector, arc frames are needed. These are taken by observing a lamp filled with a known set of elements (e.g. He, Ne, or TH and Ar). The wavelengths of the emission lines are

known very precisely, and by matching these with the observed lines in the arc image a pixel-to-wavelength conversion can be found, called the wavelength solution.

Usually arcs can be taken during the day, when the telescope is idle. However in some cases the mechanical flexure of the telescope, caused by being in a different position during observing, can introduce an uncertainty in the wavelength calibration unless an arc is taken with the telescope in the same position as for the target. In these cases an arc is usually taken directly before or after the target is observed, or between exposures of the target.

2.4 Reduction

After all observations have been taken it is time to analyze them. The first step is to reduce the raw data into the required format to work with. After that, additional analysis technique can manipulate the reduced images directly or the data that has been extracted from them. The response function of a detector can be written as

$$R_{ij}(f, t, \lambda) = B_{ij} + D_{ij}(t) + F_{ij}(\lambda) \times f \times t, \quad (2.1)$$

where R_{ij} is the CCD response of pixel i, j as a function of the integrated flux of the target $f \times t$ during the exposure which lasted a time t . The goal is to measure the flux f , which requires knowing and correcting for the bias level B_{ij} , dark current D_{ij} , and pixel response F_{ij} . Each type of calibration image is used to measure one of these values. Note that it is assumed that there are no cross or higher order terms in Eq. 2.1, in other words, the CCD is in its linear regime. When a pixel receives too much light and gets close to saturation it is no longer in its linear regime, and more terms appear in Eq. 2.1 making it much more difficult or even impossible to measure the observed flux.

2.4.1 Bias, dark, and flat corrections

Using the calibration images from section 2.3, the raw science images can be reduced to something a flux level can be measured from.

First the master-bias is created and subtracted from every other image. As both F and t are 0, the bias measures B_{ij} directly and can then immediately be removed.

With the bias gone, the dark frames measure D_{ij} for a specific t , but the master-dark can only be used on science observations with the same exposure time. Alternatively it is possible to subtract $B_{ij} + D_{ij}(t)$ in a single step by not separating out the bias term using bias images first.

Finally every science image is divided through the normalized master-flat to equalize the pixel responses. There is still a factor $F(\lambda)$ present as the detector efficiency is wavelength dependent, but the value is now independent of the pixel position, allowing values from across the CCD to be compared.

2.4.2 Cosmic-ray removal and image stacking

At this point it is often good practice to run a cosmic-ray removal algorithm to remove this source of noise as much as possible. This can be done using e.g. L.A.Cosmic (van Dokkum, 2001), which I used through Astro-SCRAPPY (McCully et al., 2018) when reducing follow-up photometry of several objects in this thesis.

If multiple images are taken of the same field or object they can be stacked to reduce background noise and increase the SNR of the observed objects. Sometimes the observations have been taken with dithering to avoid the same objects being on the same pixels in every exposure, which has to be taken care of to make sure that the images are stacked correctly.

2.4.3 Standard star calibration

Filters are never 100% transparent at any wavelength, and the CCD responds differently to different wavelengths as well. To correct for this, one last type of calibration

image is used: the standard star. This was not mentioned in section 2.1 as observing a standard star is exactly the same as observing the actual science target. The only difference is that the expected result of the observation is known and can be used to correct for the wavelength dependent efficiency of the instrument.

With photometry the observed brightness can be measured for each star in the image to get a list of instrument magnitudes. The relative differences between the magnitudes of objects are correct, but there is still an absolute offset across all objects. This is corrected by finding the offset using the standard star. If the filter is commonly used, there is a good chance many stars in the field have known magnitudes in that filter, which can be used for calibration instead of a dedicated standard star.

In spectroscopy the arcs are used to find the wavelength solution for the spectra, after which the trace from the standard star can be extracted and divided by the known spectrum of the star to obtain the sensitivity function of the detector $F(\lambda)$. The trace of the target can be extracted as well to get its spectrum, which can then be flux-calibrated using the sensitivity function. In some cases only a relative sensitivity function is known, resulting in a calibrated spectrum in an unknown flux unit. In these cases proper calibrated photometry of the object can be used to flux-calibrate the spectrum by integrating the spectrum over the filter transmission curve.

2.4.4 Forced photometry

The two most common methods to measure flux from a source in a photometric image are PSF photometry and aperture photometry. A good explanation of these can be found in [Da Costa \(1992\)](#). PSF stands for point spread function, and with this method a function is fitted to model the source. This function describes how an infinitely small point of light is spread over the detector, and through its spatial size and peak value the flux of the light source can be measured. Aperture photometry sums up the signal in a given radius around the source center and subtracts the contribution from the background in the same region.

Large surveys such as ZTF observe the night sky to find new transients and monitor

known ones. Difference imaging is used to subtract constant sources and reveal active transients, as these are the main sources that should be left in the difference image. Through PSF photometry the location and strength of each source in the image is determined, which are then compared to the locations of known sources to separate new from known ones. Each location has however been observed for the entire duration of the survey, which means that it is also possible to measure the flux of a known transient before and after it was visible in the images, creating a light curve for the full duration of the survey.

This is called forced photometry, because the PSF function is forced to center on a specific location instead of finding the best-fitting position for the centroid. When there is nothing but noise at that location the measured flux will be 0 within the error. When there is a source at the target location it will be measured, but if the source is not at the center of the PSF the fit will have trouble converging, resulting in a large uncertainty. Artefacts such as cosmic rays, imperfectly subtracted difference images, or light bleeding effects from saturated bright nearby stars can also affect the accuracy of the photometry measurement. **Not completely happy with talking about difference imaging without really introducing it, introduce it here so can keep it bit higher level, mention ZOGY, HOTPANTS, Autophot**

2.5 General considerations for observing

During my PhD I have spent two years doing studentships at the Isaac Newton Group of Telescopes (ING) and Nordic Optical Telescope (NOT) on La Palma, gaining first-hand experience with the specifics of observing in the optical regime and the considerations that come with it. I will briefly go over these in this section.

2.5.1 Location

Although this is normally already done before constructing a telescope, the first thing to consider is the observing location. When purely aiming for the best observations

possible, there are three main things to consider when choosing where to observe from:

- Weather: Clear, stable sky conditions for most nights of the year, and low atmospheric distortion (e.g. seeing) are vital to ensure good quality data on a regular basis. Low hanging clouds can be avoided by being high above sea level, while simultaneously decreasing the amount of air light has to travel through to reach the detector, decreasing atmospheric influence.
- Light pollution: Darker skies allow observations of fainter objects. Even the presence of a (partially) illuminated moon significantly changes the depth that can be reached with the same exposure time. Many observatories have (inter)national laws to control the light pollution and ensure good quality data can be obtained.
- Target observability: The target location needs to be reachable by the telescope to be observable. The closer to zenith an observation is made, the less atmosphere between the target and telescope. The atmosphere reduces the data quality through turbulence (seeing), broadband absorption (clouds, dust), narrowband interference (tellurics, skylines), and differential diffraction, among others.

Observatories should be located on top of high mountains in areas with stable and clear weather, with as small a nearby population as possible while still being accessible enough for transporting materials and observing staff. One of the best locations in the world that meets these requirements is Roque de los Muchachos on La Palma, a small Spanish island in the Atlantic ocean off the coast of Morocco. At around 2300 m above sea level, the telescopes are built on the highest peak of the mountain far from most communities on the island which are much closer to sea level, and the temperate climate ensures good sky conditions for most nights around the year. Additionally, the government has put laws in place to minimize light pollution, e.g. by limiting the use of street lights and restricting flight paths over the island. **I remember a plaque at the roque mentioning this, maybe it has a good ref?**

2.5.2 Telescope, instrument, observation type, and setup

Depending on the type of observations and the brightness of the target there is a choice of hardware to be used. Telescope, instrument, observation type, and desired setup(s) have to be considered together, as some choices will affect other ones.

Bigger telescopes can observe fainter targets, but it is also more difficult to obtain observing time. On the other hand, smaller telescopes are less oversubscribed (a measure of requested versus available observing time), but are more limited in observation depth even with long exposure times.

Secondly, different instruments, which are often telescope specific, have different observing capabilities. Photometry and spectroscopy are very standard observing modes, and most telescopes have at least one instrument can offer this. Even though ALFOSC and OSIRIS+ can both of these modes, there are still differences in data quality and resolution even if the same object is observed at the same time. However for polarimetric observations for instance, OSIRIS+ cannot be used while ALFOSC can, limiting the options for this observation mode.

Lastly, the specific setup has to be considered as well. For photometry, which filters are desired? If a very specific or rare filter is needed this may limit the options of telescopes and instruments. For spectroscopy there are other choices, such as fiber or slit spectroscopy, different gratings or grisms depending on the desired resolution and wavelength range, neutral density filters to observe targets that are otherwise too bright for the instrument, and order-blocking filters to remove second order blue light from red parts of the spectrum.

2.5.3 Night plan

Lastly, it is good to have a plan of what to observe at each point during the night in order to avoid losing observing time during the night. Most proposals already have a list of targets and standard stars to observe and exposure times when they are submitted to request observation time, but the detailed plan is usually made mere hours before

the night starts as it depends on e.g. the current weather, target priority, and specific time constraints (e.g. for transits). Calibration images might need to be taken during the night as well. All of these things need to be considered when trying to maximize the time used to expose and observe targets, and minimize the overheads from e.g. positioning, target acquisition, and readout.

Time spent repositioning the telescope can be reduced by finding the path between targets that minimizes telescope and dome movement throughout the night. The target acquisition time depends on the type of observation, but also on the experience and tiredness of the observer. With photometry a field is observed, so usually a small offset is not disastrous for the science. With spectroscopy the target needs to be identified and placed in the slit or fiber before the exposure can start, costing extra time. Readout times are detector specific, but can be sped up by windowing and binning if only a part of the CCD is needed, and a worse resolution is acceptable. Considering readout times can be especially important when multiple shorter exposures are taken instead of a single long one.

Nothing is certain during the night. Weather conditions can change suddenly, technical problems can occur, a high priority target can be discovered during the night, or observations might go so smoothly that they are completed faster than expected. A flexible schedule with a priority list and backup targets helps adapting to these situations quickly. After all, an idling telescope in (half-)decent observing conditions is a waste of resources. Fig. 2.3 shows an example night plan for the NOT with some space for adaptability built in.

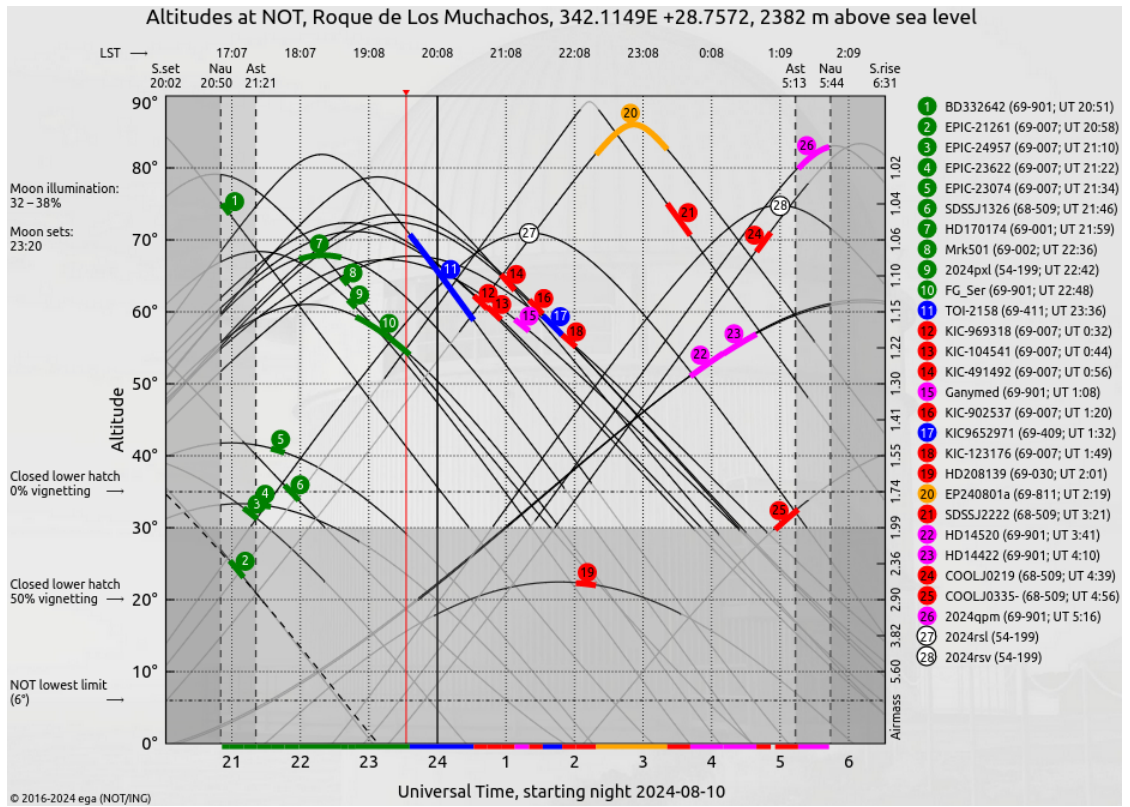


Figure 2.3: Night plan for the NOT on the night of 10 August 2024. Targets are plotted with their altitude as a function of universal standard time. Local stellar time is shown on top. The target priority has been colour coded, with the coloured bars showing the amount of time each observation is expected to take. Green targets have already been completed, and the red vertical line shows the current time. Several unscheduled backup targets are shown in case the plan has to be updated during the night.

ZTF SN Ia DR2: Searching for late-time interaction signatures in Type Ia supernovae from the Zwicky Transient Facility

This is Paper I, but needs to be properly adapted. Copied starting from Data until the end of conclusions and appended the appendix straight afterwards. To-do list: Check for broken references, check for double refs, reformat pages, add chapter introduction, expand SNAP section, make sure all the *gri* things are consistent

This chapter details my search for late-time interaction signals in the ZTF second data release (ZTF SN Ia DR2, Rigault et al. in prep.; Smith et al. in prep.) and has been published in Terwel et al. (2024). Chapter 3 contains the same details as the paper but expands on Sect. 3.2.3. Not sure what to put in this introduction, also need to actually expand on the snap section

3.1 Data

Our aim is to look for late-time (>100 d after peak brightness) signatures of CSM interaction in the largest sample of SNe Ia to date. This has been obtained by the ZTF. We are particularly interested in events that appear to be normal SNe Ia from their spectra and light curves around the peak but may display signs of late-time interaction, as seen in SN 2015cp (Graham et al., 2019b). Our starting sample is 3 628 events that were discovered by ZTF from March 2018 to October 2020 (hereafter the ZTF data release 2, ZTF DR2). Each event is spectroscopically classified as a SN Ia or one of its sub-classes. An overview of the ZTF DR2 will be presented in Rigault et al. (in prep.), including the sample definition, properties, and use for cosmology. In this study, since we are searching for likely rare signatures of interaction in the ZTF light curves, we are as inclusive as possible in our sample definition and include all SNe

Ia in the DR2 covering a redshift out to $z = 0.288$.

3.1.1 ZTF light curve data

ZTF observes in three optical bands *gri* on a 2 – 3 day cadence. Reference images, mainly made using observations at the start of ZTF, are subtracted from the science images using the ZOGY image subtraction algorithm (Zackay et al., 2016) to produce difference images. We use forced photometry at the transient location on the difference images using ZTFPS (Reusch, 2020) to get a measure of the observed flux at each epoch. This includes non-detections before each SN was first detected and after each SN has faded below detection limits.

Light curve quality cuts on specific light curve points are applied as in Smith et al (in prep.). We do not correct the light curves for Milky Way extinction in our initial analysis but do consider it when focussing on specific objects of interest in Section 3.3.

Another approach for extracting photometry at the transient location is by using Scene Modelling Photometry (SMP; Holtzman et al., 2008). We extract SMP for a few selected objects of interest in Section 3.3 to test if the identified late-time detections are independent of our approach. When using SMP, one has to define an ‘off’ time and an ‘on’ time. The observations taken during the off time are used to create a model of the region, or scene, where the SN occurs. This is then used as a template during the on time to calculate and remove host contributions to the photometry, leaving just the transient itself (Lacroix et al. in prep.). The advantage of this method is the significantly lower uncertainty in the model compared to the difference imaging technique, allowing us to find fainter detections. Since we assume that a signal from late-time interaction could occur at any point after the SN, we define the off time as everything up to shortly before the SN explodes, and the on time as everything after this moment.

3.1.2 Baseline correction

Issues in the construction of the reference images such as inaccurate flat-fielding or artefacts in the images that are subsequently co-added can result in a systematic offset in the forced photometry light curve made using different images. The technique of baseline correction is used to correct for this (Yao et al., 2019; Miller et al., 2020).

To estimate the necessary baseline correction, we calculated the weighted mean of the flux of all data points up to 40 days before the estimated SN peak (which is assumed to be the highest flux detection deemed real), and subtracted it from the light curve. Baseline corrections are done separately for each combination of band (*gri*), field (telescope pointing), and rcid (part of the camera, which is arranged in 4×4 charge-coupled devices (CCDs) with four readout channels each, giving a total of 64 readout channels) as each of these combinations uses different, unique reference images. To be able to apply a baseline correction, at least two observations are needed. If this is not possible all observations with that band, field, rcid combination are removed.

Since we are interested in post-SN detections, our baseline correction method using only pre-SN data differs from the one used in Rigault et al. (in prep.) with both pre- and post-SN data. A comparison between the methods found that for most objects our corrections agree with the ones used in Rigault et al. (in prep.) within the uncertainties. This is as expected as objects with late-time flux excesses are expected to be rare, meaning that the two baseline correction methods should give the same result for most objects.

If there is insufficient data to perform a baseline correction, the relevant data (based on field, filter and rcid) is removed from the light curve. If this includes data around the peak position, the peak position in the light curve may change and therefore, the position of the peak is recalculated.

Table 3.1: Initial sample size and its reduction in each step of the analysis process.

Criterion	Removed	Objects left
Initial DR2 sample	-	3 628
No photometry at 100+ days	109	3 519
No robust late-time detections ^(a)	2 953	566
Presence of SN Ia tail ^(b)	432	134
Removed on visual inspection ^(c)	101	33
No late-time CSM interaction ^(d)	30	3

^(a)For a ‘robust detection’, at least four positive detections (two or more adjacent bins with $\geq 5\sigma$) are required out of the 16 possible combinations of bin size (25, 50, 75, 100 d), and the starting position of the bin varied by 25, 50 or 75 per cent of the bin size.

^(b)We tested for the presence of a radioactive tail of the SN Ia as described in Sec. 3.2.2 and removed those where this was the most plausible explanation.

^(c)Each remaining light curve was inspected using SNAP (Sec. 3.2.3) for possible issues causing late-time detections. See Sec. 3.3 for a discussion of the reasons events were removed.

^(d)For each remaining light curve we checked in detail if the late-time detections could be explained without CSM interaction starting at late times.

3.2 Analysis

To systematically search for objects with late-time flux excesses, a custom pipeline was developed. In Section 3.2.1, we describe how the late-time photometry for each object is binned to reach deeper magnitude limits, as well as the scheme used to select objects with robust, significant detections. In Section 3.2.2, we identify and remove bright nearby SNe Ia whose late-time detections are due to the SN radioactive decay tail. In Section 3.2.3, we describe our method of visually inspecting images of potentially interesting sources, and in Section 3.2.4, we detail our use of SIMSURVEY to simulate SNe Ia with late-time interaction signatures. Table 3.1 shows our sample size after each step of analysis that is discussed in the subsequent sections.

3.2.1 Binning & filtering programme

After pre-processing, the late-time observations are binned in phase to push the detection limit beyond the limit of the individual observations. We define late-time observations as being at least 100 days after the estimated date of SN peak brightness

in the observer frame. We remove all SNe Ia that have no data in any band beyond this phase. The exact choice of 100 days is arbitrary but was chosen as a balance between minimising spurious detections due to the light curves being dominated by SN light at earlier times and maximising the phase range over which the interaction can be searched for.

Binning of the light curves is performed in each band separately. Larger bins are better for pushing the magnitude limit as deep as possible, but they sacrifice temporal sensitivity. To balance the time sensitivity and magnitude limit, we use bins with widths of 100, 75, 50, and 25 days. To make sure that the placement of the bin edges does not affect our results, we repeat the binning four times for each bin size while adjusting the starting epoch of the bins by decreasing the size of the first bin by 25 per cent in each iteration. This results in a total of 16 trials for each band.

Each bin starts at the position of a data point to avoid empty bins. A gap in the data that is larger than the bins being used can cause the bins after the gap to always be placed in the same location despite the size modifications of the first bin. To avoid this we re-apply this modification of adjusting the size of the first bin after the data gap to trial different start positions. Lastly, if a bin would only contain one or two points, and the phases of these points occur no later than 10 per cent of bin size of the previous bin (e.g. if the bin size is 25 d, they would occur within 2.5 d of the end of the bin), the previous bin is increased in size to include these points. An example of the bin placement is shown in Fig. 3.1.

For each bin the weighted mean and uncertainty of the observed flux are calculated. When binning flux measurements taken from difference images, the uncertainty of the reference images used in the difference imaging procedure has to be considered, as this will limit the depth of the binned observations (Strotjohann et al., 2021) and this is added in quadrature to the weighted uncertainty of the binned flux.

After the binning procedure each light curve has undergone 16 trials per band across four bin sizes and four bin placements. An attempt in a specific trial is considered significant if it has two or more adjacent bins with $\geq 5\sigma$ detections. A late-time detection

is considered ‘robust’ if at least four out of 16 attempts have significant detections suggesting that the detections are insensitive to bin placement and/or size. We make this choice of robust detection in at least four attempts to ensure that we are not dominated by spurious detections but that we can still detect a long but faint signal that can only be picked up in the four trials involving the largest (100 day) bins.

3.2.2 Removal of SN Ia radioactive tail detections

For some nearby SNe Ia, the normal light curve tail powered by the radioactive decay of $^{56}\text{Co} \rightarrow ^{56}\text{Fe}$ is still visible at the phases investigated here (>100 d after the peak), possibly triggering false positives in our pipeline. To test if the fading tail is the reason for detections after 100 d, we checked if the detections follow a declining power law in flux space consistent with that of a normal SN Ia tail. We take all bins, normalise to the brightest data point, and fit a declining power law. To ensure that the tail matches the earlier data points, we include the unbinned observations between 60 and 100 d after the peak, making sure that if there are N bins only the latest $N/2$ unbinned detections are used to ensure that the fit focusses on the bins and not the unbinned points.

A successful fit of a declining normal SN Ia tail has a reduced chi-square of $\chi^2_{\text{red, fit}} < 5$ and fitted half-life of $t_{1/2}$ with uncertainty $\sigma_{t_{1/2}}$, satisfying $t_{1/2} - 5\sigma_{t_{1/2}} \leq 50$ d. We chose a threshold of 50 d as [Dimitriadis et al. 2017](#) showed that this is the approximate decay time scale for a normal SN Ia at these phases. A fit with a high $\chi^2_{\text{red, fit}}$ value could have failed due to bad or uncertain data, or due to the late-time detections not following a power law decay. Fits with a $t_{1/2}$ significantly larger than that of a normal SN Ia tail suggest an additional luminosity source contributing to the light curve at these phases. Figure 3.1 shows an example where this tail fitting procedure determines the late-time detections in an object to be a normal declining SN Ia tail. 432 SNe Ia that were flagged as having late-time detection are discounted from further discussion because their light curves can be explained by a normal fading SN Ia tail.

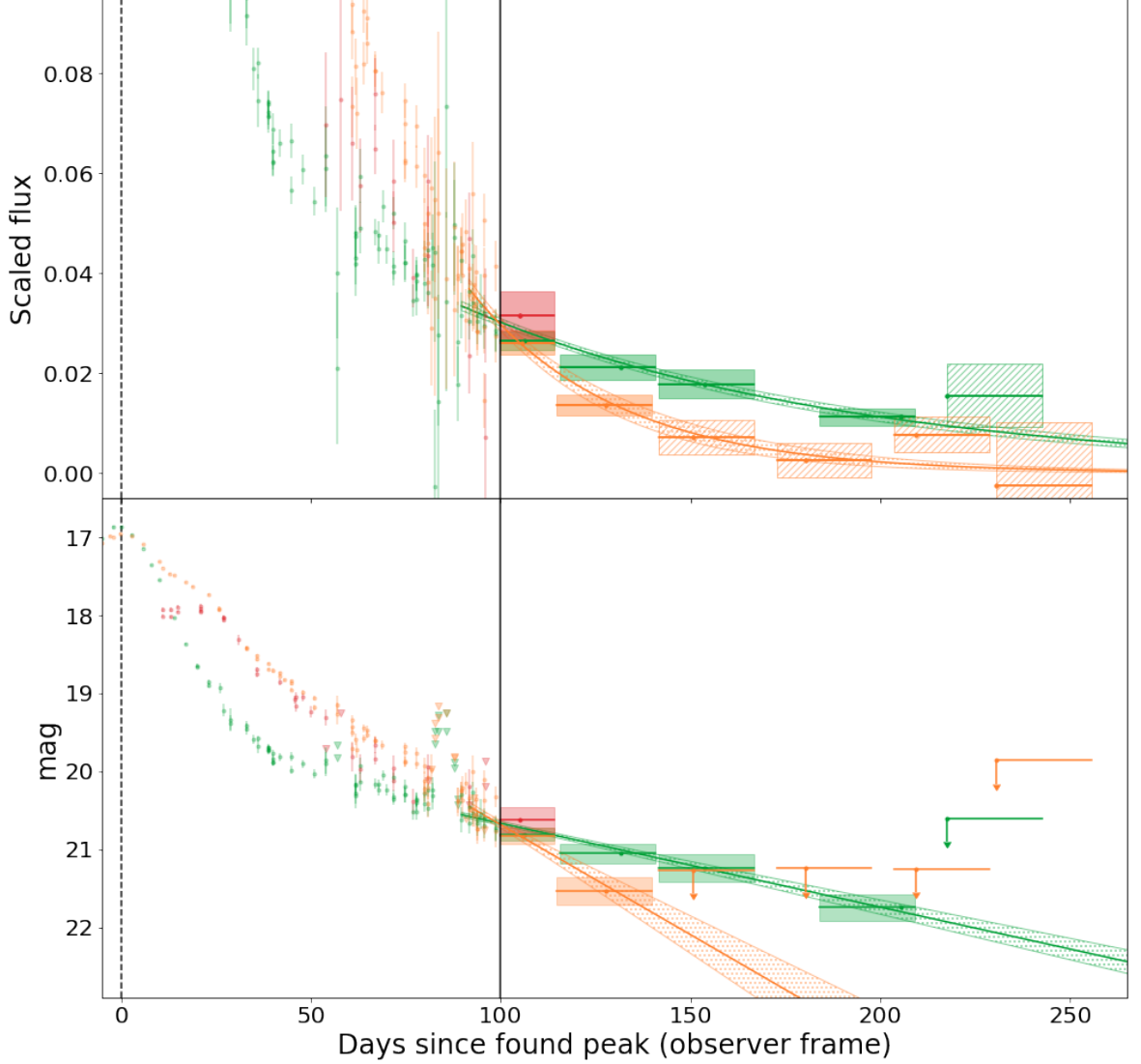


Figure 3.1: First 250 days of the *gri*-band light curves of SN 2019hbb in flux scaled to the peak flux (top panel) and magnitude (bottom panel) space. Binning starts 100 days after the estimated peak date (vertical black dashed and solid lines), using 25 d bins. The *g*-, *r*-, and *i*-bands are shown green, orange, and red, respectively. Before 100 days, we show the unbinned detections with their uncertainties (coloured circles) and non-detections (inverted triangles). After 100 days we show the bins as horizontal lines to show their size, a circle to show their mean value, and the shaded region showing the 1σ uncertainty (dashed regions are non-detections). A bin is deemed a non-detection if the flux $f < 5\sigma_f$. The 5σ magnitude limit is calculated and shown as a downward arrow. In both the *g*- and *r*-bands, the first bin is a detection and there are multiple adjacent bins with detections, triggering the tail-fitting procedure (see Section 3.2.2). The resulting tail fits are shown in the green and red lines, respectively, with their 1σ uncertainties as hashed regions. The half-life times are $t_{1/2,g} = 70 \pm 6$ d ($\chi^2_{\text{red}} = 0.6$) and $t_{1/2,r} = 27 \pm 4$ d ($\chi^2_{\text{red}} = 1.4$). This tail is therefore deemed to be a normal SN Ia tail.

3.2.3 SuperNova Animation Programme (SNAP)

After performing the binning and filtering, and removing SNe Ia with contamination from the radioactive tail, we are left with 134 SNe Ia with robust late-time detections (see Table 3.1). Since the binning and filtering programme is designed to handle a large quantity of light curves and cannot be tailored specifically to suit the peculiarities of a single object, it is possible that there are objects remaining with issues in the data or data processing (e.g. cosmic rays, bad subtractions), resulting in false positive detections. Therefore, we manually check the difference imaging to search for potential issues. To do this efficiently, we use SNAP¹.

Using ZTFQUERY (Rigault, 2018), SNAP takes all difference images of the requested sky position during the requested time period(s) in the requested band(s) and shows them in chronological order in an animation. At the start of each animation the reference images in all bands are shown. The programme can show the image in grey-scale, a three-dimensional wire-frame representation of the intensities measured per pixel, the averaged values along both axes of the image, the observation date and duration, the peak and mean pixel values of the shown region, the last spectrum taken before the currently shown image, and highlight the resulting forced photometry point in the light curve corresponding to the plotted images.

Using SNAP, issues in the difference images can be identified, including SN ghosts (the SN is visible in the reference image, leaving a negative imprint in difference images after it has faded), cosmic rays, and bad pixels (NaN, or a large negative number). Variability of a separate source can also be seen, which, when close by, can contaminate the forced photometry at the SN location, for example, an active galactic nucleus (AGN).

¹https://github.com/JTerwel/SuperNova_Animation_Program

3.2.4 Simulated interaction recovery fractions

To make sure the binning programme works as expected and estimate its detection efficiency in finding late-time signals, we simulated an observing campaign using SIM-SURVEY (Feindt et al., 2019a,b), a python package designed to simulate large scale time domain surveys such as ZTF. To successfully simulate an observing campaign, the programme needs to be told what, when, where, and how something is observed, and under what conditions. For this, we need a model of the SN Ia-CSM that is going to be observed, an explosion rate as a function of redshift, and a time range for these explosions to occur. We also require an observing log specifying which part of the sky is being observed at a specific time, the length of the observations, and the weather conditions during the observations. Lastly, we require details of the camera that is used to carry out the observations. The SN model needs to be in a similar format to the SNCOSMO models (a PYTHON package made for supernova cosmology, Barbary et al. 2021). This means we need a set of spectra over the entire phase range, all having the same wavelength spacing and range. Since no such model exists, we built our own model as described in the next section.

3.2.4.1 The interacting SN model

We chose SN 2011fe as the template of a normal SN Ia as it is well observed and close by (in M101 at a distance of 6.4 Mpc, Shappee & Stanek 2011). Optical spectra of SN 2011fe were obtained between phases of -18 to 1017 d relative to the peak. We made a custom model using SNCOSMO and spectra found on WISeREP (Yaron & Gal-Yam, 2012)¹, which are listed in Table 3.7. The spectra were flux calibrated to match the observed coeval broadband magnitudes. Spectra up to 45 d after the peak were flux calibrated using a SALT2 (Guy et al., 2007) fit of the *PTF48g* and *PTF48R*-band photometry (Law et al., 2009; Rau et al., 2009), which is used to estimate the flux in the *g*- and *r*- bands at these phases. Spectra between 45 and 400 d are flux calibrated

¹<https://wiserep.weizmann.ac.il>

using a cubic spline interpolation of photometry in the *PTF48g*- and *PTF48R*-bands. The interpolation extends up to 600 d after the peak in the *PTF48R*-band, there is no *PTF48g* photometry used between 400 and 600 d after the peak. Three interpolated photometry points from the SALT2 fits were used as anchor points to connect these two parts of the calibration. [Dimitriadis et al. \(2017\)](#) show that there is a slight kink in the light curve tail around 600 d after the peak. This is replicated in the model by calibrating all spectra more than 600 d after the peak using a cubic spline interpolation of photometry from the Large Binocular Telescope (LBT; [Hill et al., 2006](#)) in the Bessel *R*-band ([Shappee et al., 2017](#)).

After flux calibration, the spectra were dereddened to remove dust extinction effects, using the [Cardelli et al. \(1989\)](#) extinction law with $A_V = 0.04$ mag ([Patat et al., 2013](#)). The spectra were rebinned, and any wavelength region that was not covered in all spectra was removed as required by SIMSURVEY. Lastly, the model is corrected for distance, redshift and time dilation. The resulting model is that of a normal SN Ia, which exploded at a distance of 10 pc without any dust between the source and observer.

The best late-time detection of CSM in a normal/91T-like SN Ia was for SN 2015cp, where $H\alpha$ emission was identified in its spectra at 664 d after light-curve peak ([Graham et al., 2019b](#)). To model potential CSM interaction signals similar to that of SN 2015cp, we add a narrow $H\alpha$ line with a Gaussian profile to the SN 2011fe model. Due to the rareness of interaction in otherwise normal SNe Ia, we do not have good constraints on the diversity of interaction signatures and simulate a broad parameter space. The interaction was chosen to start at 100, 200, 300, or 500 days after the peak, last for 100, 300, or 500 days, and have a similar brightness to the observed signal in SN 2015cp ([Graham et al., 2019b](#)), as well as 10 times weaker or 10 times stronger than it. All possible combinations of these values are used, and a simulation without any interaction is also used as a control test, giving a total of 37 simulations.

Figure 3.2 shows an example of our model spectra at 300 d and SN 2015cp at 694 d in the rest frame ([Graham et al., 2019b](#)). It also shows the model redshifted to $z = 0.07$,

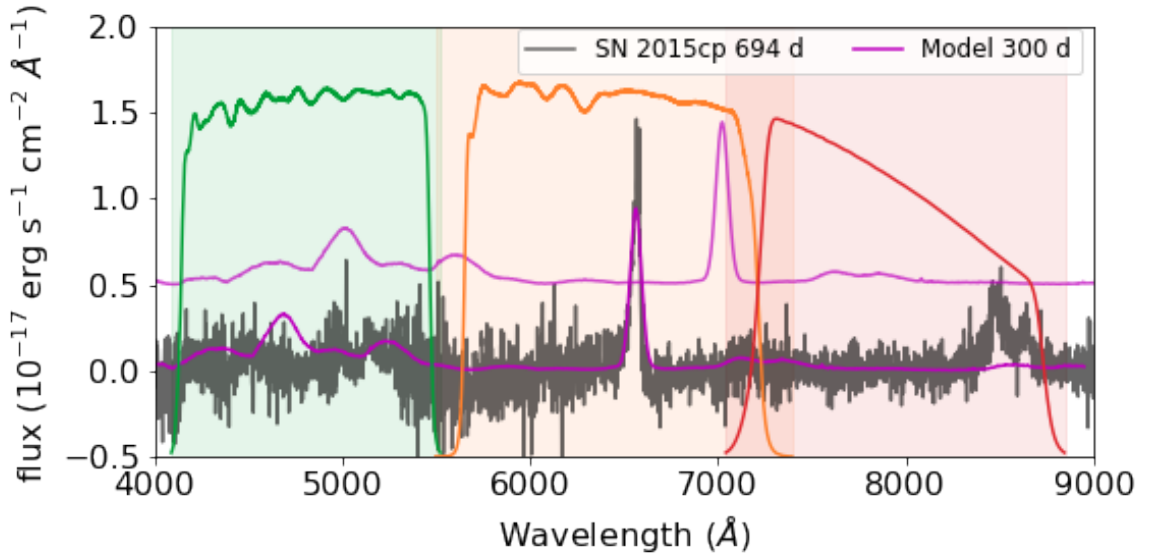


Figure 3.2: Model spectrum at 300 days (SN 2011fe with the added $H\alpha$ line) is shown in magenta overlaid on a rest-frame spectrum of SN 2015cp at 694 days in grey. The model flux has been scaled to the distance of SN 2015cp for comparison. The green, orange, and red shaded regions are the bandwidths of the g -, r -, and i -bands, respectively. The transmission profiles are plotted in the same colours for each band. The model is also shown shifted to $z = 0.07$ (and offset up in flux), where the $H\alpha$ line has just started to be in the i -band.

where the $H\alpha$ line is partly shifted into the i -band. Figure 3.3 shows the absolute magnitude ri -band light curves of the SN 2011fe model in the rest frame, as well as light curves with different strengths of $H\alpha$ emission. Our interaction model will only generate a late-time interaction signal in the r -band (or i -band at $z > 0.06$) as we only add a $H\alpha$ emission line. This is enough to test the binning programme but is likely too simple to reflect the actual late-time signal seen in SN 2015cp (which also showed O I and Ca II in the restframe i -band) or potential other events.

3.2.4.2 Simulating the observing campaign

By specifying the object to observe, as well as the telescope details and observation schedule, an observation campaign can be performed using SIMSURVEY resulting in a collection of observed light curves. For a deeper explanation of SIMSURVEY we refer the reader to Feindt et al. (2019b). The parameters used as input are listed in Appendix 3.7. In each SIMSURVEY run, 10^5 SNe Ia are simulated to produce observed light curves and meta-data such as redshift, observed peak date, etc. To ensure that the SNe Ia are similar around the peak to those recovered, we require that the SN Ia light curves must

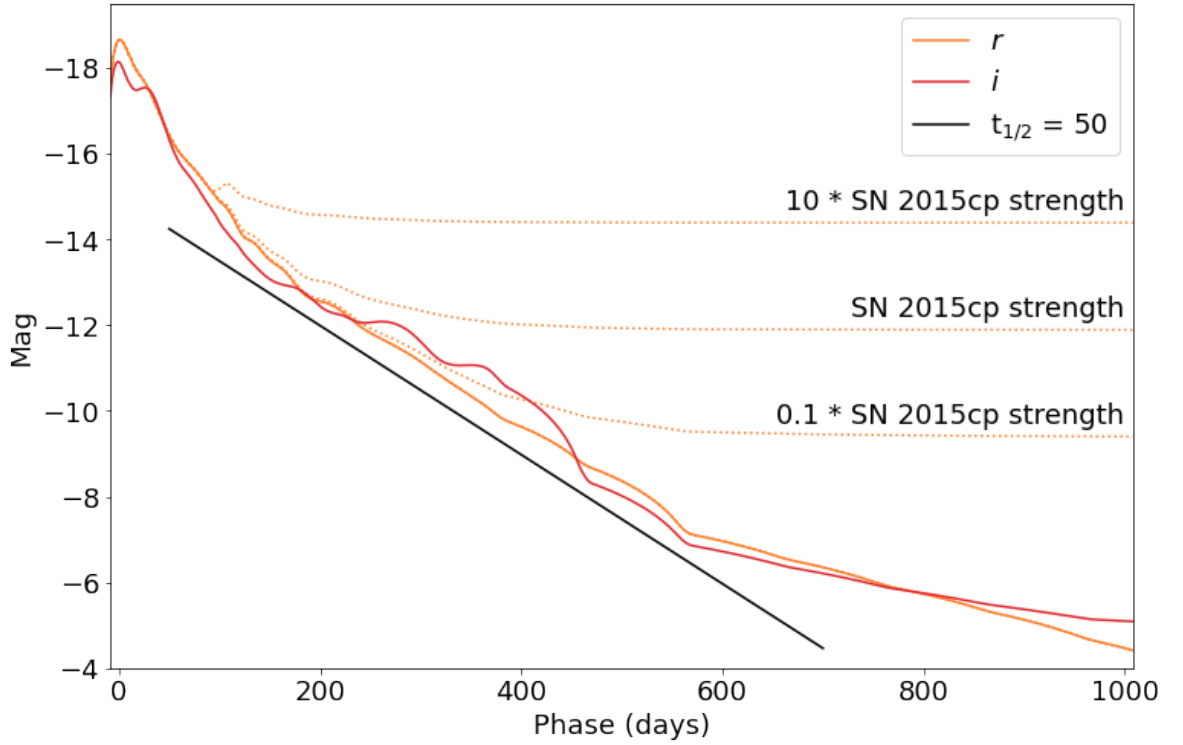


Figure 3.3: r (orange) and i (red) absolute magnitude light curves of the SN 2011fe model used in the simulations in the ZTF bands as a function of phase from rest-frame B -band peak (Mazzali et al., 2014). The bumpiness in the models is because the underlying SNCOSMO model class interpolates in flux space but fails to find an exponential decay. The added rest-frame CSM interaction model based on $H\alpha$ emission (starting at a phase of 100 d) is shown with dotted lines for the r -band. Once the interaction becomes the dominant source, it smooths out the bumps from the underlying tail. The black line shows a radioactive decay with $t_{1/2} = 50$ d, typical of a declining normal SN Ia tail.

have at least three detections of $\geq 5\sigma$ and are brighter than 19 magnitude at the peak. This reduces the sample to $\sim 40,000$ objects per simulation. These are sent through the binning and filtering programme (Section 3.2.1) as if they were real observed light curves to determine the recovery efficiency.

The volumetric rate used as input in the simulations favours more distant SNe, which results in very few SNe at extremely low redshift values and hence larger uncertainties. To mitigate this, we split $0 \leq z \leq 0.015$ into bins of size 0.001 and simulate an additional 100 SNe in each bin using the same parameters as in the original simulations. Introducing these additional events does not impact the recovery efficiencies because we are comparing the number of recovered events relative to the input number in each redshift bin and therefore, are insensitive to the input rate of events.

3.2.4.3 Simulated interaction recovery

Our aim is to determine from our simulations how many SNe Ia with signatures of late-time interaction similar to that of SN 2015cp would have been detected by our pipeline. For each of the simulations, we binned the SNe based on their redshift and looked at the fraction of SNe that were reported by the pipeline to show late-time excesses. Figure 3.4 shows the recovery fractions as a function of redshift for an example simulation when the interaction starts at 500 d and lasts for 500 d for simulations of no CSM interaction, late-time interaction with the same strength as SN 2015cp, and interaction 10 times as strong as SN 2015cp (strong interaction). As expected the recovery fraction drops off with increasing redshift for both the SN 2015cp equivalent strength and the interaction that is 10 times stronger, with the strong interaction recoverable out to a higher redshift.

The recovery fraction of the simulations with CSM interaction does not reach 100 per cent in the lowest redshift bins. This is because the radioactive tails of these SNe Ia tend to be bright out to hundreds of days after explosion. Therefore, depending on the cadence and uncertainties of the simulated photometry, the SN light can dominate over the CSM interaction and the CSM interaction signal does not alter the shape of

the SN decay tail enough to be flagged as CSM interaction.

In the simulation without CSM interaction, the recovery fraction is non-zero at small redshifts, meaning that some objects are falsely identified as having late-time excess. For these very bright and high signal-to-noise SN Ia light curves, our decaying tail model for normal SNe Ia proves to be too simple. Our analysis pipeline detects real deviations of the SN light curve evolution from our simple decay tail model. This only occurs at the lowest redshifts and nearby SNe Ia are rare, with only 0.6% of our observed SN Ia sample at $z \leq 0.01$. This means that contamination of our sample due to normal SNe Ia tails that cannot be fit by our simplified tail fit model is very low.

We fitted a sigmoid function to the recovery fractions of each simulation, using the total amount of objects in each bin as its weight (Fig. 3.4). A sigmoid function is an oversimplification (the recovery fraction is underestimated at the low redshifts) but it allows us to easily estimate the redshift limit where CSM interaction can be recovered. We define our redshift limit where CSM interaction can be recovered as z_{50} , the redshift where 50 per cent of the SN interactions are recovered. These values are listed for all simulations in Table 3.8.

As discussed in Section 3.2.4.1, we simulated 36 models with interaction signatures starting at 100, 200, 300 and 500 d post peak, lasting for 100, 300 and 500 d, and with strengths the same as SN 2015cp, 10 times weaker and 10 times stronger. We also simulated a model without any late-time CSM interaction. For the models with an interaction strength similar to SN 2015cp (Graham et al., 2019b), when the interaction is short and early (starting 100 days after the peak and lasting for 100 days), the interaction cannot be distinguished from a normal SN Ia decaying light curve and the recovery fraction is as low as the no interaction simulation. When the interaction is longer, or if it starts later, the light curve flattens enough to be identified as deviating from a normally declining SN Ia tail. This pushes the redshift boundary where 50 per cent of the interaction would be recovered by ZTF to $z_{50} = 0.0105 \pm 0.0003$ for the longest and latest interaction (500 - 1000 days after peak).

If the CSM interaction is 10 times weaker than that of SN 2015cp, the decaying

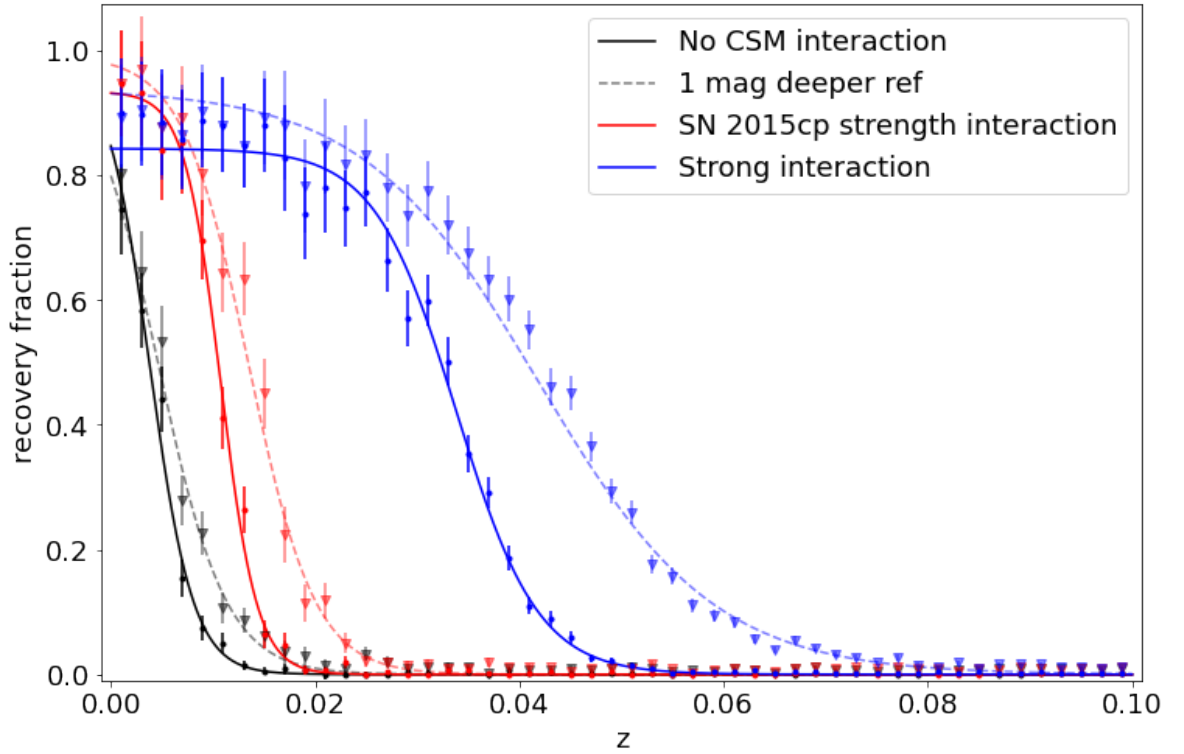


Figure 3.4: Fraction of SNe Ia for one of our simulations (interaction occurring between 500 – 1000 d after the peak) where the CSM interaction was recovered per redshift bin of size 0.002. The simulations are shown for interaction strengths of zero (grey), similar to SN 2015cp (red), and 10 times stronger than SN 2015cp (blue). In the simulation without CSM interaction, the recovery fraction should be interpreted as the fraction of false positives. The simulations with normal ZTF quality reference images are shown with dots and fitted sigmoid functions with solid lines. Simulations where one magnitude deeper reference images were assumed are shown in triangles, with their fitted sigmoid functions in dashed lines.

SN Ia tail generally dominates over the interaction signature and the light curve shows little deviation from a normal decaying SN Ia tail. Even in the best case scenario of the longest and latest CSM interaction simulation, the 50 per cent recovery threshold lies at $z_{50} = 0.0050 \pm 0.0005$. In the simulations where the interaction is 10 times stronger compared than that of SN 2015cp, the shortest and earliest interaction (lasting from 100 to 200 days after peak) has $z_{50} = 0.0091 \pm 0.0014$. For the longest and latest interaction, the 50 per cent recovery rate is at $z_{50} = 0.0323 \pm 0.0004$.

3.2.4.4 Impact of reference image depth

The mean limiting magnitude of the ZTF reference images is ~ 21.8 mag and as discussed in (Strotjohann et al., 2021), this is the limiting factor for recovering faint signals from binned light curve data. To test the improvement of deeper reference images, the assumed limiting magnitude was changed to be 0.5 and 1 mag deeper. The recovery fraction for one magnitude deeper is shown for comparison in Fig. 3.4. As expected, deeper reference images allows the interaction signatures to be detected to higher redshift, although the increases in z_{50} values are modest (see Table 3.8). For example, for the latest onset and longest interaction duration interaction, z_{50} increases from 0.0323 ± 0.0004 to 0.0407 ± 0.0009 .

3.3 Results

We run our custom detection pipeline on the ZTF DR2 light curves in the same way as it was performed on the simulated light curves in Section 3.2.4. In 1932 light curves, nothing is detected in any of the 16 trials discussed in Section 3.2.1, in 432 light curves the late-time detections are attributed to declining SN Ia tails, and in 1020 light curves the detections were not considered robust (<4 successful trials). These are the three largest cuts in our sample, as can be seen in Table 3.1, and leave us with 134 light curves that pass the pipeline. In Section 3.3.1, we describe the light curves of these events and discuss how some light curves fit into known classes of events (e.g. known

Ia-CSM, late-time SN Ia tail detections). In Section 3.3.2, we describe the additional tests that were performed on the remaining promising 10 events to determine if their late-time excesses are due to CSM interaction or other scenarios.

3.3.1 Initial summary of detected events

As can be seen in Table 3.1, the result of the pipeline is a list of 134 objects that require visual inspection after passing the detection cuts of positive $>5\sigma$ detections in adjacent light curve bins in at least four of the 16 bin size and placement combinations. In 47 of these cases, by visual inspection we identify that an incorrect baseline caused false positives. In five cases, the peak date estimation failed and estimated the peak to be over 100 days before the actual SN explosion. Because of this the SN itself was detected as a late-time signal. Furthermore, in 29 cases there was evidence of the host galaxy being improperly subtracted or showing signs of activity, which interfered with the forced photometry at the SN location. Finally, in 20 cases the tail fit test was unable to show the nature of the tails due to various reasons (e.g. the fits did not converge properly or there was a gap in the observations while the tail was visible). After this step, 33 objects were remaining in the sample.

Further details of these remaining 33 SNe Ia are shown in Table 3.2 and can be split up into four main groups: i) known Ia-CSM events, ii) transient siblings, where a second transient event occurs near the identified SN Ia causing its light to (partially) be picked up during forced photometry at the first SN location, iii) nearby objects whose tail could not be fitted by our simple model, and iv) objects that do not fall in the first three groups. In the following sections, we describe the first three of these groups that are not due to potential CSM interaction at late times.

3.3.1.1 Known Ia-CSM

The first group are the 13 known Ia-CSM, defined as those objects that already had a Ia-CSM classification. These objects started interacting relatively soon after the explosion and remained active long enough to be picked up by our pipeline beyond the

Table 3.2: List of objects that passed the initial visual inspections.

Name	IAU name	Redshift	Type ^(a)	Peak MJD	Peak mag.	Excess phase (d)	Excess band	Excess mag.	Group ^(b)
ZTF18aaykji	SN 2018crl	0.09690 ± 0.00002	Ia-CSM	58297.3	18.40 ± 0.04	100 – 400	<i>r</i>	20.1 – 21.9	Known Ia-CSM
ZTF18abuatfp	SN 2018gkx	0.13643 ± 0.00001	Ia-CSM	58382.1	18.71 ± 0.05	100 – 475	<i>gri</i>	19.6 – 21.5	Known Ia-CSM
ZTF18actuhrs	SN 2018evt	0.02442 ± 0.00001	Ia-CSM	58476.5	16.19 ± 0.01	100 – 525	<i>gri</i>	16.6 – 21.8	Known Ia-CSM
ZTF19aaoeqst	SN 2019agi	0.05958 ± 0.00001	Ia-CSM	58511.5	18.46 ± 0.04	100 – 450	<i>gri</i>	19.2 – 21.9	Known Ia-CSM
ZTF19abidbqp	SN 2019ibk	0.04014 ± 0.00001	Ia-CSM	58688.5	18.56 ± 0.05	100 – 1125	<i>gr</i>	19.1 – 21.5	Known Ia-CSM
ZTF19acbjddp	SN 2019rvb	0.1832 ± 0.0004	Ia-CSM	58790.1	18.90 ± 0.06	100 – 400	<i>gr</i>	20.4 – 22.0	Known Ia-CSM
ZTF20aatxryt	SN 2020eyj	0.0294 ± 0.0004	Ia-CSM	58939.2	17.24 ± 0.01	100 – 450	<i>gr</i>	19.0 – 21.8	Known Ia-CSM
ZTF20abbbsfs	SN 2020kre	0.13530 ± 0.00001	Ia-CSM	58998.2	19.09 ± 0.04	175 – 425	<i>gr</i>	19.8 – 21.4	Known Ia-CSM
ZTF20abmlrxr	SN 2020onv	0.0940 ± 0.0004	Ia-CSM	59052.4	17.85 ± 0.01	100 – 500	<i>gr</i>	18.8 – 21.6	Known Ia-CSM
ZTF20abqkbf	SN 2020qzz	0.0968 ± 0.0004	Ia-CSM	59094.3	18.18 ± 0.04	100 – 450	<i>gri</i>	19.5 – 21.9	Known Ia-CSM
ZTF20accmutv	SN 2020uem	0.043 ± 0.001	Ia-CSM	59173.5	16.38 ± 0.01	100 – 525	<i>gr</i>	17.4 – 21.4	Known Ia-CSM
ZTF20aciwcuz	SN 2020xtg	0.06122 ± 0.00001	Ia-CSM	59189.5	17.45 ± 0.02	100 – 500	<i>gri</i>	18.0 – 21.9	Known Ia-CSM
ZTF20acyroke	SN 2020aeh	0.12665 ± 0.00004	Ia-CSM	59217.4	19.01 ± 0.06	100 – 250	<i>r</i>	19.8 – 20.9	Known Ia-CSM
ZTF18aasdted	SN 2018big	0.01814 ± 0.00001	Ia-norm	58268.4	15.64 ± 0.01	450 – 550	<i>gr</i>	20.4 – 21.5	Sibling
ZTF19aaysiwt	SN 2019hnt	0.0926 ± 0.0004	Ia	58651.2	18.46 ± 0.05	525 – 625	<i>gr</i>	20.5 – 21.7	Sibling
ZTF19acihfxz	SN 2019tjz	0.055 ± 0.003	Ia-norm	58795.1	18.00 ± 0.03	950 – 1050	<i>r</i>	19.4 – 20.7	Sibling
ZTF20abzetdf	SN 2020tft	0.071 ± 0.002	Ia-norm	59113.5	18.2 ± 0.1	725 – 800	<i>r</i>	19.4 – 20.2	Sibling
ZTF20acehyxd	SN 2020uud	0.0346 ± 0.0005	Ia-norm	59129.3	18.72 ± 0.03	300 – 350	<i>r</i>	20.2 – 21.5	Sibling
ZTF19aatlmbo	SN 2019ein	0.0072 ± 0.0001	Ia-norm	58617.2	blinded ^(c)	100 – 425	<i>r</i>	18.9 – 21.8	Kinked tail
ZTF20abqvsik	SN 2020rcq	0.00246 ± 0.00001	Ia-norm	59144.5	blinded ^(c)	100 – 400	<i>i</i>	16.5 – 22.2	Kinked tail
ZTF20abrjmgi	SN 2020qxp	0.00356 ± 0.00001	Ia-91bg	59088.1	blinded ^(c)	100 – 375	<i>r</i>	17.9 – 21.8	Kinked tail
ZTF20abwrcnq	SN 2020sck	0.01643 ± 0.00001	Iax	59099.4	16.25 ± 0.01	100 – 450	<i>gri</i>	19.1 – 21.9	Kinked tail
ZTF20achlced	SN 2020uxz	0.00867 ± 0.00008	Ia-norm	59142.4	blinded ^(c)	100 – 400	<i>gr</i>	17.1 – 21.9	Kinked tail
ZTF19acvrqtv	SN 2019vzf	0.059 ± 0.004	Ia-99aa	58829.1	18.00 ± 0.07	150 – 400	<i>gr</i>	20.7 – 21.8	Other – AGN ^(d)
ZTF20aahptds	SN 2020awr	0.07649 ± 0.00002	Ia-norm	58888.5	18.54 ± 0.07	300 – 1050	<i>i</i>	20.2 – 20.5	Other – data issue ^(d)
ZTF20aazwuin	SN 2020kzd	0.082 ± 0.001	Ia-norm	58997.4	18.86 ± 0.03	250 – 850	<i>gr</i>	21.3 – 22.0	Other – data issue ^(d)
ZTF18abtqevs*	SN 2018grt	0.042 ± 0.003	Ia-norm	58372.3	18.56 ± 0.02	1350 – 1450	<i>r</i>	21.1 – 21.3	Other
ZTF19aanyuyh	SN 2020pkj	0.02456 ± 0.00001	Ia-norm	59060.4	16.90 ± 0.01	100 – 175	<i>r</i>	20.8 – 21.1	Other
ZTF19abfvhlx*	SN 2019ldf	0.05646 ± 0.00001	Ia-norm	58686.5	17.90 ± 0.04	1050 – 1225	<i>ri</i>	20.1 – 21.1	Other
ZTF19ablekwo	SN 2019mse	0.088 ± 0.004	Ia-norm	58715.4	18.37 ± 0.02	450 – 700	<i>gri</i>	19.8 – 20.6	Other
ZTF19abzwtiu	SN 2019rqn	0.075 ± 0.003	Ia-norm	58760.3	18.62 ± 0.03	950 – 1050	<i>i</i>	20.6 – 21.4	Other
ZTF20aaiifyfx	SN 2020alm	0.06001 ± 0.00001	Ia-norm	58873.5	18.10 ± 0.02	750 – 1025	<i>gri</i>	19.9 – 21.9	Other
ZTF20abjfufv*	SN 2020tfc	0.031 ± 0.001	Ia-norm	59116.3	17.22 ± 0.01	550 – 800	<i>gri</i>	18.9 – 21.4	Other

*Our three final objects with suggested detections of late-time interaction.

^(a)Type is based on spectral classifications (Rigault et al., in prep.), Ia-CSM are those interacting with CSM that is observed around peak, Ia-norm are those that are most consistent with a normal SN Ia, Ia are those without a sub-classification but are consistent with being a SN Ia, and SN 2020sck is a Iax (Dutta et al., 2022).

^(b)The objects are split into four groups: Ia-CSM that were previously known, identified siblings, SNe Ia that are detected due to their early-time tail fits showing a kink (Kinked tail), and the ‘Other’ category that includes ten events with potential flux excesses, including three (SN 2019vzf, SN 2020awr and SN 2020kzd) that are subsequently ruled out (see Section 3.3.2).

^(c)The peak magnitudes of four SNe Ia in the sample are blinded because of their planned use in H_0 constraints (Rigault et al., in prep.).

^(d)SN 2019vzf is ruled out as a true excess due to AGN variability at the position, in SN 2020awr the excess is only detected in the *i* band and is ruled out by the scene modelling analysis, and SN 2020kzd is detected in the *gr* bands on a complex galaxy environment and not detected in the scene modelling analysis (see Section 3.3.2.1).

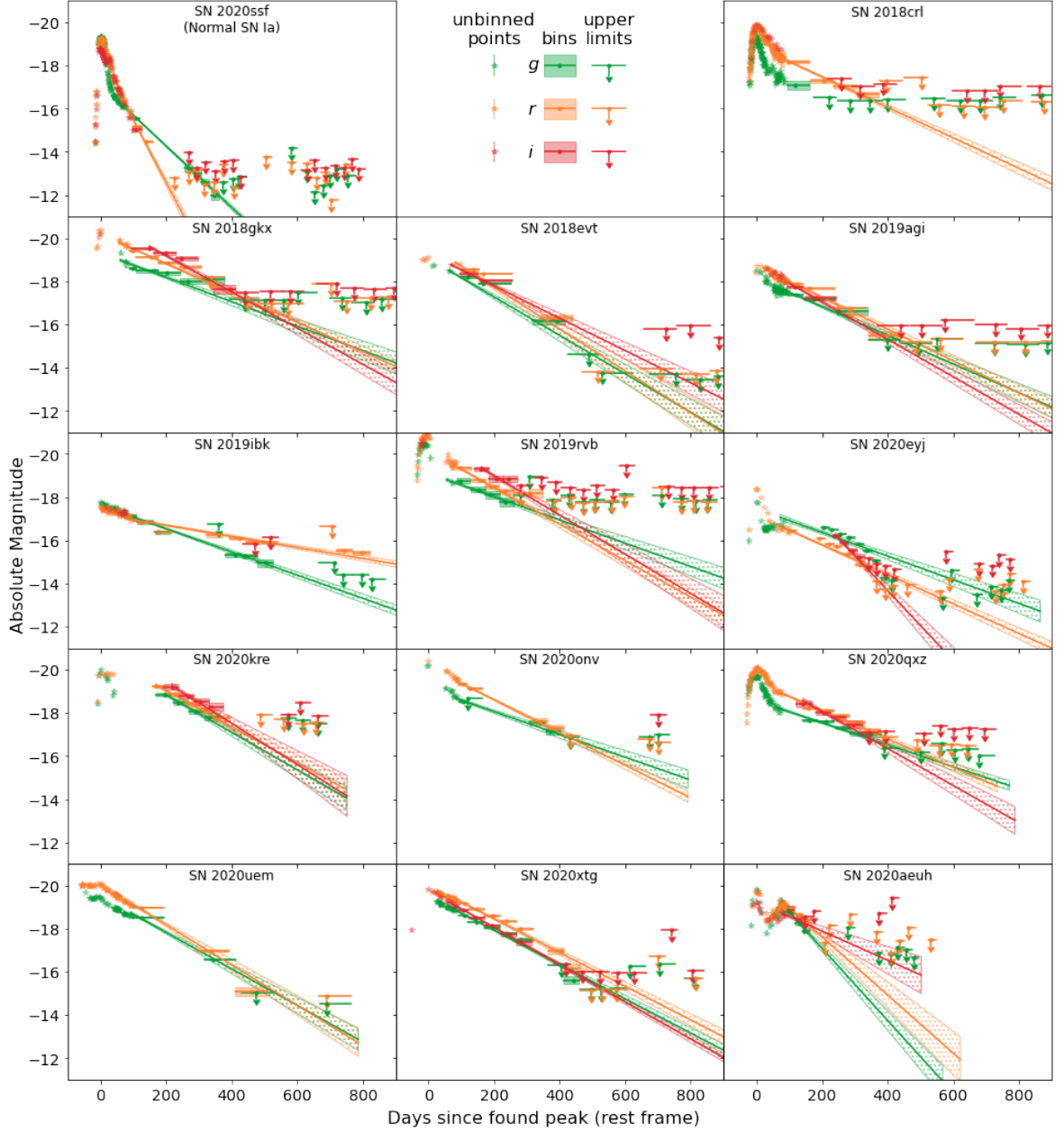


Figure 3.5: Binned late-time observations of the recovered known SNe Ia-CSM. All objects are shown in absolute magnitude and over the same time range for easy comparison. All objects are detected beyond 100 days after the peak without using the binning technique. We do not show these individual data points to increase readability. The tail fits are shown as solid lines with the hashed region denoting their 1σ uncertainties. For comparison, SN 2020ssf (ZTF20abytpc) in the top left corner is a normal SN Ia with a normally declining tail with $t_{1/2,g} = 53 \pm 1$ days and $t_{1/2,r} = 26 \pm 1$ days. The fitted tails for the SNe Ia-CSM are significantly shallower.

100 day threshold. Figure 3.5 shows the light curves of the recovered SNe Ia-CSM in absolute magnitude space (uncorrected for extinction). Even if the peak identified by our code is not the real peak due to it not being observed (e.g. for SN 2018evt, SN 2019agi, and SN 2019ibk), the CSM interaction persists for long enough for it to be picked up by our pipeline.

Ten of the known Ia-CSM SNe are presented in Sharma et al. (2023), who search for SNe Ia-CSM discovered in the ZTF Bright Transient Survey from May 2018 to May 2021 (BTS; Fremling et al., 2020; Perley et al., 2020). They find two objects that are not in our sample: SN 2020abfe (ZTF20acqikeh) and SN 2020aekp (ZTF21aaabwzx). SN 2020abfe is in the DR2 sample, but due to a combination of a gap in the observed light curve and the interaction not altering the declining tail sufficiently, our tail fit procedure is unable to distinguish it from a normal declining SN Ia tail. SN 2020aekp was first detected after the final date for objects to be included into our sample. Two of the events in our sample (SN 2020eyj and SN 2020kre) are not presented in Sharma et al. (2023). SN 2020eyj was excluded as Sharma et al. (2023) focussed on interaction with H-rich material and this object showed He emission lines suggesting interaction with He-rich material (Kool et al., 2023). SN 2020kre is not in the BTS sample and therefore, not included in Sharma et al. (2023). However, it was confirmed with spectroscopy to have $H\alpha$ emission in its peak spectra.

Out of the 13 events SN 2020aeuh is an outlier, due to its distinct light curve. While the other 12 known Ia-CSM events detected in our sample have decline tails whose slopes are significantly shallower than for a normal SN Ia or steepen over time, SN 2020aeuh brightens significantly, having a double peaked nature with the second peak at around 100 d after the first. Even though the light curve suggests the SN to be interacting, no H emission ($H\alpha$ or other lines) are observed. Kool et al. (in prep) present a detailed analysis of this object.

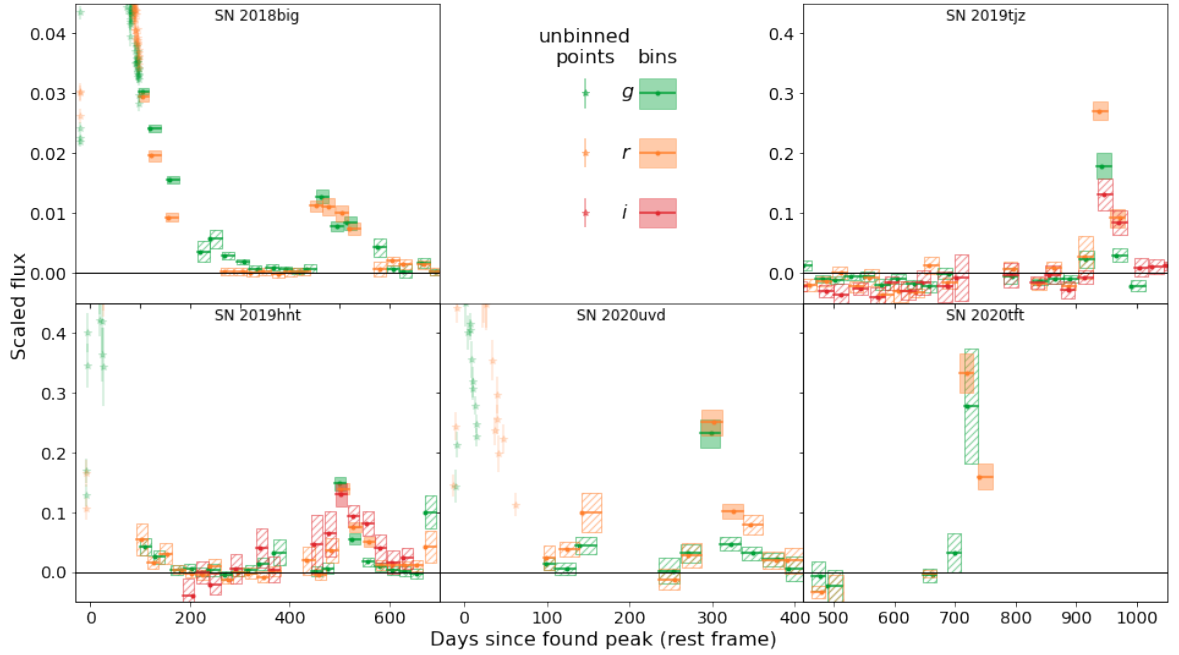


Figure 3.6: Binned late-time observations in flux space of the five events with a detected sibling, with the flux normalised to the found peak flux. All objects are plotted on the same flux scale for easy comparison except for SN 2018big, as its late-time detections are much weaker compared to the original SN peak magnitude due to the larger distance offset between the siblings.

Table 3.3: Objects with a detected sibling transient.

Primary name	IAU name	Sibling name	IAU name ^b	Type	Date ^a	Offset (") ^c
ZTF18aasdted	SN 2018big	ZTF19abqhobb	SN 2019nvm	IIP	58 714	3.7
ZTF19aaysiwt	SN 2019hnt	ZTF20acwpads	-	-	59 186	1.2
ZTF19acihfxz	SN 2019tjz	ZTF18aanhpil	-	-	59 774	1.2
ZTF20abzetdf	SN 2020tft	-	-	Ia	59 867	< 1
ZTF20acehyxd	SN 2020uvd	ZTF21abouuow	SN 2021udv	Ia	59 422	3.1

^aMJD of the first detection of the sibling.

^bThe siblings ZTF19aaysiwt and ZTF20acwpads share an IAU name. For ZTF20abzetdf, the siblings are too close together (<1" separation) to be automatically recognised as separate events, causing them to share both ZTF and IAU names. ZTF18aanhpil is a sibling transient in 2022 on top of the host nucleus, resulting in the internal name being from 2018.

^cAngular separation on the sky between the siblings.

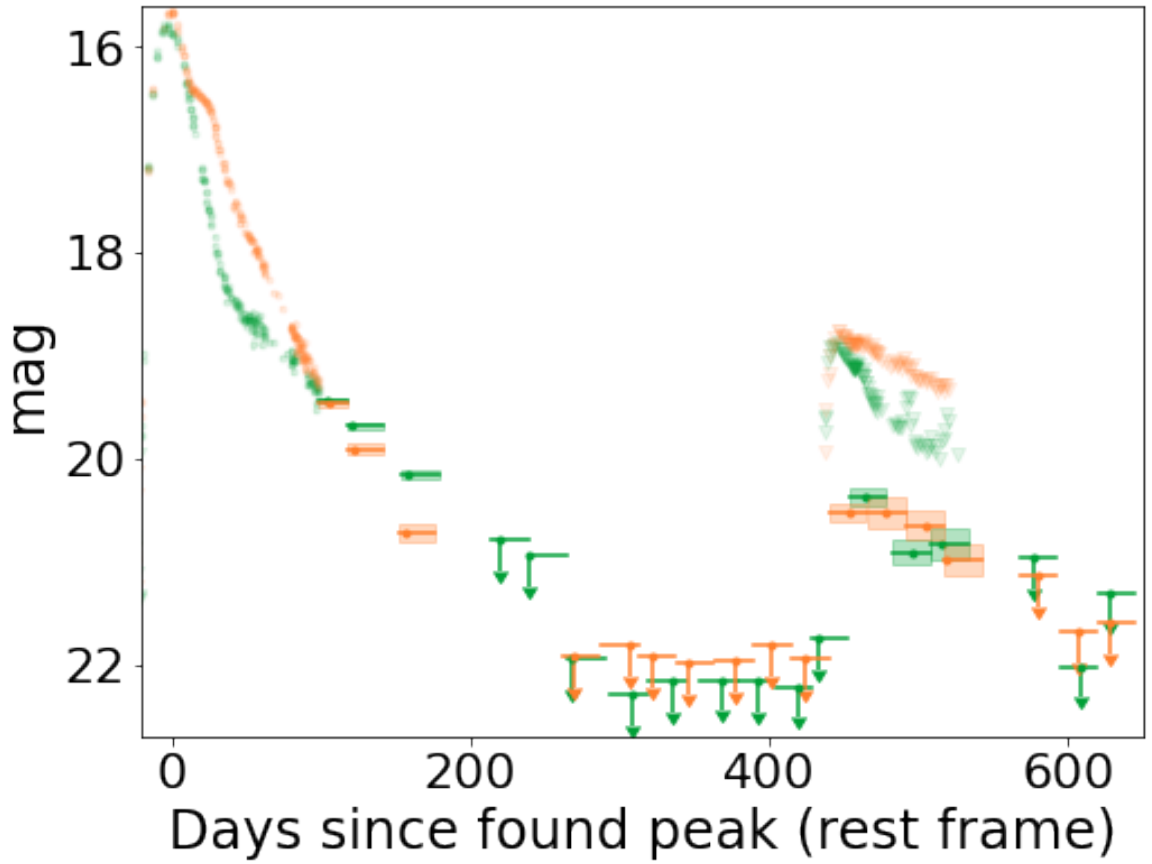


Figure 3.7: Light curves of SN 2018big and its sibling SN 2019nvm in magnitude space using bins of 25 d. The g (green) and r (orange) bins follow the tail of SN 2018big until it disappears in the noise. About 450 d after the peak of SN 2018big, new detections are identified in the binned photometry. The individual observations remain upper limits, although their shape hint to the true nature of these late-time detections.

3.3.1.2 Siblings

Siblings are transients that occur in the same host galaxy as each other and can be useful for understanding differences in local environments (e.g. [Biswas et al., 2022](#); [Graham et al., 2022](#)). In some cases, the siblings occur in (almost) the same place on the sky, only differing in explosion time. This can be either due to the two transients being physically close together, or a projection effect due to the inclination of the host. However, the result is the same: forced photometry at the location of one sibling will result in a (partial) recovery of the other. Assuming that the first transient is a SN Ia in our sample and the second transient is fainter, our pipeline will flag the late-time rebrightening as a late-time excess in one of our objects.

Careful examination of the images using SNAP and cross-referencing using Fritz (an alert broker, [van der Walt et al. 2019](#); [Duev et al. 2019](#); [Kasliwal et al. 2019](#); [Coughlin et al. 2023](#)) and the Transient Name Server¹ (TNS) showed that there are five objects in our shortlist whose late-time detections are due to a sibling. Figure 3.6 shows the binned light curves of these objects in flux space. In each light curve there is a sudden significant spike in the detected fluxes in all observed bands, which falls back down again after a short period of time. Table 3.3 lists the name and type of each sibling if known, as well as their sky separation. In some cases the siblings are close enough together that they are not automatically recognised as separate events, resulting in them having the same name. In the case of SN 2019tzj the sibling (ZTF18aanhpjii) exploded close to the nucleus, which had some spurious detections in 2018. This caused the sibling to have a 2018 ZTF name, although it exploded in 2022.

Figure 3.7 shows the detection of a sibling (SN 2019nvm) in the late-time light curve of SN 2018big in magnitude space. SN 2019nvm is slightly offset ($\sim 4''$) from the location of the original SN. The photometry pipeline forces the point spread function (PSF) fit at the position of SN 2018big. As the position of SN 2019nvm is slightly offset, only some of the total flux of SN 2019nvm is captured in the fit. Besides these five siblings, we identified two other pairs of siblings with SNAP: SN 2019gcm and

¹<https://www.wis-tns.org/>

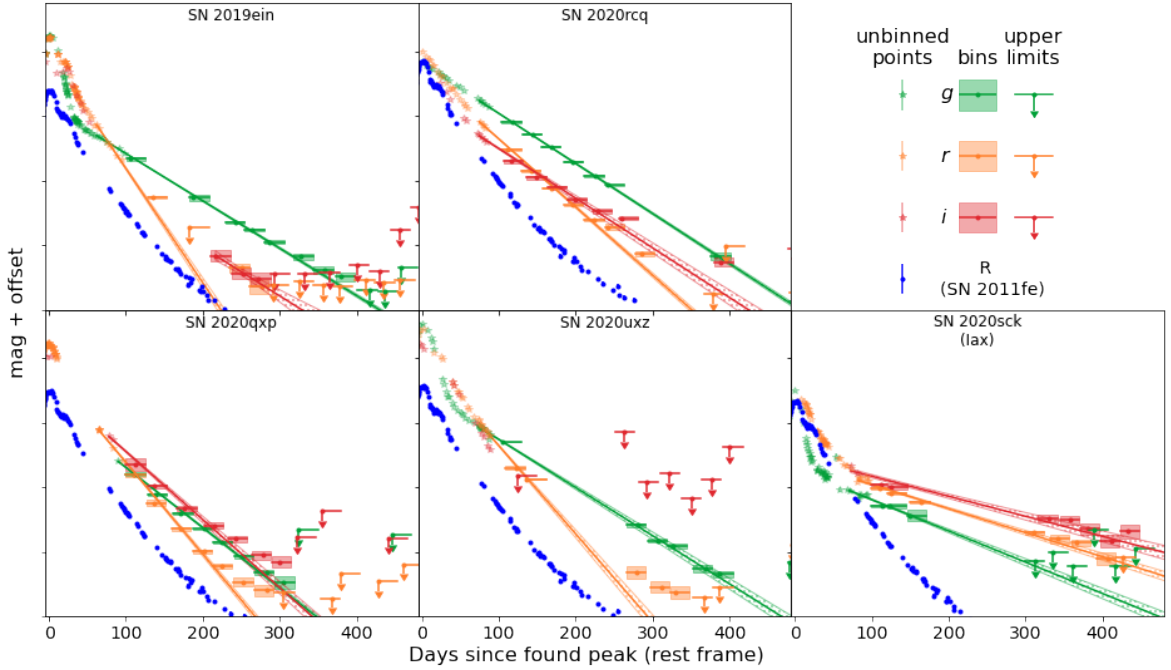


Figure 3.8: Five objects with kinks in their tails that start to deviate from the assumed decline rate at $\sim 200 - 250$ d post peak are shown in magnitude space as a function of days since peak. As most of these objects have their peak magnitude blinded, no scaling is shown. A normal radioactive decay model was fitted to these tails, shown as solid straight lines with their 1σ uncertainty as dashed regions. But as the ejecta opacity changes over time so does the half-life time of the tail, causing a kink seen in the bins which is not reproduced by the model. The arbitrarily normalised R -band light curve of SN 2011fe (known not to have CSM interaction from detailed spectral studies) (Zhang et al., 2016) is shown in blue, showing the same shift in decline slope at a similar phase.

SN 2021fnj, and SN 2020jgs and SN 2021och. These siblings were too far apart to be picked up with the forced photometry (9.6 and 10.8", respectively) but were found while inspecting using SNAP. For a complete list and study on the siblings found in the ZTF DR2, we refer the reader to Dhawan et al. (in prep.).

3.3.1.3 Kinked tails

This group consists of five objects where the simple tail model, based on the typical decline rate of SNe Ia based on SN 2011fe (Dimitriadis et al., 2017), failed to fit the observations at later times. The reason for this failure in four of the events is that there is a slow-down in the r - and i -band decline rates at $\sim 200 - 250$ d after peak, which the model does not take into account. The fifth event, SN 2020sck (Dutta et al., 2022), is a known SN Iax, a subclass known for having lower ejecta velocities and luminosities, suggesting that the explosion did not necessarily fully disrupt the star (Jordan et al.,

2012; Kromer et al., 2013). This event was flagged because of a slow-down in its decline rate roughly 80 days after the identified peak. The change in slope is visible in all bands and significantly longer than the assumed $t_{1/2} = 50$ d of normal SNe Ia. The presence of a bound remnant has been suggested to be the cause of similar late-time signatures seen in other SNe Iax (Kawabata et al., 2018; McCully et al., 2022; Camacho-Neves et al., 2023).

The four SNe objects that deviate from the simple tail model are very nearby ($z \leq 0.009$) compared to the majority of ZTF DR2 sample and when using the binned observations they are bright enough to be detected up to (nearly) a year after their first detection. As Rigault et al. (in prep.) are using these nearby events to calibrate their H_0 measurement, their peak magnitudes are currently blinded. Figure 3.8 shows the g -, r -, and i -band light curves of these objects in magnitude space. The R -band light curve of SN 2011fe (Zhang et al., 2016), which had a similar change in decline slope, is also shown for comparison. As discussed in Dimitriadis et al. (2017), the radioactive decays produce γ -rays and positrons, as well as X-rays and electrons that can be thermalised, depositing their energy in the expanding SN ejecta. As the ejecta expand over time they become more transparent, shortening the delay between thermalisation of the deposited energy and the emission of optical radiation. This results in the SN tail slope changing as the opacity changes.

To be able to observe a change in decline slope such as this, a SN has to be both bright and well observed during the time it is visible. The other SNe Ia in our sample at similarly low redshifts have gaps in their observations or the change in slope is not strong enough for the tail fits to fall outside the allowed range of reduced chi-squared values ($\chi^2_{\text{red}} > 5$) and therefore, are not flagged by the pipeline due to this.

3.3.2 Additional tests of promising events

After performing the tests discussed in the previous sections on each event, there are ten objects remaining with an unexplained late-time excess. Light echoes produced by SN light scattering off of nearby dust clouds were considered, but were ruled out

Table 3.4: Results of the additional tests for the ten promising objects. The host separation is given in " and converted to kpc using the redshift given in Table 3.2 and the same cosmology as was used in Sec. 3.2.4.4. In the final five columns the similarity of each SN Ia with a late-time excess is compared to different transient classes to see if the late-time signal can be interpreted as another transient. This can be excluded based on an inconsistent colour (1), duration (2), and/or an excessive amount of host extinction (3) needed to obtain the observed magnitudes.

Name	Red. error ^(a)	Host separation (") (kpc)		$E(B - V)_{\text{host}}$ (mag.) ^(b)	AGN ^(c)	Approx. mag. ^(d)	SN Ia?	Ib?	Ic?	IIP?	TDE?
SN 2018grt*	no	0.36 ± 0.03	0.32 ± 0.02	$0.21 - 0.36$	no	-16.5	no (23)	no (23)	no (2)	no (3)	no (13)
SN 2020pkj	no	0.52 ± 0.02	0.28 ± 0.01	$0.23 - 0.36$	no	-15.4	yes	yes	yes	no (23)	no (13)
SN 2019ldf*	no	0.65 ± 0.04	0.78 ± 0.05	≤ 0.03	no	-16.4	no (123)	no (123)	no (123)	no (123)	no (13)
SN 2019mse	no	0.59 ± 0.05	1.09 ± 0.10	0	no	-17.5	no (2)	no (2)	no (2)	no (2)	yes
SN 2019rqn	no	1.39 ± 0.08	2.21 ± 0.13	≤ 0.04	no	-16.8	no (13)	yes	yes	no (1)	no (13)
SN 2019vzf	no	3.89 ± 0.08	4.86 ± 0.10	0	yes	-	-	-	-	-	-
SN 2020awr	yes	19.60 ± 0.04	31.65 ± 0.07	-	-	-	-	-	-	-	-
SN 2020alm	no	0.67 ± 0.07	0.85 ± 0.09	≤ 0.05	no	-16.9	no (123)	no (12)	no (23)	no (123)	yes
SN 2020kzd	yes	4.67 ± 0.04	8.07 ± 0.07	-	-	-	-	-	-	-	-
SN 2020tfc*	no	0.21 ± 0.02	0.14 ± 0.01	≤ 0.12	no	-16.8	no (123)	no (12)	no (23)	no (123)	no (3)

^(a)Reduction error: Comparison between the standard light curve reduction and scene modelling identified issues with the baseline correction (see Section 3.3.2.1).

^(b)Estimated assuming the main peak is a normal SN Ia. When correcting for Milky Way extinction and distance is enough to exceed an absolute g -band magnitude of -19.3 , we quote a host $E(B - V) = 0$ mag.

^(c)The presence of an AGN was estimated using the WISE colours of the host and the criteria of [Hviding et al. \(2022\)](#).

^(d)Mean absolute magnitude of the r -band late-time excess after correction for Galactic and host extinction, averaged over the host extinction range considered.

as these are typically ≥ 10 mag fainter than the SN at its peak ([Patat, 2005](#); [Graur et al., 2016](#)). We performed several additional tests on these ten events to try to determine the origin of their late-time excess. The first is using SMP as described in Section 3.1.1. The second is testing for coincidence with an AGN and third is more detailed comparisons with known transient classes. These tests are discussed below and a summary is shown in Table 3.4.

3.3.2.1 Scene modelling photometry

To test for issues in data processing, we ran the ten events through the scene modelling pipeline of Lacroix et al. (in prep.) as discussed in Section 3.1.1. Two SNe Ia (SN 2020awr and SN 2020kzd) were found to have issues with their difference imaging and forced photometry light curves, causing false detections. The detections in both these events are close to the detection limit and therefore, are impacted by even small errors in the baseline placement. The difference imaging (left panel) and scene-modelling

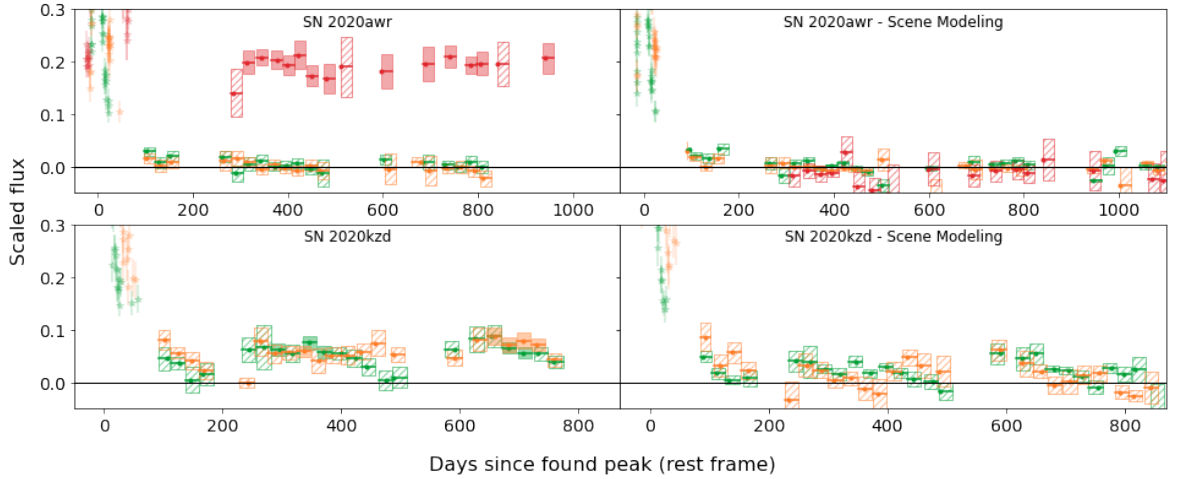


Figure 3.9: Two objects whose late-time detections were revealed to be caused by the photometry extraction. The colours are as in Fig. 3.8. The left side shows the binned forced photometry light curve, and the right side shows the binned SMP light curve. Bins with 5σ detections are shaded solid, while the non-detections are hashed.

(right panel) light curves of these two events are shown in Fig. 3.9.

For SN 2020awr, ~ 300 d after the SN peak, the *i*-band observations jump up to detections at ~ 20.3 mag. In contrast to other objects where baseline issues were found, here the offset occurs only for part of the light curve, while the pre-SN baseline has no visible issues. We could not identify a clear reason for this when inspecting the images with SNAP, and the SN is too far away from the host nucleus for it to be host activity. For the scene-modelling version of the photometry, the jump in the *i*-band observations has disappeared completely, showing that there was indeed an unidentified issue with the *i*-band data for this object. Since the late-time detections are determined to be spurious, this object is ruled out from having late-time detections.

In the case of SN 2020kzd, late-time detections are present in the *g*- and *r*-bands for hundreds of days (see Fig. 3.9). The SN is in a complex environment with three galaxies close to its sky position, which likely complicates the image subtraction and baseline correction. When SMP is performed on the event the detections disappear and average flux at late times is consistent with zero, showing that the binned forced photometry light curve likely suffered from a wrongly determined baseline correction.

Table 3.5: Details of the comparison transients used to test if late-time detections could be explained by another transient at a similar sky position. The first column shows the assumed type of transient, the second shows the transients used to represent each type, the third has the approximate absolute extinction-corrected r -band peak magnitudes, and the fourth the reference for each event.

Type	Name	Peak abs. M_r (mag.)	Reference
SN Ia	SN 2011fe	$-18.4 - -19.4$	Mazzali et al. (2014)
SN Ib	SN 2019yvr	-17.9	Kilpatrick et al. (2021)
SN Ic	SN 2021krf	-17.3	Ravi et al. (2023)
SN IIP	SN 2020jfo	-17.8	Ailawadhi et al. (2023)
SN IIP	SN 2017gmr	-18.7	Andrews et al. (2019)
TDE	AT 2018hco	-22.1	van Velzen et al. (2021)
TDE	AT 2018zr	-20.1	van Velzen et al. (2021)

3.3.2.2 AGN contamination

If a SN explosion site is coincident with a host galaxy that has an AGN, host activity is a likely cause of the late-time detections. Using data from the Wide-field Infrared Survey Explorer (WISE; [Wright et al. 2010](#)), [Hviding et al. \(2022\)](#) present a criterion to test if a galaxy hosts an AGN based on the WISE $W1-W2$ and $W2-W3$ colours, which we apply to our events. One object (SN 2019vzf) is 4.86 kpc of its host centre and its host is a known AGN, with WISE colours of $W1-W2 = 0.55 \pm 0.03$ and $W2-W3 = 2.90 \pm 0.04$ mag. In SNAP, the late-time signal appears to cover both the SN and AGN locations. The AGN contamination is too strong to put any meaningful constraints on the late-time flux at the SN location. We kept the object in our sample until now to test if it is possible to use scene modelling to reduce the AGN contamination. However, this is not possible. We attribute the late-time signal to host activity and disregard it in future discussion. The light curves of SN 2019vzf are shown in Fig. 3.10.

3.3.2.3 Presence of a sibling close to the SN location

To test if a previously unidentified sibling transient is causing the late-time detections of the remaining seven objects, we compared their late-time light curves to known classes of transients, including a SN Ia, core-collapse SNe (Type Ib, Type Ic, Type IIP) and two tidal disruption events (TDE). Firstly, we have estimated the amount of potential host extinction from the main SN peak by assuming it was a normal SN

Ia with a typical g -band peak of -18.8 to -19.3 mag after correcting for the distance to the SN and for Milky Way extinction. These estimated host extinction values are given in Table 3.4, assuming $R_V = 3.1$. The bright end of the absolute peak magnitude gives an upper limit for the host extinction, and the faint end gives a lower limit. After correcting for this range of additional host galaxy extinction, the late-time excesses have mean absolute r -band magnitudes of -15.4 to -17.5 mag (see Table 3.4).

After estimating the allowed extinction for each primary SN Ia, we initially assumed that if the late-time excess is due to another transient then it will have the same extinction along the line-of-sight. For these other transients, we used examples of a SN Ia, Ib, Ic, two IIPs, and two TDEs to compare against, with details of the comparison objects described in Table 3.5. The transients chosen to represent their category are all in the typical magnitude range for their type. Two TDEs and SN IIPs were chosen to represent the upper and lower end of the range of peak magnitudes expected for these transients. We use our model for SN 2011fe to represent SNe Ia and test the lower and upper edge of the range of normal SN Ia peak r -band magnitude.

These comparison objects were chosen as they have well-sampled light curves in the ZTF filters, and literature values for the host extinction. We correct the light curves of the comparison objects using their literature redshifts and their extinction values before correcting for the redshift and extinction of each SN Ia in our sample with a potential late-time excess. We then compare this transient light curve to the found late-time detections to see how well they match. A good match will have a similar magnitude, colour, and duration.

It could be the case that the suspected sibling was in the same line-of-sight direction, but had a different amount of extinction due to, for instance, exploding behind a cloud that adds additional extinction. We check this by adding enough extinction to match the r -band detections between the different comparison events and the observed late-time detection and again check if the colour and duration match up, as the observed colour is affected by the extinction. For the TDE comparisons, we allow a host galaxy $E(B - V)$ of up to one magnitude, as was estimated for the ZTF TDE sample of

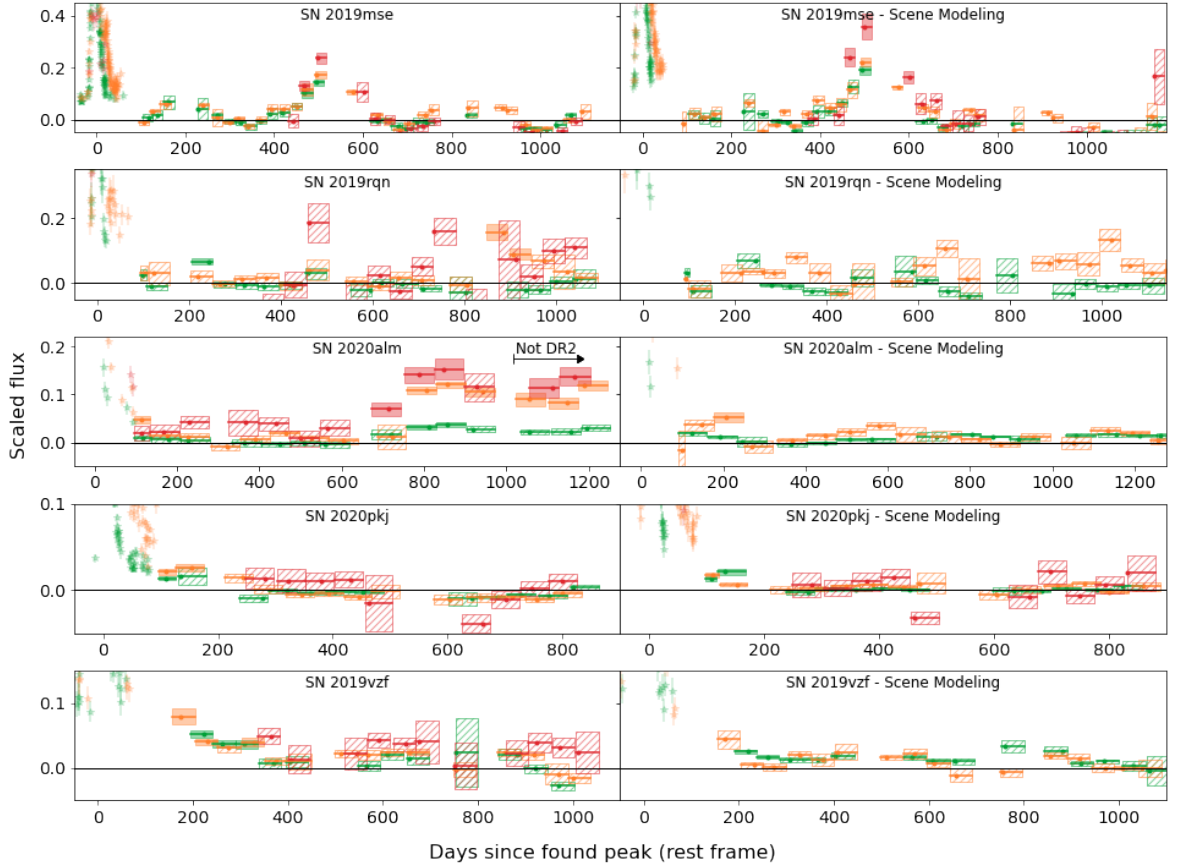


Figure 3.10: Objects whose late-time detections are explained in the additional tests. The top four rows show the light curves of the objects where a previously undetected sibling transient as an explanation for the late-time observations could not be ruled out, with forced photometry light curves in the left-hand panels and the scene modelling photometry light curves in the right-hand panels. The 5σ detections are shown as bins with solid uncertainty regions and bins with hashed uncertainty regions are non-detections. The object whose late-time detections are caused by the host galaxy AGN, SN 2019vzf, is shown in the bottom row. The colours are as in Fig. 3.8 with *g*band in green, *r*band in orange, and *i*band in red.

Hammerstein et al. (2023).

For four events (SN 2019mse, SN 2019rqn, SN 2020alm, and SN 2020pkj), the late-time detections are consistent with at least one of the comparison classes, as detailed in Table 3.4 and shown in Fig. 3.10. We describe them individually in the following sections. The three remaining events (SN 2018grt, SN 2019ldf, and SN 2020tfc) cannot be explained by the presence of a sibling transient and are discussed further in Section 3.3.2.4.

SN 2019mse

SN 2019mse has late-time detections starting at 450 d after the peak and lasting ~ 250 d in the *gri*-bands with an absolute *r*-band magnitude of -17.5 mag during the excess. Careful re-examination of the difference images show that the late detections are slightly offset (about one pixel) from the SN location, and appear to be on the host nucleus location instead. However, with its WISE colours being $W1 - W2 = 0.25 \pm 0.04$ and $W2 - W3 = 2.44 \pm 0.09$, the host is determined to not contain an AGN. The scene modelling version of the light curve shows a similar late-time excess, showing that this is not an artefact from the chosen photometric analysis method.

The late-time signal is detected in all three bands, and its behaviour is very similar in all of them (see Fig. 3.10). Its rise and decline time scales, absolute magnitude, and colours agrees well with the ranges seen for TDE. Together with the observation that the late-time detection are at the host nucleus location, this suggests that a nuclear transient explains the late-time signal adequately.

SN 2019rqn

In the case of SN 2019rqn, there is a short period of detections at 950 – 1050 d in the *r*-band after a gap in the observations, declining and fading below the detection significance within 100 d of the first detection. Nothing is detected at a $\geq 5\sigma$ level in the *g*- or *i*-band observations. The *i*-band SMP light curve had its host contribution not completely subtracted, causing a flux offset in the data points. We therefore do not consider the SMP *i*-band further. The data points in the *g*- and *r*-band light curve have slightly larger uncertainties in the SMP version, causing the main SN light curve to fall below the 5σ threshold at an earlier epoch resulting in fewer individual points visible (Fig. 3.10). Similarly, larger uncertainties for the SMP prevents the detection of a late-time *r*-band signal.

Assuming a sibling exploded during the gap in the observations between 870 and 950 d post peak, SNe Ib and Ic with $E(B - V) \leq 0.3$ mag extinction in the *r*-band can

fit their tail to match the observed detections in the r -band without being excluded by the g -band and i -band non-detections. Therefore, we cannot rule out a sibling as the source of the detected late-time signal.

SN 2020alm

The late-time signal in SN 2020alm is seen in all three bands, beginning at ~ 750 d after the peak and lasting for at least 300 d. There is a gap of 80 d in the observations immediately before the period of activity. The detections slowly rise to a plateau. Our initial analysis only included data for SN 2020alm up to ~ 1000 d after the peak. However, when this object was identified as having late-time detections, the light curve pipeline was rerun and it was found to be still bright at later times, with significant detections in the r - and i -bands, but not above 5σ detections in the g -band. The i -band SMP light curve contained a significant flux offset, as the host was not fully subtracted. We therefore do not further consider this band. The binned SMP r -band light curve fails to reproduce the late-time detections found in the forced photometry light curve. However, the g -band detections are recovered in the SMP. The SN is close to the host nucleus at $0.66''$ (0.85 kpc) offset at the redshift of the SN, but the WISE colours of $W1-W2 = 0.06 \pm 0.04$ and $W2-W3 = 2.42 \pm 0.12$ place it far outside the AGN region.

As SN 2020alm was still active while our analysis was on-going, we obtained two spectra using the Optical System for Imaging and low-Intermediate-Resolution Integrated Spectroscopy (OSIRIS) instrument on the Gran Telescopio CANARIAS (GTC) at Roque de los Muchachos in La Palma on 26 July 2023 using the R1000R grism. As the spectrum is heavily dominated by the host galaxy, we subtracted a rebinned spectrum of the host taken by the Sloan Digital Sky Survey (SDSS, [York et al. 2000](#); [Adelman-McCarthy et al. 2006](#); [Gunn et al. 2006](#); [Smee et al. 2013](#)) in 2003, well before the SN occurred. We confirmed successful host subtraction by checking for residual Na ID and Mg I $\lambda 5175$ absorption lines and found that no residual features were present. A more detailed explanation is given in Appendix [3.8](#).

The resulting spectrum shows an excess that is stronger towards longer wavelengths (Fig. 3.14). This is consistent with the broadband photometry finding an brighter excess in the redder bands, while the g -band remains within the noise after binning the observations. There is some excess in the narrow [N II] $\lambda\lambda 6548, 6583$, $H\alpha$ and [S II] $\lambda\lambda 6716, 6730$ emission lines, but we lack the resolution to check if this is significant. There is no visible additional $H\alpha$ component in the spectrum, which would be indicative of CSM interaction. Integrating the spectrum over the r - and i -band efficiencies gives an $r-i$ colour of 0.6 mag, which is within 3σ of the value found in the latest photometry bin.

Hammerstein et al. (2023) show that TDEs generally have a $g-r$ colour of zero and can have featureless spectra. We approximate a TDE by a flat line in order to estimate the amount of extinction needed to generate a red excess similar to the spectrum. We find that the general shape of the spectrum can be approximated with $0.6 < E(B - V)_{\text{host}} < 1$ mag. This would mean an absolute r -band magnitude of $-18.8 > M_r > -19.8$ mag. Hammerstein et al. (2023) show that both this amount of host extinction and late-time brightness are possible for TDEs. They also show that it is possible for a TDE to rise and fall back down within the 80 d gap in observations, although this is seen in fainter TDEs than corresponding to our estimated absolute magnitude range.

The TDE sample of Hammerstein et al. (2023) did not contain a single object that matches our late-time detections in duration and luminosity in SN 2020alm. However, it is possible to combine parts of different TDEs together to make a TDE that peaked and decayed within the 80 d gap and levelled out by the time it became observable again. Based on this, a TDE is a plausible explanation for the late-time signal detected in this object.

SN 2020pkj

In the case of SN 2020pkj, the first r -band bin with a detection is the end of the normally declining tail, but after the first bin the detections rise slightly in the next

r -band bin (Fig. 3.10). None of the binned photometry for the g - and i -bands give significant detections. Unfortunately, there is a gap in the observations immediately after the r -band detections preventing us from following its evolution closely at these phases. When it became observable again at >200 d, no significant detections were found in any band. The duration of the transient is at least 75 d and could be up to 150 d. In the SMP light curve of this object, a similar rise at the same epochs is recovered, though it is found in the g -band instead of the r -band. This is likely due to the low significance of these detections at just $5.8\text{-}\sigma$ in the r -band in the forced photometry and $5.2\text{-}\sigma$ in the g -band in the SMP, showing that they are just on the detection limit of our binning technique.

With a redshift of $z = 0.02456$, this object is nearby enough for the end of the tail to be visible in the bins at 100 days. This could explain why the first bin is a detection, but the slight increase is still unexpected for a normal SN Ia decline tail. While the second bin is marginally consistent with our tail fit, a slight but steady increase can be seen in the unbinned flux values as well, suggesting that the brightening is real.

Assuming that the detected part of the late-time signal is the brightest part of a sibling transient, the tested transients need significantly more extinction of ~ 3 to 6 mag in the r -band (depending on the comparison transient) than was found for the main SN Ia peak. However, the ~ 80 d gap is long enough for a Type I sibling SN to peak higher during the gap and dim again before observations resumed. The other transient could have just started when it stopped being observable, and declined below the detection limit when the location became observable again. Since there is no constraint on the magnitude, this could work with any amount of extinction. Therefore, we cannot rule out conclusively that the late-time detections are due to another transient.

3.3.2.4 Late-time interaction candidates

Finally, we present the three objects (SN 2018grt, SN 2019ldf, and SN 2020tfc) whose late-time detections could not be explained by any of the explanations discussed above. Their light curves are shown in Fig. 3.11, and the colours of the late-time detections

in Fig. 3.12 and the SMP light curves for SNe 2019ldf and 2020tfc in 3.15. A scene modelling analysis could not be performed for SN 2018grt due to it exploding early in the ZTF survey. The forced photometry pipeline uses images obtained during the ZTF commissioning phase as templates but the SMP does not. We present these three objects as late-time interaction candidates as there are no spectra of these objects at these late times to confirm the presence of features consistent with CSM interaction.

By using the estimated mean absolute r -band magnitude after removing all extinction effects (see Table 3.4) we can estimate the required $H\alpha$ flux assuming that it is the source of all the detected flux in the r -band, and that the emission line has the same width as was used during the simulations. The identified strength of the signal is compared to the $H\alpha$ signal detected in SN 2015cp for each of the events.

SN 2018grt

The late-time signal of SN 2018grt is only detected in the r -band, the g -band stays around zero flux, and there are no i -band observations at these phases. The first detection in the r -band begins at 1350 d post peak with a magnitude of 21.4 ± 0.2 (absolute magnitude of -16.4 mag). It varies little over the ~ 100 d period where it is detected, after which it returns to zero flux within 50 d. The SN is close to the host nucleus with an offset of $0.35''$ (0.32 kpc) but its host colours place it well outside the expected AGN region. Checking the difference images with SNAP shows that the host nucleus and SN location differ by ~ 1 pixel.

The late-time detections are ~ 2.5 mag below the main SN peak. If the late-time signal is due to another SN Ia or a TDE, it would require a significantly higher extinction value than was found for SN 2018grt itself. In addition, this object shows a sudden drop in the r -band, which is not normal behaviour for a TDE. Most of the other transient types cannot reproduce the plateau followed by the sharp decline only detectable in the r -band, apart from a SN IIP, where the plateau of SN 2017gmr has nearly the same time span. However, to fit the observed magnitude with a IIP SN, it would require a host $E(B - V)$ that is three times higher than what was found for SN

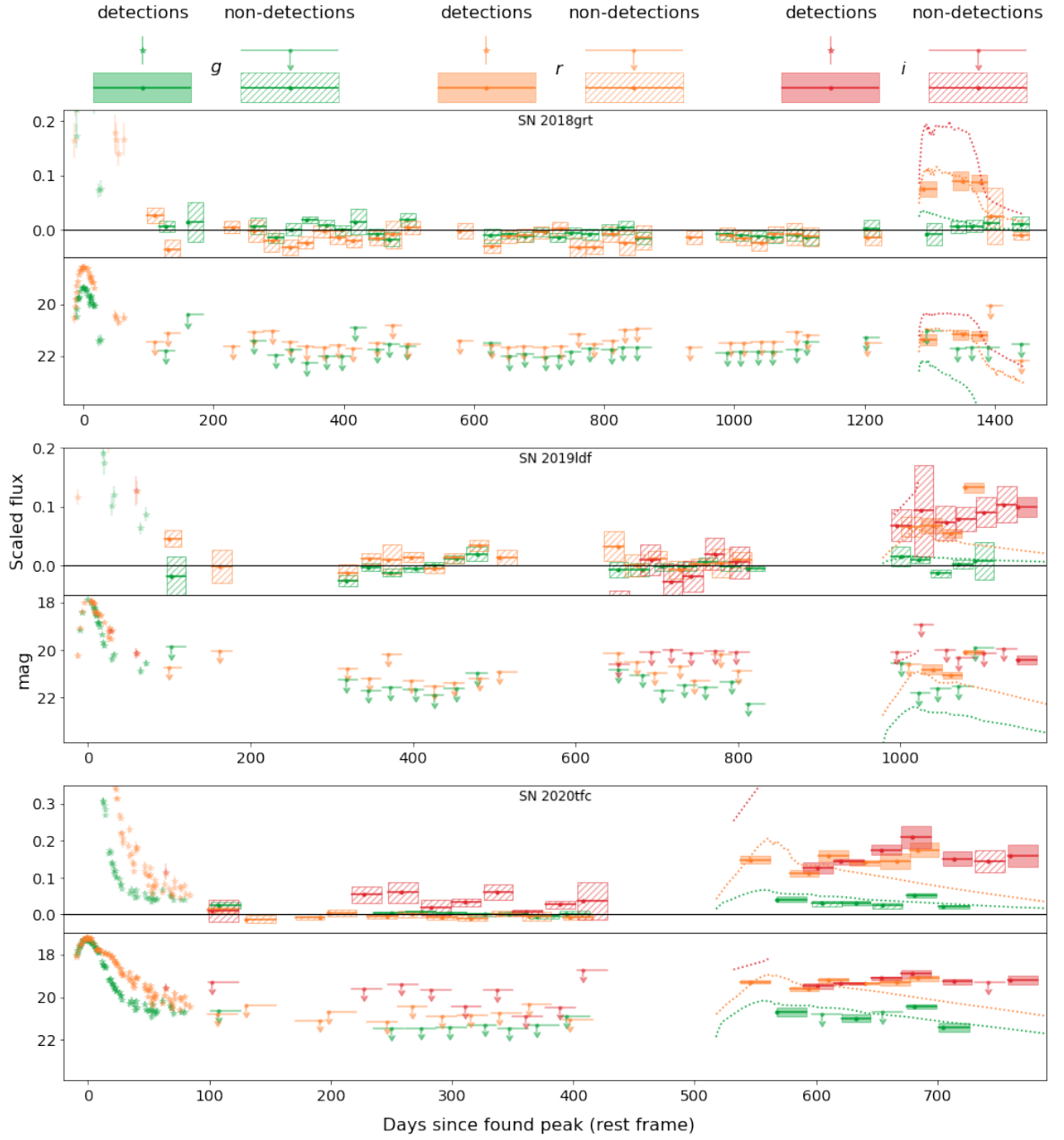


Figure 3.11: Three candidate objects, shown in magnitude and flux space. All three have significant detections ($\geq 5\sigma$) after a period of observations consistent with zero flux. From the alternative explanations the best fitting alternate transients are shown in dotted lines. For SN 2018grt this is the Type IIP SN 2017gmr, for SN 2019ldf and SN 2020tfc this is the TDE AT 2018hco.

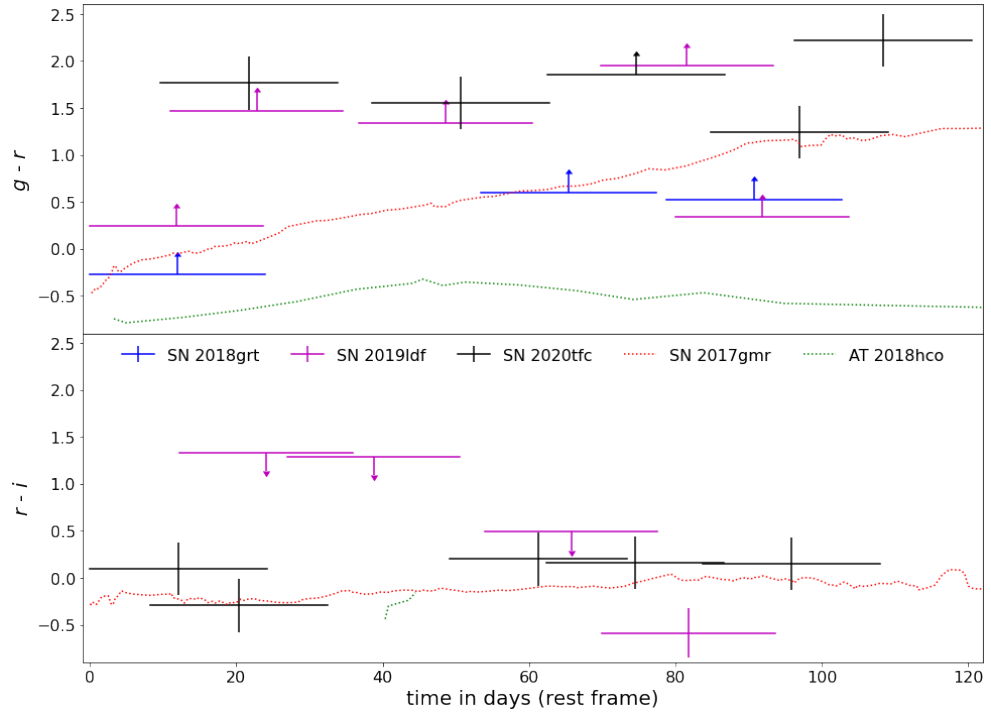


Figure 3.12: Colour curves of the three candidate objects, together with the colours of the best fitting alternate transients. The top and bottom panels show $g-r$ and $r-i$, respectively. The first bin for each object starts at zero days, but the bins can be shifted horizontally in an attempt to better fit the colour curve of the transient compared against (given that this is allowed by the rest of the light curve). Bins whose mean observation dates are closest to each other are used to calculate the colour, provided that these bins overlap in time. If there is a detection in only one band used to calculate the colour while the other is a non-detection, the result is a lower or upper limit.

2018grt, making this scenario less likely to be the case. Therefore, we conclude that late-time CSM interaction is a plausible scenario for the late-time signal in this object.

If we assume $0.21 \leq E(B - V)_{\text{host}} \leq 0.36$ mag and that the r -band signal is produced only by an $H\alpha$ emission line with a similar width to the one used in our simulations in Section 3.2.4, we estimate the strength of the emission to be much stronger than SN 2015cp, at 60 to 100 times its emission strength. However, there are examples of SNe Ia-CSM with interaction strengths this strong, for example, SN 2020eum was within this range (Sharma et al., 2023).

SN 2019ldf

SN 2019ldf has late-time detections in the r -band beginning at 1050 d after the peak and lasting for about 100 d, with an additional increase in brightness towards the end. There is a single 5σ detection in the i -band but there are a number of lower significance detections coeval with the r -band detections. These detections are directly after a long period without observations due to the object being behind the Sun. Nothing is detected in the g -band during the time of the rise in the r -band. The binned SMP light curve recovers these late-time r -band detections, and a single i -band detection, showing that these detections are not specific to the photometry method.

We compared the properties of the late-time detections to those of our comparison transient objects. Even if we assume that a SN exploded during the gap in observations in order to avoid needing a significantly larger $E(B - V)_{\text{host}}$ value, SNe evolve too much over a period of 100 days to explain the detections. In addition, detections would also be expected in the g -band, which have not been found.

A TDE could fit the detections if it was intrinsically bright but heavily extinguished, as this could explain the red colour and absence of signal in the g -band. However, SN 2019ldf is offset from the host nucleus by $0.65''$ (0.78 kpc) and inspection of the difference images using SNAP shows that the late-time signal is more consistent with the SN location than the host nucleus location, disavouring the TDE explanation. Therefore, we conclude that the late-time signal could be due to late-time CSM interaction.

The late-time detections persist until the end of the observation window. To determine if there were still signs of interaction once it was visible again, we obtained g - and r -band photometry with the EFOSC2 imaging spectrograph (Buzzoni et al., 1984) on the ESO New Technology Telescope (NTT) in La Silla, Chile on 2023 May 19 as part of the extended Public ESO Spectroscopic Survey of Transient Objects+ (ePESSTO+; Smartt et al. 2015).

To examine whether the SN is still detected in our images from May 2023, we used image subtraction techniques. Due to the lack of reference images in the g - and r -band filters from EFOSC2, we used images from the DESI Legacy Imaging Surveys Data Release 9 (Dey et al., 2019). After aligning the images, we subtracted them from each other with the High Order Transform of Psf AND Template Subtraction code version 5.11 (HOTPANTS; Becker, 2015). We measured the brightness in the difference images using aperture photometry. The photometry was calibrated against stars from DESI Legacy Imaging Surveys. The EFOSC2 and DESI Legacy Imaging Surveys filters are not identical which might add an unknown systematic to the reported photometry. The 5σ upper limits are $m_g = 24.7$ and $m_r = 24.3$ mag at 1397 days after the peak, with no detection in either band. This means that the signal has disappeared at this time, and thus could have lasted, at most, for about 500 days.

Assuming that the r -band signal is entirely due to the $H\alpha$ emission, we estimate it to be ~ 60 times as strong as the late-time interaction found in SN 2015cp. However, this assumption is very simplistic, as it completely disregards the rise in the i -band and therefore it is only a first order estimate.

SN 2020tfc

This object has late-time gri -band detections, beginning at 550 d after the peak and lasting for at least 250 days. While the r - and i -bands are at more or less the same magnitude, the g -band detections are about 1.3 mag fainter. This immediately poses an issue for any alternate transient considered, as either there is a low amount of extinction and a weak g -band signal, or there is a high amount of extinction and the

intrinsic signal is even brighter in the i -band. This, combined with the fact that the signal lasts for several hundreds of days with little variation, disfavours a SN as an alternate transient explanation. The intrinsic colour also heavily disfavours a TDE as these objects tend to have a similar intrinsic brightness in the g -, r -, and i -bands. In the binned SMP light curve the late-time detections were confirmed in the g -band. The SMP i -band data points have a large scatter, most likely due to uncertain background removal because of a low number of available images for the SMP template. Therefore, we do not consider them further in our analysis. In the r -band SMP light curve, the data points are below our 5σ cut-off for detections, although one is very close to our limit at 4.6σ . However, the g -band detections seen in the forced photometry are confirmed by SMP suggesting a real signal is present at late-times in at least this band, and at lower significance in the r band.

Similar to SN 2020alm, the late-time signal was on-going during our analysis but unfortunately there is no archival host galaxy spectrum available to compare to. As the host dominates the late-time signal (the SN is at a distance of $0.28''$ (0.21 kpc) from the host nucleus) and cannot be removed using difference imaging or SMP as for the photometry, this prevented us from taking a spectrum of the late-time signal. With all alternate explanations ruled out or severely challenged by observations, the late-time CSM interaction remains as a plausible explanation for these late-time detections.

If we assume that the r -band signal is due to $H\alpha$ emission only, the interaction is estimated to be 110 to 150 times as strong as the interaction found in SN 2015cp. This is by far the strongest of the three, but again this simple assumption is unrealistic as it completely ignores the measured g - and i -band signal that suggests a contribution from a continuum or other spectral lines to the late-time signal.

Table 3.6: Parameters used for rate estimation simulations for each object.

Object	Start epoch (d)	Duration (d)	Strength (SN 2015cp)	N_{sample}	late-time CSM fraction	late-time CSM rate ($\text{Gpc}^{-3} \text{ yr}^{-1}$)
SN 2018grt (worst)	1 375*	100	60	748	$0.0084^{+0.0183}_{-0.0041}$	203^{+438}_{-97}
SN 2018grt (best)	1 275*	200	100	988	$0.0015^{+0.0032}_{-0.0007}$	36^{+76}_{-18}
SN 2019ldf (worst)	1 050*	200	60	1 931	$0.0019^{+0.0036}_{-0.0009}$	45^{+87}_{-22}
SN 2019ldf (best)	875*	500	60	2 505	$0.0023^{+0.0038}_{-0.0011}$	54^{+91}_{-26}
SN 2020tfc (worst)	550	250	100	3 439	$0.0004^{+0.0009}_{-0.0002}$	10^{+22}_{-5}
SN 2020tfc (best)	450	500	150	3 493	$0.0003^{+0.0008}_{-0.0002}$	8^{+20}_{-4}

For each of the three SNe we assumed a worst and best case scenario for detecting them in our sample, giving upper and lower limits for a simulated observing campaign. The efficiency curves generated from these simulations were then used to determine the intrinsic fraction of SNe Ia with late-time CSM interaction in an MCMC process, with the assumption that only one object was recovered in a sample size that is the same as the amount of DR2 objects with observations after the start epoch (N_{sample}). The last two columns show the found late-time CSM interaction fraction of the total SN Ia rate and the late-time CSM interaction rate.

*When the start epoch of the late-time excess is >750 d, 750 d is used as the start epoch because of limitations of the available ZTF survey plan. See Section 3.3.3 for more details.

3.3.3 Late-time CSM interaction rates based on our candidate objects

We identified three objects (SNe 2018grt, 2019ldf, and 2020tfc) with potential late-time CSM interaction signatures. For SN 2018grt and SN 2019ldf, these detections were in the r -band (with no i -band data available for SN 2018grt and low significance i -band detections for SN 2019ldf). For SN 2020tfc, late-time detections were found in all three bands (gri). In our initial simulations to determine our recovery efficiency (Section 3.2.4), we made the assumption that any CSM interaction would be dominated by $\text{H}\alpha$ emission that would be present in only the r -band up to $z \sim 0.07$ and in the i -band beyond that. This was based on the dominant interaction signatures seen in SNe Ia-CSM and also the one event with late onset interaction, SN 2015cp (Graham et al., 2019b).

In Graham et al. (2019b), the Ca II NIR triplet emission was also identified in its spectra, along with emission consistent with Mg I $\lambda 5175$. Harris et al. (2018) speculated

that although the Ca II NIR region was very noisy, the Ca II emission may be a similar strength to the $H\alpha$ emission. For SN 2019ldf at a redshift of 0.057, the Ca II NIR triplet, if present, would be partially shifted out of the i -band, which could potentially explain its low-significance i -band detections. SN 2020tfc is at lower redshift (0.031) so the Ca II NIR triplet would fall completely in the i -band and could potentially be the source of the i -band detections. The strength of the potential Mg I $\lambda 5175$ line in SN 2015cp was weak and not well constrained (Graham et al., 2019b) but could potentially result in a weak signature in the g -band. However, without spectral confirmation this is only speculation.

The other difference between our initial simulations for determining recovery efficiency and the observed detections in our three candidate late-time CSM objects is that the late-time CSM interaction signature is much stronger in our observed events. In our three candidates, the late-time signal is between 2 to 3 magnitudes below the SN peak magnitude, while in the simulations with strongest interaction the signal was about 4.4 magnitudes below the peak.

It is clear from our candidate events, that there is significant diversity (detected bands, timescales and strengths) in their potential CSM signatures and without knowledge of their underlying spectra (e.g. emission lines that are present), it is difficult to develop spectral models and run simulations covering this full diversity. Therefore, although very simplistic and ignoring other potential emission lines occurring in the g - and i -bands as were seen in SN 2015cp (Graham et al., 2019b), we focussed on $H\alpha$ emission dominated models and the corresponding r -band detection efficiency to estimate a rate of late-time $H\alpha$ emission dominated CSM interaction based on our three candidate objects. We use the same underlying spectral model (SN 2011fe combined with $H\alpha$ emission) as detailed Section 3.2.4 in further SIMSURVEY simulations but constrain the strength and timescale of the CSM signature based on our three events. In Table 3.6, we show the range of start epoch, duration and strength (dependent on assumed host galaxy extinction) simulated for each event. For each of the three objects, we take the worst case scenario (shortest, weakest, latest start epoch) and the best case

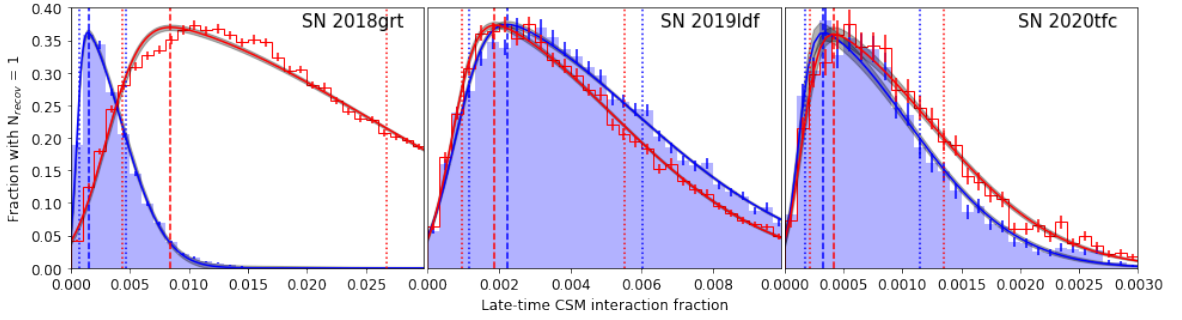


Figure 3.13: Fraction of MCMC realisations per bin that resulted in one object being recovered in a sample with the same size as the effective DR2 sample size as a function of the late-time CSM interaction fraction. The best and worst case scenario for each object is shown in blue and red, respectively. A skewed normal distribution fit with a 1σ uncertainty band is shown for each scenario, and the dashed and dotted lines give maximum and 68 per cent confidence interval of these distributions, respectively. The distributions continue on the right side of each plot.

scenario (longest, strongest, earliest start epoch) allowed by the constraints from the data to estimate a worst and best case scenario recovery efficiency for each object.

Since the available ZTF survey plan for our simulations only spans 1004 d, we cannot set the interaction signal to start at phases after this as the interaction would never be observed. Therefore, we choose to start the interaction in our simulations no more than 750 d after the peak. This is done to ensure there is a decent chance to observe an event until after the interaction has started, while still being able to apply a good baseline correction. As the interaction is by far the dominant source of light at these epochs, changing the start date of the interaction in this way has little effect on the total brightness of the SN. However, it does affect the number of objects observed by allowing more objects to have observations at later times, when the interaction occurs. This is a redshift independent effect, but will impact the resulting recovery fraction function. To account for this, we only consider objects with observations after the start of the interaction, and remove those where the simulation limits prevent any possible late-time detection. While changing the interaction start date has increased the number of objects that satisfy this condition, there are still some objects that do not due to e.g. being in a sparsely observed field.

Not all objects in the DR2 have detections up to the time after the peak where the interaction was detected in the three final candidates. Similar to the simulation, in order to get a proper estimate of the rate we can only consider the objects that could

have been found interacting (N_{sample}), and remove those without observations this late after the peak. This gives us an effective sample size that is smaller than the full DR2, and is listed in Table 3.6.

The expected number of observed objects with late-time interaction in a sample $N_{\text{recov}}(N_{\text{sample}}, \eta(z))$ is a function of the efficiency and the intrinsic rate, which in turn is a fraction of the total SN Ia rate. If we assume the SN Ia rate from Frohmaier et al. (2019) as in our initial simulations and that the fraction of these showing late-time interaction, f , is redshift independent, then the only z dependency is in the efficiency of our pipeline. In a similar approach to Prajs et al. (2017) and Frohmaier et al. (2018), we run a Markov chain Monte Carlo (MCMC) simulation with 10^7 realisations for each scenario to find the fraction of interacting SNe that best explains our findings.

In each realisation of the MCMC, we draw N_{sample} objects, and assign a redshift to each object according to the distribution from Frohmaier et al. (2019). For each object we also draw two random numbers from a flat distribution between zero and one. The first random number is used to decide if the object was interacting, and the second to decide if any interaction would have been recovered. Interaction is true if the random number is below the chosen value for f for that realisation. Recovery is true if the second random number is below $\eta(z)$ at the z of the object (e.g. if the recovery efficiency is 0.7 at the SN redshift, a drawn number below 0.7 will result in a detection if the object was interacting). The number of recovered objects with interaction can be found by counting the objects for which both interaction and recovery is true, while the actual number of interacting objects can be found by counting the objects where interaction is true.

Figure 3.13 shows per bin the fraction of realisations that resulted in one object being recovered as a function of late-time CSM interaction fraction with the best and worst scenario parameters for the three discovered events. We approximate them by fitting a skewed normal distribution and use the fit to estimate the peak of the distribution and the 68 per cent confidence interval on either side. These values are quoted as a fraction of the total SN Ia rate and as the late-time CSM interaction rate in the

last two columns of Table 3.6.

3.4 Discussion

In this section, we first discuss the overall rate of CSM interaction signatures found in our analysis (Section 3.4.1) and some of the properties of the three SNe Ia displaying these unexplained late-time detections (Section 3.4.2).

3.4.1 Late-time interaction is rare in SNe Ia

In our study of the ~ 3500 SNe Ia in the ZTF DR2 with photometry at >100 d, we identified three objects (SN 2018grt, SN 2019ldf, and SN 2020tfc) for which late-time CSM interaction is the best explanation for their detected late-time flux excesses. However, as each of these has significantly different parameters for the interaction, they have to be treated separately when trying to estimate the rate of late-time CSM interaction in SNe Ia (Section 3.3.3). Except for the worst case scenario of SN 2018grt, the identified rate for all cases agree with one another within the uncertainty, with the fraction of SNe Ia showing late-time H α -dominated CSM interaction between $0.03^{+0.08}_{-0.02}$ and $0.23^{+0.38}_{-0.11}$ per cent. This is similar to what was found by Sharma et al. (2023) in their Ia-CSM sample, and agrees with the upper limit set by Graham et al. (2019b) with their discovery of the late-time interaction in SN 2015cp. Some objects were disregarded as we could not definitively determine that they were not due to a sibling transient. Therefore, there could be a handful of additional objects displaying strong late-time H α -dominated CSM interaction that were not included in our rate estimates but this would double the rate at most. Therefore, we estimate that the intrinsic rate of late-time H α -dominated CSM interaction in SNe Ia is < 0.5 per cent.

The identified late-time signals that are consistent with CSM interaction occurred between 1.5 to over 3.5 years after the original SN peaked. If we assume that the SN ejecta have a velocity of the order of 10^4 km s $^{-1}$, the distance at which the CSM shell resides is of the order of 10^{17} cm. As CSM moves slowly, this means it must have been

ejected from the system a long time ago. The further out the shell is from the progenitor system, the more mass is contained in even a thin shell. This is especially true when one considers that in order to get a detectable signal from the interaction, the CSM density cannot be too low. At these distances, light travel time effects also become significant, and a short interaction with a thin shell will be smeared out over a long time. Unfortunately, since we have only partial constraints on the interaction timescales and CSM mass estimation from an interaction signature is far from straightforward, we do not attempt to provide a CSM mass estimate.

An interesting aspect of the late-time detections in our three candidates is their inferred strength. While our model is likely an oversimplification by trying to explain the entire r -band signal using only a narrow $H\alpha$ line, it is clear that the signal is much stronger compared to the one found in SN 2015cp, especially when there are other band(s) at a similar magnitude. Interaction this strong is not unprecedented though, SN 2020aekp for instance, starts to plateau around 50 days after peak at an absolute magnitude $M \sim -18.5$ in all three ZTF bands (Sharma et al., 2023) and holds this plateau for several hundreds of days. Most of the known SNe Ia-CSM presented in Sharma et al. (2023) have detections in multiple bands, and the spectra presented show more than just an $H\alpha$ line coming from the CSM interaction. CSM around a SN Ia also does not have to be spherically symmetric, especially in a scenario where material has been stripped and partially lost from the donor star in the progenitor system. Smith et al. (2015) show for SNe IIn that if the CSM mostly resides in a disk, only the ejecta travelling in the direction of the disk will be slowed down and interact while ejecta at higher inclinations continues to expand normally.

The colour curves for the late-time detections in our three objects (Fig. 3.12), show that $g-r \sim 1.7$ mag for SN 2020tfc, with limits of $g-r > 0.5$ and 1.5 mag for SN 2018grt and SN 19ldf, respectively. For the two objects with i -band observations, $r-i < 0.5$ mag. The SN Ia-CSM sample of Sharma et al. (2023) had late-time (>300 d) $g-r$ colours of $0-0.5$ mag, which are similar to SN 2018grt but bluer than SN 2019ldf and SN 2020tfc. Kool et al. (2023) find $g-r \sim -1$ mag and $r-i \sim 0.5$ mag at late times

for the He-interacting Ia-CSM SN 2020eyj. When taking into account the host galaxy extinction that they identify, it becomes even bluer and is much bluer than our three objects.

3.4.2 Properties of SNe Ia with late-time interaction

The three SNe Ia with late-time flux excesses that cannot be explained by other scenarios have SALT2 light curve fitter x_1 and c values that are generally typical of normal SNe Ia (Rigault et al. in prep.). However, the c value of SN 2018grt of 0.61 ± 0.03 is at the high end and would be excluded from cosmological analyses. We also identified significantly more host extinction for this object than for the other two based on their luminosities at the peak.

All three candidates are found at small projected distances from their host nuclei. While the small sample size might be used to explain part of this observation, the mean projected distance of all objects in the ZTF DR2 is 6.3 kpc (Rigault et al. in prep.). The chance for our three objects to be at most 0.8 kpc from the host is < 1 per cent, suggesting that objects with late-time interaction have a preference for small host separations, the detections are caused by nuclear variability, or they are caused by bad host subtraction. The location of the late-time signal is too close to the host nucleus to distinguish which location the late-time signal is more consistent with by using SNAP. The host galaxy colours are inconsistent with being AGN and the properties of the late-time detections cannot be easily explained by known nuclear transient classes such as TDEs. It is possible that by going to deeper limiting magnitudes with our light curve binning that we have identified previously unstudied nuclear variability but this cannot be confirmed. Imperfect template subtraction can occur to galaxy centres, resulting in a dipole artefact. However, these are easily recognisable with SNAP, and this possibility was ruled out for our three candidates. Therefore, we conclude that that a likely interpretation is that there may be something intrinsic to SNe Ia exploding in these environments that produces late-time CSM interaction but further samples are required to confirm.

The morphologies of the host galaxies of the candidate events are broadly elliptical or spheroidal in nature with no signs of spiral arms. The galaxies have stellar masses of 4×10^9 , 6×10^9 , and $2 \times 10^{10} M_\odot$ for SN 2018grt, SN 2019ldf, and SN 2020tfc, respectively. These host masses are all within the bulk of the masses of the ZTF DR2 SN Ia sample (Rigault et al. in prep.). The hosts of the known H-rich Ia-CSM sample have stellar masses of $\sim 3 \times 10^8$ to $3 \times 10^{10} M_\odot$, consistent with our objects (Sharma et al., 2023). SN 2020eyj, the He-interacting and radio detected SN Ia-CSM (Kool et al., 2023) also had a very small offset from its host of $0.57 \pm 0.02''$ (0.36 ± 0.01 kpc). Its host only has a WISE $W3$ upper limit so it cannot be excluded from having an AGN present. It is a compact star forming galaxy with a mass of $\sim 6 \times 10^7 M_\odot$, which is lower than the typical Ia-CSM range (Sharma et al., 2023).

The hosts of the three candidate events all have WISE $W1 - W2 \approx 0$ mag. SN 2020tfc has $W2 - W3$ of ~ 0.8 mag, while the other two have only limits with $W2 - W3 > 1.2$ mag. Based on Fig. 2 of Irani et al. (2022), this places them in the overlap region between elliptical and spiral host properties from the galaxy sample of Lintott et al. (2011). The vast majority of Ia-CSM sample of Sharma et al. (2023) has $W2 - W3$ colours of > 1 mag, again broadly consistent with our sample. However, the morphologies of our candidate events do not show evidence for spiral arms and their overlap between ellipticals and spirals in the $W2 - W3$ parameter space suggest they may come from different, older stellar populations than the known Ia-CSM events (Kool et al., 2023; Sharma et al., 2023). However, to prove that these are different populations requires a larger sample.

3.4.3 Limitations of the analysis

Since there is no good model of a Type Ia SN interacting with CSM at late times that could be used for our SIMSURVEY simulations, we had to make our own based on several assumptions. Our main assumptions were that the SN Ia looks normal until the moment the interaction starts, and we assumed that this interaction was with hydrogen-rich material showing itself primarily as an $H\alpha$ emission line. This is motivated by the

fact that $H\alpha$ is found in most SNe Ia-CSM and the late-time interaction in SN 2015cp was confirmed through the observation of an $H\alpha$ emission line. However, [Graham et al. \(2019b\)](#) also found other emission lines that are associated with the SN, such as the Ca II triplet near 8500 Å and a tentative detection of Mg I λ 5175, suggesting that our model is too simplistic. Similarly, for SN 2020tfc, we identified late-time detections in the *gri*-bands, which cannot be explained by $H\alpha$ emission alone.

This method of binning the late-time light curves allows to push the detection limit down to a limiting magnitude $m = 21.44$ mag. Since the references used in ZTF have a mean limiting magnitude of $\bar{m}_{\text{lim}} \sim 21.8$ mag, this becomes the leading uncertainty preventing our binning technique to go deeper. We have shown through our simulations that deeper references will allow for the binning technique to go deeper and recover fainter interaction signatures in a larger redshift volume. We have also used SMP to generate light curves that did not rely on forced photometry to test for issues coming from the photometry measurement. In most cases the late-time detections were recovered with both methods, showing their robustness. However, the SMP has been found to have issues with identifying a baseline flux when the number of images used in scene model template creation is small. This highlights the requirement for a long off time to model the underlying galaxy light sufficiently.

The pipeline focusses more on the historical light curve of the SNe than their current state. Since we require two adjacent bins to be detections in order to avoid false positives and the smallest bins we use are 25 d, the interaction needs to be active for over a month before it is picked up. Only after this, can it be followed up with spectroscopy if identified fast enough and the interaction signature is still occurring. Unfortunately, in the cases of our three candidates this could not be done due to a combination of recovering the interaction late, the objects being blocked by the Sun for a section of the year, and not having a suitable reference spectrum of the host galaxy to subtract and isolate the interaction spectrum. Adapting the pipeline to run in real-time would help with shortening the timescale to detection but if the host galaxy contribution is strong, then an archival reference spectrum is required.

3.4.4 By-product pipeline detections

The conservative, catch-all approach outlined in our work poses the challenge of identifying exactly why each object is flagged by the pipeline. Our approach allows for different kinds of objects that become interesting at late times to be caught. We recovered nearly all known Ia-CSM SNe through their non-normal SN Ia tails, as well as a number of known and unknown siblings, along with evidence of a change in the declining tail slope of close-by, normal Type Ia SNe around 200 days after the peak. In our sample, four per cent of the objects needed to be visually inspected, upon which the cause of the (false) positive became clear quickly for most objects. Some of the checks, such as using the WISE colours to identify an AGN host close to the SN location, have been automated, reducing the workload in future attempts to use this method for searching for late-time signals, especially when using large datasets such as the Vera C. Rubin Observatory’s Legacy Survey of Space and Time (LSST; Ivezić et al., 2019).

The pipeline, as presented in this paper, is specifically tailored for finding SNe Ia that deviate from normal behaviour at >100 d after the peak. However, the method of binning late-time observations can be used for any type of transient, but the checks to ensure that the resulting detections are not due to expected behaviour are SN Ia specific. When other types of transients (e.g. SN Ib, Ic, IIP) are used as input, the result will likely vary. For instance, a long lasting plateau in an SN IIP will be unexpected by the pipeline as it does not follow the decline tail of a normal SN Ia. However, modifying the pipeline to work for different kinds of transients mostly requires revision of these checks.

3.5 Conclusions

We have presented a search of the ZTF DR2 SN Ia light curve sample for signatures of late-time CSM interaction. This is the first systematic search for signatures of late-time interaction in SNe Ia in a large optical survey. We made a custom pipeline to calibrate and bin the light curve data at more than 100 d after the peak, using bins

with sizes between 25 and 100 d. Our analysis was based on searching for $H\alpha$ emission (as was seen in SN 2015cp and Ia-CSM) in the r -band at lower redshift and i -band above a redshift of $z = 0.07$. We performed simulations with SIMSURVEY to determine the efficiency of our search, as well as the intrinsic rate of potential $H\alpha$ -dominated CSM interaction in the sample. Our main conclusions are:

1. Our pipeline returned 134 SNe that were potentially interesting based on their late-time light curves. Visual inspection of these objects was performed using our visualisation programme, SNAP, to inspect the difference images, removing 101 objects as false positives.
2. Of the remaining 33 objects, we identified 13 out of the 14 known Ia-CSM objects in the DR2, five siblings close to the position of the original SN Ia, four very nearby events whose late-time light curves were not captured by our simple radioactive tail model and one Iax with a late-time excess in all three bands, consistent with the presence of a bound remnant.
3. Out of our final shortlist of ten candidate events, we identified three SNe Ia (SN 2018grt, SN 2019ldf, and SN 2020tfc) that displayed late-time detections beginning 550 - 1350 d after peak and lasting at least 100 - 250 d, which could not be explained by data issues, AGN activity, or other transient events exploding at a similar location.
4. For SN 2018grt, these late-time detections were only in the r -band (no coeval i -band data was available). For SN 2019ldf, detections were made in the ri -bands and for SN 2020tfc in all three bands suggesting potential contributions with Ca II NIR emission or other Mg I as was identified in SN 2015cp ([Graham et al., 2019b](#)).
5. The r -band magnitudes of the late-time interaction are -16.5 , -16.4 , and -16.8 mag for SN 2018grt, SN 2019ldf, and SN 2020tfc, respectively. At their respective redshifts, this corresponds to $H\alpha$ interaction strengths of 60 – 150 times that of

SN 2015cp (depending on the extinction correction used). The strong nature of this signal could suggest we might only have found the high end of the late-time interaction strength distribution.

6. Using SIMSURVEY simulations of the ZTF survey, we estimated the intrinsic rate of strong $H\alpha$ -dominated late-time (> 100 days after the SN peak) interaction to be occurring in <0.5 per cent of SNe Ia. This translates to absolute rates of 8^{+20}_{-4} to 54^{+91}_{-26} $\text{Gpc}^{-3} \text{ yr}^{-1}$, assuming a constant SN Ia rate of $2.4 \times 10^{-5} \text{ Mpc}^{-3} \text{ yr}^{-1}$ for $z \leq 0.1$.

The rarity of late-time interaction (occurring in <0.5 per cent of SNe Ia) highlights the importance of a large dataset of objects that have been observed for multiple years. The late-time detections occurred at different epochs for each object (from 550 – 1350 d post peak), showing that the phase at which SNe Ia will start to show signs of CSM interaction is highly variable. Therefore, the only viable strategy is to keep observing SNe even after they have faded beyond the detection limit and binning the late-time light curves. The interaction strength that we are sensitive to is heavily dependent on both the science and reference image depth. Future improvements to the analysis would include the use of deeper reference images to detect fainter signatures of late-time interaction, as well as running the pipeline in real time so that additional photometry and spectroscopy can be obtained to further characterise the late-time excesses. The deeper magnitude limits of LSST would be ideal for this study but cannot be immediately performed when the survey starts because of the requirements of deep reference images, as well as the need to wait up to more than three years after the SN Ia peak for the interaction to occur.

3.6 Tables

Table 3.7: Spectra used to make the SN 2011fe model. All spectra were taken from WISeREP (Yaron & Gal-Yam, 2012).

MJD	Phase (d)	Telescope	Instrument	Wavelength coverage (Å)	Reference
55798.0	−16.0	Lijiang-2.4m	YFOSC	3461 – 8956	Zhang et al. (2016)
55798.2	−15.8	Lick-3m	KAST	3416 – 10278	Nugent et al. (2011)
55799.0	−15.0	Lijiang-2.4m	YFOSC	3502 – 8958	Zhang et al. (2016)
55799.3	−14.7	UH88	SNIFS	3296 – 9693	Pereira et al. (2013)
55800.2	−13.8	UH88	SNIFS	3296 – 9693	Pereira et al. (2013)
55801.2	−12.8	UH88	SNIFS	3296 – 9693	Pereira et al. (2013)
55802.3	−11.7	UH88	SNIFS	3296 – 9693	Pereira et al. (2013)
55803.2	−10.8	UH88	SNIFS	3296 – 9693	Pereira et al. (2013)
55804.2	−9.8	UH88	SNIFS	3296 – 9693	Pereira et al. (2013)
55805.2	−8.8	UH88	SNIFS	3296 – 9693	Pereira et al. (2013)
55806.2	−7.8	UH88	SNIFS	3296 – 9693	Pereira et al. (2013)
55807.3	−6.7	UH88	SNIFS	3296 – 9693	Pereira et al. (2013)
55808.2	−5.8	UH88	SNIFS	3296 – 9693	Pereira et al. (2013)
55809.2	−4.8	UH88	SNIFS	3296 – 9693	Pereira et al. (2013)
55811.4	−2.6	HST	STIS	1779 – 24965	Mazzali et al. (2014)
55812.0	−2.0	Gemini-N	GMOS	3497 – 9648	Parrent et al. (2012)
55813.2	−0.8	UH88	SNIFS	3296 – 9693	Pereira et al. (2013)
55814.2	0.2	UH88	SNIFS	3296 – 9693	Pereira et al. (2013)
55815.2	1.2	UH88	SNIFS	3296 – 9693	Pereira et al. (2013)
55816.2	2.2	UH88	SNIFS	3296 – 9693	Pereira et al. (2013)
55817.2	3.2	UH88	SNIFS	3296 – 9693	Pereira et al. (2013)
55817.7	3.7	HST	STIS	1265 – 24965	Mazzali et al. (2014)
55818.2	4.2	UH88	SNIFS	3296 – 9693	Pereira et al. (2013)
55821.2	7.2	UH88	SNIFS	3296 – 9693	Pereira et al. (2013)
55823.2	9.2	UH88	SNIFS	3296 – 9693	Pereira et al. (2013)
55826.2	12.2	UH88	SNIFS	3296 – 9693	Pereira et al. (2013)
55828.2	14.2	UH88	SNIFS	3296 – 9693	Pereira et al. (2013)
55829.0	15.0	Gemini-N	GMOS	3497 – 9643	Parrent et al. (2012)
55830.2	16.2	Keck1	LRIS	3227 – 10242	Stahl et al. (2020)
55831.2	17.2	UH88	SNIFS	3296 – 9693	Pereira et al. (2013)
55832.0	18.0	Lijiang-2.4m	YFOSC	3577 – 8957	Zhang et al. (2016)
55833.2	19.2	UH88	SNIFS	3296 – 9693	Pereira et al. (2013)
55835.3	21.3	HST	STIS	1731 – 10221	Mazzali et al. (2014)
55836.2	22.2	UH88	SNIFS	3296 – 9693	Pereira et al. (2013)
55838.2	24.2	UH88	SNIFS	3296 – 9693	Pereira et al. (2013)
55841.3	27.3	HST	STIS	1738 – 10221	Mazzali et al. (2014)
55855.2	41.2	HST	STIS	1738 – 10216	Mazzali et al. (2014)
55888.6	74.7	UH88	SNIFS	3296 – 9693	Pereira et al. (2013)
55891.7	77.7	UH88	SNIFS	3296 – 9693	Pereira et al. (2013)
55893.6	79.7	UH88	SNIFS	3296 – 9693	Pereira et al. (2013)
55896.6	82.6	UH88	SNIFS	3296 – 9693	Pereira et al. (2013)
55897.7	83.7	Keck1	LRIS	3164 – 10126	Stahl et al. (2020)
55901.6	87.6	UH88	SNIFS	3296 – 9693	Pereira et al. (2013)
55903.6	89.6	UH88	SNIFS	3296 – 9693	Pereira et al. (2013)
55911.0	97.0	XLT	BFOSC	3296 – 9693	Zhang et al. (2016)
55911.6	97.6	UH88	SNIFS	3296 – 9693	Pereira et al. (2013)
55913.5	99.5	Lick-3m	KAST	3427 – 10332	Stahl et al. (2020)
55914.0	100.0	WHT-4.2m	ISIS	3499 – 9491	Friesen et al. (2017)
55916.0	102.0	WHT-4.2m	ISIS	3498 – 9491	Law et al. (2009); Rau et al. (2009)
55917.0	103.0	WHT-4.2m	ISIS	3499 – 9492	Law et al. (2009); Rau et al. (2009)
55926.0	112.0	Lijiang-2.4m	YFOSC	3366 – 9069	Zhang et al. (2016)
55929.5	115.5	Lick-3m	KAST	3426 – 10170	Stahl et al. (2020)
55944.5	130.5	Lick-3m	KAST	3453 – 10088	Stahl et al. (2020)
55959.0	145.0	Lick-3m	KAST	3497 – 10000	Law et al. (2009); Rau et al. (2009)
55980.4	166.4	Lick-3m	KAST	3441 – 10250	Stahl et al. (2020)

MJD	Phase (d)	Telescope	Instrument	Wavelength coverage (Å)	Reference
55988.0	174.0	WHT-4.2m	ISIS	3495 – 9982	Mazzali et al. (2015)
56019.4	205.4	Lick-3m	KAST	3438 – 10324	Mazzali et al. (2015)
56040.4	226.4	Lick-3m	KAST	3437 – 10178	Mazzali et al. (2015)
56047.0	233.0	Lijiang-2.4m	YFOSC	3392 – 9053	Zhang et al. (2016)
56073.0	259.0	WHT-4.2m	ISIS	3495 – 9483	Mazzali et al. (2015)
56103.0	289.0	WHT-4.2m	ISIS	3423 – 10268	Mazzali et al. (2015)
56127.0	313.0	P200	DBSP	3197 – 10991	Law et al. (2009) ; Rau et al. (2009)
56162.2	348.2	Lick-3m	KAST	3487 – 10240	Mazzali et al. (2015)
56194.2	380.2	Keck1	LRIS	3232 – 10268	Stahl et al. (2020)
56277.0	463.0	Lijiang-2.4m	YFOSC	3379 – 9337	Zhang et al. (2016)
56778.5	964.5	Keck1	LRIS	3074 – 10320	Graham et al. (2015)
56831.2	1017.2	LBT	MODS1	3098 – 10487	Taubenberger et al. (2015)

3.7 Inputs to SIMSURVEY simulations

The specific inputs to SIMSURVEY used in Section 3.2.4.2 to determine the detection efficiencies for SN 2015cp-like interaction are listed here.

- Model: SN 2011fe + H α line (Section 3.2.4.1).
- Sky distribution: RA $\in [0^\circ, 360^\circ]$, Dec. $\geq -30^\circ$ (The area covered by ZTF, [Bellm et al. 2019a](#)).
- Volumetric rate: The SN Ia rate is $2.4 \times 10^{-5} \text{ Mpc}^{-3} \text{ yr}^{-1}$ for $z \leq 0.1$ ([Frohmaier et al., 2019](#)). SIMSURVEY uses this to calculate the amount of SNe to generate at a given redshift interval.
- SN peak time distribution: $58\,195 \leq \text{modified Julian date (MJD)} \leq 58\,487$ (between 18 March 2018 and 4 January 2019).
- Galactic extinction: dust maps from [Schlegel et al. \(1998\)](#).
- Host galaxy extinction: [Cardelli et al. \(1989\)](#) extinction law, with $E(B - V)$ drawn from an exponential distribution with exponent $\lambda = 0.11$ ([Stanishev et al., 2018](#)), the same way as host extinction was added in the original SIMSURVEY paper ([Feindt et al., 2019b](#)).
- Telescope specifications: ZTF P48 camera, 4×4 grid of CCDs with four readout channels each, resulting in 64 separate output channels ([Dekany et al., 2020](#)).
- Survey plan: ZTF observation logs between $58\,197 \leq \text{MJD} \leq 59\,211$ (between 20 March 2018 and 28 December 2020), ensuring all simulated SNe are followed for a minimum of about 2 years after the peak.

3.8 Late-time spectrum of SN 2020alm

After confirming the late-time detections in SN 2020alm to still be ongoing, we obtained a spectrum using OSIRIS on the GTC on 26 July 2023, 1277 days after the estimated

Table 3.8: Redshift values where 50 per cent of the simulated SNe were found to have CSM interaction. Strength is the strength of the $H\alpha$ line compared to the strength detected in SN 2015cp. Start shows how many days after the peak the interaction begins, and duration is in days as well. We fitted sigmoid functions to the results of each simulation in order to find the redshift where 50 per cent of the interactions were recovered, assuming the reference images were of the same depth as the ones used in ZTF or 0.5 or 1 mag deeper. These values are shown in $z_{50} \pm \sigma_{z_{50}}$, and χ^2_{red} shows the quality of the fit.

strength	start	duration	ZTF references			0.5 mag deeper			1 mag deeper		
			z_{50}	$\sigma_{z_{50}}$	χ^2_{red}	z_{50}	$\sigma_{z_{50}}$	χ^2_{red}	z_{50}	$\sigma_{z_{50}}$	χ^2_{red}
0.0	–	–	0.0038	0.0009	0.72	0.0042	0.0019	1.83	0.0046	0.0032	3.47
0.1	100	100	0.0041	0.0008	0.83	0.0049	0.0011	1.82	0.0049	0.0033	3.41
0.1	100	300	0.0050	0.0007	0.79	0.0055	0.0014	1.79	0.0059	0.0025	3.42
0.1	100	500	0.0053	0.0006	0.77	0.0062	0.0011	1.76	0.0068	0.0018	3.44
0.1	200	100	0.0045	0.0007	0.78	0.0050	0.0016	1.80	0.0054	0.0028	3.38
0.1	200	300	0.0053	0.0006	0.78	0.0058	0.0014	1.79	0.0063	0.0022	3.44
0.1	200	500	0.0056	0.0006	0.77	0.0066	0.0010	1.79	0.0073	0.0016	3.47
0.1	300	100	0.0050	0.0006	0.80	0.0056	0.0012	1.80	0.0059	0.0023	3.43
0.1	300	300	0.0052	0.0006	0.80	0.0061	0.0044	1.78	0.0067	0.0017	3.46
0.1	300	500	0.0053	0.0005	0.82	0.0060	0.0010	2.03	0.0069	0.0016	3.53
0.1	500	100	0.0045	0.0007	0.82	0.0048	0.0014	2.08	0.0054	0.0021	3.52
0.1	500	300	0.0050	0.0005	0.83	0.0056	0.0010	2.09	0.0062	0.0017	3.53
0.1	500	500	0.0050	0.0005	0.82	0.0057	0.0009	2.09	0.0063	0.0017	3.52
1.0	100	100	0.0041	0.0007	0.86	0.0045	0.0013	2.10	0.0046	0.0027	3.58
1.0	100	300	0.0091	0.0005	0.85	0.0096	0.0012	1.98	0.0108	0.0017	3.40
1.0	100	500	0.0111	0.0004	0.84	0.0129	0.0008	2.08	0.0139	0.0013	3.50
1.0	200	100	0.0067	0.0007	0.80	0.0077	0.0012	2.05	0.0083	0.0021	3.51
1.0	200	300	0.0104	0.0005	0.93	0.0122	0.0008	2.06	0.0130	0.0014	3.31
1.0	200	500	0.0116	0.0004	0.84	0.0129	0.0008	2.11	0.0140	0.0018	3.63
1.0	300	100	0.0086	0.0004	0.78	0.0094	0.0008	1.95	0.0100	0.0013	3.62
1.0	300	300	0.0105	0.0004	0.75	0.0118	0.0007	2.02	0.0128	0.0015	3.61
1.0	300	500	0.0109	0.0004	0.78	0.0125	0.0008	2.11	0.0139	0.0013	3.76
1.0	500	100	0.0081	0.0003	0.83	0.0090	0.0008	1.94	0.0094	0.0016	3.69
1.0	500	300	0.0104	0.0003	0.78	0.0121	0.0007	2.10	0.0133	0.0012	3.79
1.0	500	500	0.0105	0.0003	0.80	0.0122	0.0007	2.11	0.0135	0.0012	3.80
10.0	100	100	0.0091	0.0014	0.93	0.0097	0.0028	2.13	0.0087	0.0058	3.45
10.0	100	300	0.0259	0.0007	1.36	0.0299	0.0009	1.79	0.0328	0.0012	1.83
10.0	100	500	0.0297	0.0005	1.21	0.0347	0.0007	1.83	0.0383	0.0010	1.84
10.0	200	100	0.0204	0.0009	1.69	0.0223	0.0012	2.40	0.0217	0.0019	2.54
10.0	200	300	0.0314	0.0004	1.45	0.0351	0.0007	1.98	0.0377	0.0010	2.40
10.0	200	500	0.0326	0.0005	1.50	0.0374	0.0007	2.05	0.0415	0.0009	1.95
10.0	300	100	0.0221	0.0023	1.21	0.0233	0.0011	2.01	0.0231	0.0019	2.71
10.0	300	300	0.0311	0.0004	1.30	0.0350	0.0007	1.90	0.0375	0.0010	2.27
10.0	300	500	0.0328	0.0004	1.42	0.0381	0.0007	2.22	0.0423	0.0009	2.21
10.0	500	100	0.0199	0.0011	1.80	0.0224	0.0014	2.47	0.0226	0.0019	3.04
10.0	500	300	0.0323	0.0004	1.23	0.0371	0.0007	2.12	0.0406	0.0009	2.19
10.0	500	500	0.0323	0.0004	1.22	0.0373	0.0007	2.12	0.0407	0.0009	2.12

peak date of the SN. As the observed spectrum is heavily dominated by the host galaxy, we subtracted a host galaxy spectrum taken by SDSS in 2003 to remove the host contamination. This was done after re-sampling the host spectrum to have the same wavelength spacing as the new spectrum. This left only the spectrum causing the late-time photometry detections, and is shown in Fig. 3.14. The subtraction was confirmed to be successful by checking that the Mg I $\lambda 5175$ and Na ID absorption lines were reduced to the noise level, as these lines are not expected to be due to the late-time signal but purely from the host galaxy. Some of the host galaxy emission lines were not completely subtracted during this process, most noticeably [N II] $\lambda 6583$ and [S II] $\lambda\lambda 6716, 6730$, but our resolution is inadequate to draw any conclusions from this.

The only explanation for the late-time detections that uses a second transient at the same location is a TDE. Hammerstein et al. (2023) shows that the intrinsic spectrum of a TDE is flat in this wavelength range, with sometimes some narrow emission lines. Therefore, we model a TDE spectrum as a line of constant flux density and add Milky Way extinction (using the SFD89 dust maps in the direction of the object; Schlegel et al., 1998) and variable host extinction in an attempt to obtain the general shape of the observed spectrum. We find that $0.6 \leq E(B - V)_{\text{host}} \leq 1$ mag is adequate to reproduce the general spectral shape and suggests that a TDE with approximately constant colour and moderate host extinction can explain the observed spectral excess for this event.

3.9 Binned SMP light curves of the final candidates

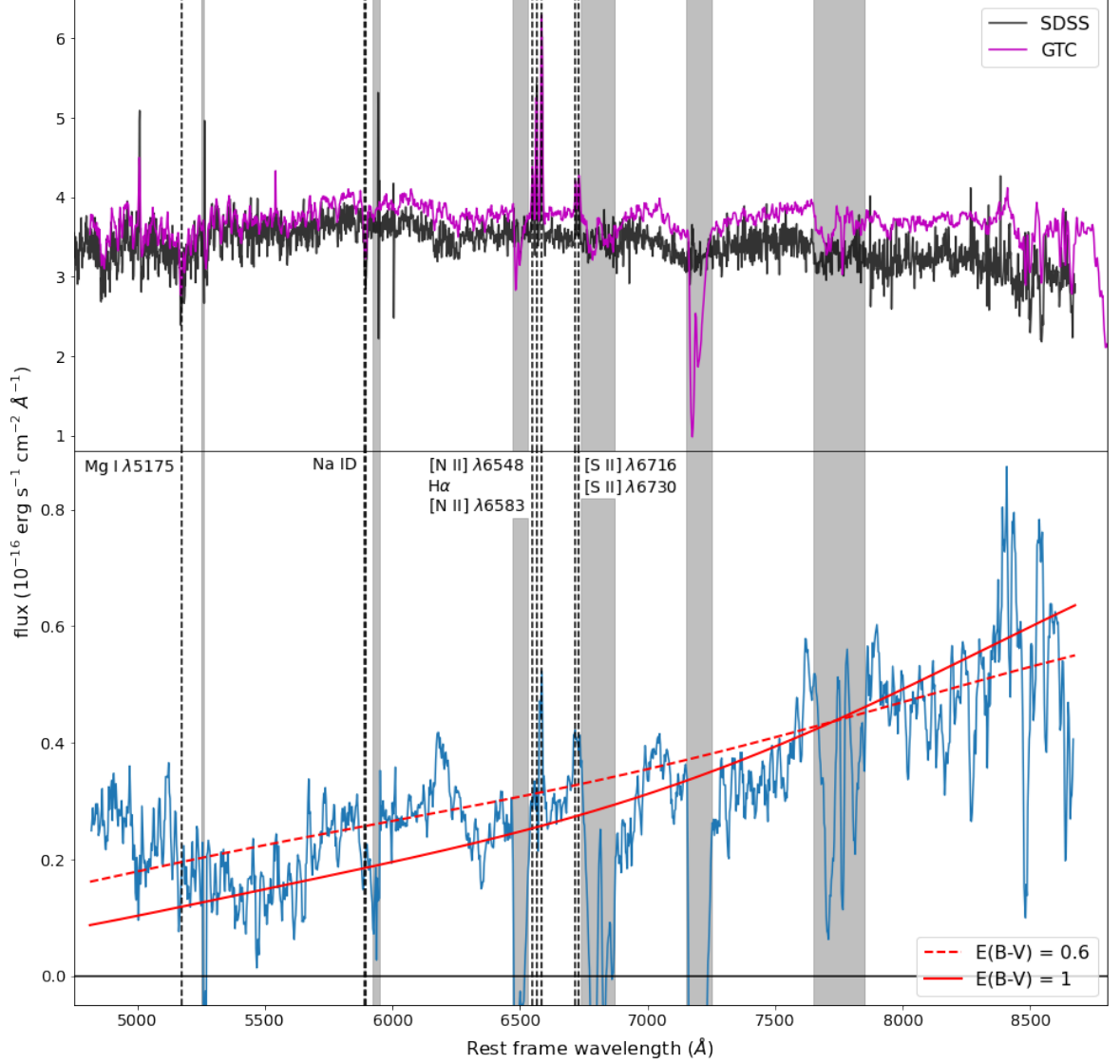


Figure 3.14: Spectrum of the late-time signal in SN 2020alm in its rest frame. The top panel shows the late-time spectrum obtained on 26 July 2023 using OSIRIS on the GTC, and the SDSS spectrum obtained in 2003. The bottom panel shows the late-time excess, obtained by subtracting the SDSS host galaxy spectrum from the observed late-time spectrum. A smoothed spectrum is shown in blue. The smoothing was done using a rolling kernel of size 5 to average over the values. The red lines are a simple TDE model with Milky Way and some amount of host galaxy extinction applied (the amount is shown in the legend), in order to get the approximate shape of the observed spectrum. Narrow emission and absorption lines that were notable in the unsubtracted spectrum are marked with dashed lines. The grey regions are affected by sky lines, and should be ignored. The late-time spectrum of SN 2020alm is available in electronic form at the CDS via anonymous ftp to [cdsarc.u-strasbg.fr](ftp://cdsarc.u-strasbg.fr) (130.79.128.5), via <http://cdsweb.u-strasbg.fr/cgi-bin/qcat?J/A+A/> or upon request to the author.

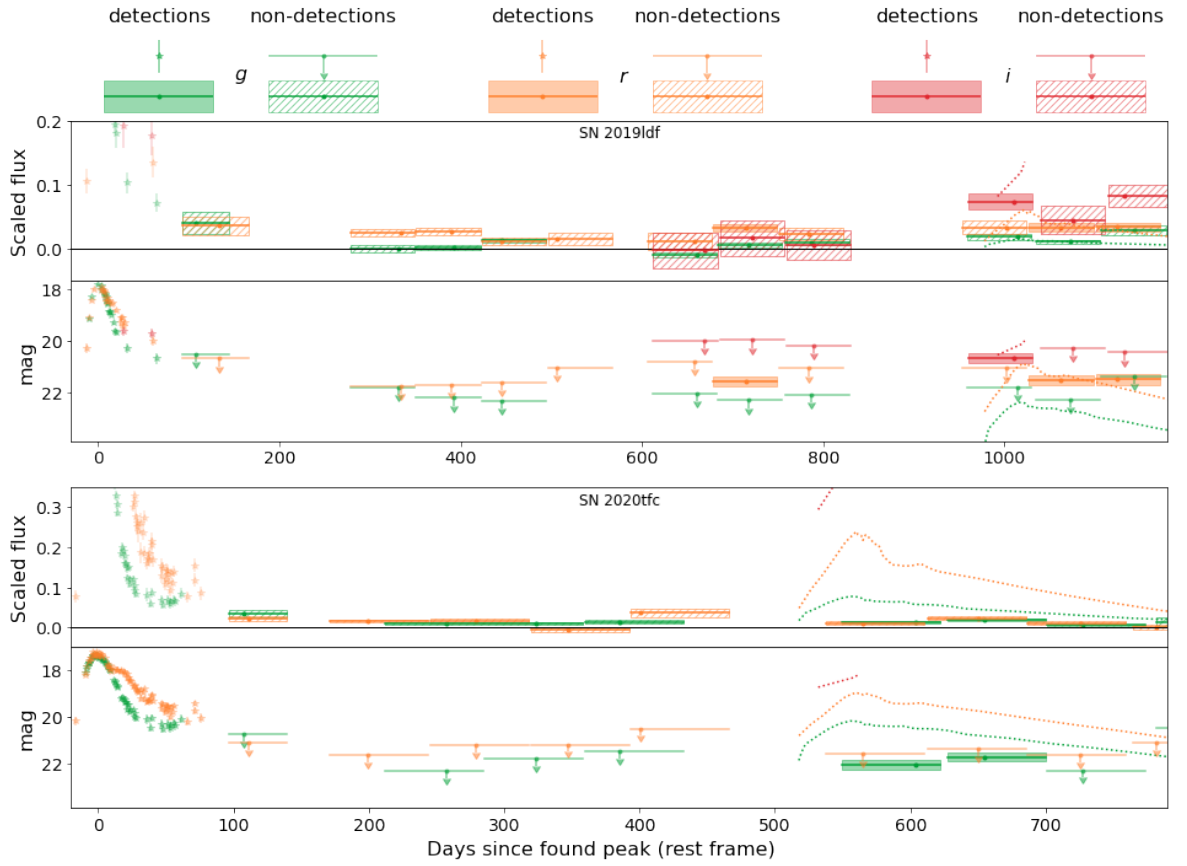


Figure 3.15: Binned SMP light curves of the three candidate objects. As no bins $\geq 5\sigma$ are recovered in SN 2018grt, it is not shown here. Both SN 2019ldf and SN 2020tfc do however still have robust detections in some bands. The best fitting alternate transients, shown in dotted lines, are the same as in Fig. 3.11. The i -band of SN 2020tfc is not shown as the background was not subtracted completely, resulting in a significant flux offset.

References

- Adelman-McCarthy, J. K., Agüeros, M. A., Allam, S. S., et al. 2006, *Astrophysical Journal Supplemental Series*, 162, 38 (Cited on page 51.)
- Ailawadhi, B., Dastidar, R., Misra, K., et al. 2023, *Monthly Notices of the Royal Astronomical Society*, 519, 248 (Cited on page 47.)
- Andrews, J. E., Sand, D. J., Valenti, S., et al. 2019, *Astrophysical Journal*, 885, 43 (Cited on page 47.)
- Barbary, K., Bailey, S., Barentsen, G., et al. 2021, SNCosmo (Cited on page 28.)
- Becker, A. 2015, HOTPANTS: High Order Transform of PSF ANd Template Subtraction, Astrophysics Source Code Library, record ascl:1504.004 (Cited on page 58.)
- Bellm, E. C., Kulkarni, S. R., Barlow, T., et al. 2019a, *Publications of the Astronomical Society of the Pacific*, 131, 068003 (Cited on pages 6 and 74.)
- Bellm, E. C., Kulkarni, S. R., Graham, M. J., et al. 2019b, *Publications of the Astronomical Society of the Pacific*, 131, 018002 (Cited on page 6.)
- Biswas, R., Goobar, A., Dhawan, S., et al. 2022, *Monthly Notices of the Royal Astronomical Society*, 509, 5340 (Cited on page 42.)
- Buzzoni, B., Delabre, B., Dekker, H., et al. 1984, *The Messenger*, 38, 9 (Cited on pages 9 and 58.)
- Camacho-Neves, Y., Jha, S. W., Barna, B., et al. 2023, arXiv e-prints, arXiv:2302.03105 (Cited on page 44.)
- Cardelli, J. A., Clayton, G. C., & Mathis, J. S. 1989, *Astrophysical Journal*, 345, 245 (Cited on pages 29 and 74.)
- Chambers, K. C., Magnier, E. A., Metcalfe, N., et al. 2016, arXiv e-prints, arXiv:1612.05560 (Cited on page 9.)
- Coughlin, M. W., Bloom, J. S., Nir, G., et al. 2023, *Astrophysical Journal Supplemental Series*, 267, 31 (Cited on page 42.)
- Da Costa, G. S. 1992, in *Astronomical Society of the Pacific Conference Series*, Vol. 23, *Astronomical CCD Observing and Reduction Techniques*, ed. S. B. Howell, 90 (Cited on page 14.)
- Dekany, R., Smith, R. M., Riddle, R., et al. 2020, *Publications of the Astronomical Society of the Pacific*, 132, 038001 (Cited on pages 6 and 74.)
- Dey, A., Schlegel, D. J., Lang, D., et al. 2019, *Astronomical Journal*, 157, 168 (Cited on page 58.)
- Dimitriadis, G., Sullivan, M., Kerzendorf, W., et al. 2017, *Monthly Notices of the Royal Astronomical Society*, 468, 3798 (Cited on pages 25, 29, 43 and 44.)
- Duev, D. A., Mahabal, A., Masci, F. J., et al. 2019, *Monthly Notices of the Royal Astronomical Society*, 489, 3582 (Cited on page 42.)
- Dutta, A., Sahu, D. K., Anupama, G. C., et al. 2022, *Astrophysical Journal*, 925, 217 (Cited on pages 37 and 43.)

- Feindt, U., M., R., V., B., & J., N. 2019a, ufeindt/simsurvey: 0.6.0 (Cited on page 28.)
- Feindt, U., Nordin, J., Rigault, M., et al. 2019b, , 2019, 005 (Cited on pages 28, 30 and 74.)
- Filippenko, A. V. 1982, *Publications of the Astronomical Society of the Pacific*, 94, 715 (Cited on page 6.)
- Fremling, C., Miller, A. A., Sharma, Y., et al. 2020, *Astrophysical Journal*, 895, 32 (Cited on page 39.)
- Friesen, B., Baron, E., Parrent, J. T., et al. 2017, *Monthly Notices of the Royal Astronomical Society*, 467, 2392 (Cited on page 72.)
- Frohmaier, C., Sullivan, M., Maguire, K., & Nugent, P. 2018, *Astrophysical Journal*, 858, 50 (Cited on page 63.)
- Frohmaier, C., Sullivan, M., Nugent, P. E., et al. 2019, *Monthly Notices of the Royal Astronomical Society*, 486, 2308 (Cited on pages 63 and 74.)
- Gaia Collaboration, Prusti, T., de Bruijne, J. H. J., et al. 2016, *Astronomy & Astrophysics*, 595, A1 (Cited on page 9.)
- Graham, M. J., Kulkarni, S. R., Bellm, E. C., et al. 2019a, *Publications of the Astronomical Society of the Pacific*, 131, 078001 (Cited on page 6.)
- Graham, M. L., Fremling, C., Perley, D. A., et al. 2022, *Monthly Notices of the Royal Astronomical Society*, 511, 241 (Cited on page 42.)
- Graham, M. L., Harris, C. E., Nugent, P. E., et al. 2019b, *Astrophysical Journal*, 871, 62 (Cited on pages 20, 29, 33, 60, 61, 64, 68 and 70.)
- Graham, M. L., Nugent, P. E., Sullivan, M., et al. 2015, *Monthly Notices of the Royal Astronomical Society*, 454, 1948 (Cited on page 73.)
- Graur, O., Zurek, D., Shara, M. M., et al. 2016, *Astrophysical Journal*, 819, 31 (Cited on page 45.)
- Gunn, J. E., Siegmund, W. A., Mannery, E. J., et al. 2006, *Astronomical Journal*, 131, 2332 (Cited on page 51.)
- Guy, J., Astier, P., Baumont, S., et al. 2007, *Astronomy & Astrophysics*, 466, 11 (Cited on page 28.)
- Hammerstein, E., van Velzen, S., Gezari, S., et al. 2023, *Astrophysical Journal*, 942, 9 (Cited on pages 49, 52 and 76.)
- Harris, C. E., Nugent, P. E., Horesh, A., et al. 2018, *Astrophysical Journal*, 868, 21 (Cited on page 60.)
- Hill, J. M., Green, R. F., & Slagle, J. H. 2006, in Society of Photo-Optical Instrumentation Engineers (SPIE) Conference Series, Vol. 6267, Society of Photo-Optical Instrumentation Engineers (SPIE) Conference Series, ed. L. M. Stepp, 62670Y (Cited on page 29.)
- Holtzman, J. A., Marriner, J., Kessler, R., et al. 2008, *Astronomical Journal*, 136, 2306 (Cited on page 21.)
- Hviding, R. E., Hainline, K. N., Rieke, M., et al. 2022, *Astronomical Journal*, 163, 224 (Cited on pages 45 and 47.)
- Irani, I., Prentice, S. J., Schulze, S., et al. 2022, *Astrophysical Journal*, 927, 10 (Cited on page 67.)

- Ivezić, Ž., Kahn, S. M., Tyson, J. A., et al. 2019, *Astrophysical Journal*, 873, 111 (Cited on page 69.)
- Jayasinghe, T., Stanek, K. Z., Kochanek, C. S., et al. 2019, *Monthly Notices of the Royal Astronomical Society*, 485, 961 (Cited on page 9.)
- Jordan, George C., I., Perets, H. B., Fisher, R. T., & van Rossum, D. R. 2012, *Astrophysical Journal Letters*, 761, L23 (Cited on page 43.)
- Kasliwal, M. M., Cannella, C., Bagdasaryan, A., et al. 2019, *Publications of the Astronomical Society of the Pacific*, 131, 038003 (Cited on page 42.)
- Kawabata, M., Kawabata, K. S., Maeda, K., et al. 2018, *Publications of the Astronomical Society of Japan*, 70, 111 (Cited on page 44.)
- Kilpatrick, C. D., Drout, M. R., Auchettl, K., et al. 2021, *Monthly Notices of the Royal Astronomical Society*, 504, 2073 (Cited on page 47.)
- Kool, E. C., Johansson, J., Sollerman, J., et al. 2023, *Nature*, 617, 477 (Cited on pages 39, 65 and 67.)
- Kromer, M., Fink, M., Stanishev, V., et al. 2013, *Monthly Notices of the Royal Astronomical Society*, 429, 2287 (Cited on page 44.)
- Kulkarni, S. R. 2013, *The Astronomer’s Telegram*, 4807, 1 (Cited on page 9.)
- Law, N. M., Kulkarni, S. R., Dekany, R. G., et al. 2009, *Publications of the Astronomical Society of the Pacific*, 121, 1395 (Cited on pages 9, 28, 72 and 73.)
- Lintott, C., Schawinski, K., Bamford, S., et al. 2011, *Monthly Notices of the Royal Astronomical Society*, 410, 166 (Cited on page 67.)
- Masci, F. J., Laher, R. R., Rusholme, B., et al. 2019, *Publications of the Astronomical Society of the Pacific*, 131, 018003 (Cited on page 6.)
- Mazzali, P. A., Sullivan, M., Filippenko, A. V., et al. 2015, *Monthly Notices of the Royal Astronomical Society*, 450, 2631 (Cited on page 73.)
- Mazzali, P. A., Sullivan, M., Hachinger, S., et al. 2014, *Monthly Notices of the Royal Astronomical Society*, 439, 1959 (Cited on pages x, 31, 47 and 72.)
- McCully, C., Crawford, S., Kovacs, G., et al. 2018, *astropy/astroscrappy: v1.0.5 Zenodo Release* (Cited on page 13.)
- McCully, C., Jha, S. W., Scalzo, R. A., et al. 2022, *Astrophysical Journal*, 925, 138 (Cited on page 44.)
- Miller, A. A., Yao, Y., Bulla, M., et al. 2020, *Astrophysical Journal*, 902, 47 (Cited on page 22.)
- Nugent, P. E., Sullivan, M., Cenko, S. B., et al. 2011, *Nature*, 480, 344 (Cited on page 72.)
- Parrent, J. T., Howell, D. A., Friesen, B., et al. 2012, *Astrophysical Journal Letters*, 752, L26 (Cited on page 72.)
- Patat, F. 2005, *Monthly Notices of the Royal Astronomical Society*, 357, 1161 (Cited on page 45.)
- Patat, F., Cordiner, M. A., Cox, N. L. J., et al. 2013, *Astronomy & Astrophysics*, 549, A62 (Cited on page 29.)
- Pereira, R., Thomas, R. C., Aldering, G., et al. 2013, *Astronomy & Astrophysics*, 554, A27 (Cited on page 72.)

- Perley, D. A., Fremling, C., Sollerman, J., et al. 2020, *Astrophysical Journal*, 904, 35 (Cited on page 39.)
- Planck Collaboration, Aghanim, N., Akrami, Y., et al. 2020, *Astronomy & Astrophysics*, 641, A6 (Cited on page 1.)
- Prajs, S., Sullivan, M., Smith, M., et al. 2017, *Monthly Notices of the Royal Astronomical Society*, 464, 3568 (Cited on page 63.)
- Rau, A., Kulkarni, S. R., Law, N. M., et al. 2009, *Publications of the Astronomical Society of the Pacific*, 121, 1334 (Cited on pages 9, 28, 72 and 73.)
- Ravi, A. P., Rho, J., Park, S., et al. 2023, *Astrophysical Journal*, 950, 14 (Cited on page 47.)
- Reusch, S. 2020, ztffps (Cited on page 21.)
- Rigault, M. 2018, ztfquery, a python tool to access ZTF data (Cited on page 27.)
- Schlegel, D. J., Finkbeiner, D. P., & Davis, M. 1998, *Astrophysical Journal*, 500, 525 (Cited on pages 74 and 76.)
- Shappee, B. J., Prieto, J. L., Grupe, D., et al. 2014, *Astrophysical Journal*, 788, 48 (Cited on page 9.)
- Shappee, B. J. & Stanek, K. Z. 2011, *Astrophysical Journal*, 733, 124 (Cited on page 28.)
- Shappee, B. J., Stanek, K. Z., Kochanek, C. S., & Garnavich, P. M. 2017, *The Astrophysical Journal*, 841, 48 (Cited on page 29.)
- Sharma, Y., Sollerman, J., Fremling, C., et al. 2023, *Astrophysical Journal*, 948, 52 (Cited on pages 39, 57, 64, 65 and 67.)
- Smartt, S. J., Valenti, S., Fraser, M., et al. 2015, *Astronomy & Astrophysics*, 579, A40 (Cited on pages 9 and 58.)
- Smee, S. A., Gunn, J. E., Uomoto, A., et al. 2013, *Astronomical Journal*, 146, 32 (Cited on page 51.)
- Smith, N., Mauerhan, J. C., Cenko, S. B., et al. 2015, *Monthly Notices of the Royal Astronomical Society*, 449, 1876 (Cited on page 65.)
- Stahl, B. E., Zheng, W., de Jaeger, T., et al. 2020, *Monthly Notices of the Royal Astronomical Society*, 492, 4325 (Cited on pages 72 and 73.)
- Stanishev, V., Goobar, A., Amanullah, R., et al. 2018, *Astronomy & Astrophysics*, 615, A45 (Cited on page 74.)
- Strotjohann, N. L., Ofek, E. O., Gal-Yam, A., et al. 2021, *Astrophysical Journal*, 907, 99 (Cited on pages 24 and 35.)
- Taubenberger, S., Elias-Rosa, N., Kerzendorf, W. E., et al. 2015, *Monthly Notices of the Royal Astronomical Society*, 448, L48 (Cited on page 73.)
- Terwel, J. H., Maguire, K., Dimitriadis, G., et al. 2024, arXiv e-prints, arXiv:2402.16962 (Cited on page 20.)
- Tonry, J. L., Denneau, L., Heinze, A. N., et al. 2018, *Publications of the Astronomical Society of the Pacific*, 130, 064505 (Cited on page 9.)
- van der Walt, S. J., Crellin-Quick, A., & Bloom, J. S. 2019, *Journal of Open Source Software*, 4 (Cited on page 42.)

- van Dokkum, P. G. 2001, *Publications of the Astronomical Society of the Pacific*, 113, 1420 (Cited on page 13.)
- van Velzen, S., Gezari, S., Hammerstein, E., et al. 2021, *Astrophysical Journal*, 908, 4 (Cited on page 47.)
- Wright, E. L., Eisenhardt, P. R. M., Mainzer, A. K., et al. 2010, *Astronomical Journal*, 140, 1868 (Cited on pages 10 and 47.)
- Yao, Y., Miller, A. A., Kulkarni, S. R., et al. 2019, *Astrophysical Journal*, 886, 152 (Cited on page 22.)
- Yaron, O. & Gal-Yam, A. 2012, *Publications of the Astronomical Society of the Pacific*, 124, 668 (Cited on pages xiii, 28 and 72.)
- York, D. G., Adelman, J., Anderson, John E., J., et al. 2000, *Astronomical Journal*, 120, 1579 (Cited on page 51.)
- Zackay, B., Ofek, E. O., & Gal-Yam, A. 2016, *Astrophysical Journal*, 830, 27 (Cited on page 21.)
- Zhang, K., Wang, X., Zhang, J., et al. 2016, *Astrophysical Journal*, 820, 67 (Cited on pages xi, 43, 44, 72 and 73.)